FUNDAMENTALS OF UNDERVOLTAGE BREAKDOWN THROUGH THE TOWNSEND MECHANISM

James E. Cooley

A DISSERTATION
PRESENTED TO THE FACULTY
OF PRINCETON UNIVERSITY
IN CANDIDACY FOR THE DEGREE
OF DOCTOR OF PHILOSOPHY

RECOMMENDED FOR ACCEPTANCE
BY THE DEPARTMENT OF
MECHANICAL AND AEROSPACE ENGINEERING
Advisor: Professor Edgar Y. Choueiri

September, 2008

Fundamentals of Undervoltage Breakdown Through the Townsend Mechanism

Prepared by:

James E. Cooley

Approved by:

Professor Edgar Y. Choueiri
Dissertation Advisor

Professor Robert G. Jahn
Dissertation Reader

Dr. Samuel A. Cohen
Dissertation Reader

Abstract

The conditions under which an externally supplied pulse of electrons will induce breakdown in an undervoltaged, low-gain, DC discharge gap are experimentally and theoretically explored. The phenomenon is relevant to fundamental understanding of breakdown physics, to switching applications such as triggered spark gaps and discharge initiation in pulsed-plasma thrusters, and to gas-avalanche particle counters.

A dimensionless theoretical description of the phenomenon is formulated and solved numerically. It is found that a significant fraction of the charge on the plates must be injected for breakdown to be achieved at low avalanche-ionization gain, when an electron undergoes fewer than approximately 10 ionizing collisions during one gap transit. It is also found that fewer injected electrons are required as the gain due to electron-impact ionization (α process) is increased, or as the sensitivity of the α process to electric field is enhanced by decreasing the reduced electric field (electric field divided by pressure, E/p).

A predicted insensitivity to ion mobility implies that breakdown is determined during the first electron avalanche when space charge distortion is greatest. A dimensionless, theoretical study of the development of this avalanche reveals a critical value of the reduced electric field to be the value at the Paschen curve minimum divided by 1.6. Below this value, the net result of the electric field distortion is to increase ionization for subsequent avalanches, making undervoltage breakdown possible. Above this value, ionization for subsequent avalanches will be suppressed and undervoltage breakdown is not possible.

Using an experimental apparatus in which ultraviolet laser pulses are directed onto a photo-emissive cathode of a parallel-plate discharge gap, it is found that undervoltage breakdown can occur through a Townsend-like mechanism through the buildup of successively larger avalanche generations. The minimum number of injected electrons required to achieve breakdown is measured in argon at pd values of 3-10 Torr-m. The required electron pulse magnitude was found to scale inversely with pressure and voltage in this parameter range. When higher-power infrared laser pulses were used to heat the cathode

surface, a faster, streamer-like breakdown mechanism was occasionally observed.

As an example application, an investigation into the requirements for initiating discharges in Gas-fed Pulsed Plasma Thrusters (GFPPTs) is conducted. Theoretical investigations based on order-of-magnitude characterizations of previous GFPPT designs reveal that high-conductivity arc discharges are required for critically-damped matching of circuit components, and that relatively fast streamer breakdown is preferable to minimize delay between triggering and current sheet formation. The faster breakdown mechanism observed in the experiments demonstrates that such a discharge process can occur. However, in the parameter space occupied by most thrusters, achieving the phenomenon by way of a space charge distortion caused purely by an electron pulse should not be possible. Either a transient change in the distribution of gas density, through ablation or desorption, or a thruster design that occupies a different parameter space, such as one that uses higher mass bits, higher voltages, or smaller electrode spacing, is required for undervoltage breakdown to occur.

Acknowledgments

My time at Princeton amounts to the most educationally productive period of my life, and I will be forever indebted to all the people who made it so.

First, to Edgar Choueiri, my advisor. Thank you for giving me the freedom to make this project my own, for helping me sharpen my technical communication skills, for showing me how to see the forest of real physical insight for the trees of scientific results, and for your insistence that to do anything less would be a waste of everyone's time. For the rest of my career, I will judge myself by the incredibly high standards you set for yourself and your students. On a personal level, thank you for showing compassion and understanding when I needed for family matters to become a priority. I will always be grateful.

I would like to thank Bob Sorenson, our technician. Without Bob, nothing would have been built, and no code would have been written. Again and again, you demonstrated the importance of care, precision, and getting something right the first time. With the exception of your insufferable puns, I greatly miss our daily conversations.

To the students who were already there when I arrived: Andrea, Kamesh, Jack, Lenny, Slava, and Kurt, thank you for helping me navigate through all the obstacles I would find in my way. From classes, to generals, to last-minute, late-night, paper rewriting sessions, I couldn't have gotten through it without your guidance. Thank you also for your friendship and for making the lab into a fun, vibrant community. I will always remember our many trips to George's, our volleyball and poker games, our road trips, and our historic European tour.

To Luke and Peter, who arrived after I got there, thanks for bringing new life and new perspectives to the lab. Thanks especially to Luke for a certain early-morning bike ride across campus. To Peter, your advice on numerical methods was the difference between having working code and having generated numerical results with Microsoft Paint. To the even newer students, Ashley and Danny, thanks for reminding me about the importance of enthusiasm for new research.

I would like to thank all of the teachers I've had over the years, but especially Bob Jahn

and Sam Cohen. To Bob, for coming to all those lab meetings and for asking questions and giving suggestions that were always insightful. To Sam, for simultaneously teaching me the techniques of, and enthusiasm for, experimental plasma physics. To both of you for showing me the importance of pursuing research for which you truly have passion.

Finally, I would like to thank Becca, my wife. I could not have done this without your patience and support. Compromise in relationships is not uncommon, but you have an extraordinary knack for embracing it. What I love about you is not so much that you agreed to move to (horrors!) New Jersey, but that you found a way to love it there.

This research has been supported by the Program in Plasma Science and Technology at the Princeton Plasma Physics Laboratory and by a DRDF grant from NASA-JPL. This dissertation carries the designation 3187T in the records of the Department of Mechanical and Aerospace Engineering.

Nomenclature

A	Empirical coefficient for determining α
$A(x,t)$	Heating function
A	Richardson coefficient
a	Coaxial transmission line inner conductor outer diameter
α	Townsend ionization coefficient
B	Empirical coefficient for determining α
b	Coaxial transmission line outer conductor inner diameter
β	Decay rate constant
C	α fit coefficient
C	PPT circuit capacitance
D	α fit coefficient
D	Diffusion coefficient
d	Gap width
$\Delta\bar{t}$	Numerical time step (dimensionless)
$\Delta\bar{x}$	Grid spacing (dimensionless)
δ	Skin depth
E	Electric field
E_0	Applied or initial electric field
E_r	Electric field at spherical avalanche front
e	Electron charge
e	Base of the natural logarithm
ϵ_0	Permittivity of free space
ε_i	Ionization potential
η_{thrust}	Thrust efficiency
$F(t)$	Absorbed laser irradiance
$\Gamma_{e,+}$	Electron, ion flux
Γ_{pulse}	Injected electron flux
γ	Secondary emission coefficient
h	Planck's constant
I_{peak}	Peak laser intensity
J	Current
J_{CL}	Child-Langmuir current
J_{crit}	Space-charge limited current
j_0	Background current
j_e	Electron current
$\dot{j}_{\mathrm{max}}$	Maximum current rise rate

K	Thermal conductivity
k	Reaction coefficient
k_i	Calibration fit constant
κ	Thermal diffusivity
L_0	Initial circuit inductance
Λ	Length scale for diffusive loss
λ	Ionization mean-free-path
μ	Breakdown parameter
μ_0	Initial value of breakdown parameter
μ_0	Permeability of free space
$\mu_{e,+}$	Electron, ion mobility
N_{e0}	Areal density of injected electrons
$\bar{N}^*_{e0}$	Critical dimensionless injected areal electron density
n	Neutral gas volumetric density
n	Number of pulses in a bin
$n_{e,+}$	Volumetric electron, ion density
ν	Courant number
ν	Sigmoid fit parameter
ν	Optical frequency
ν_m	Momentum-transfer collision frequency
p	Breakdown probability
p	pressure
$\bar{p}^*$	Critical dimensionless pressure
ϕ	Work function
ϕ	Electrostatic potential
q	Variable employed in theoretical analysis
q'	Normalization reference variable
$\bar{q}$	Normalized variable
Q	Total charge released during a laser pulse
Q	Capacitor charge
R	Plasma resistance
R	Desorption rate
r_D	Radius of spherical avalanche front
σ	Binomial error
σ	Gas amplification factor
σ_1	Gas amplification factor after first avalanche
τ	Injected electron temporal pulsewidth
T	Temperature
$T_{+,e}$	Ion, electron transit time in absence of distortion
t	Time
τ	Loss mechanism lifetime

V	Voltage
V_B	Breakdown voltage
v_d	Drift velocity
X	Dimensionless temporal pulsewidth
x	Position coordinate
x	Sigmoid fit data
$x_{1/2}$	Sigmoid fit parameter
ξ	Avalanche time parameter
y	Sigmoid fit data
y_0	Sigmoid fit parameter
$y_{\max}$	Sigmoid fit parameter
Z_0	Characteristic impedance of a transmission line

Contents

Chapter 1

Introduction

1.1 Undervoltage Breakdown

When the voltage across two electrodes that span a gas-filled gap is raised above a certain threshold potential, the neutral gas transitions to conductive plasma in a process known as *breakdown*. The threshold potential, known as the *breakdown voltage* or *sparking potential*, is determined by electrode geometry and material, gas composition, and gas pressure. A discharge gap held below this potential is said to be at an *undervoltage*, and will not break down under most circumstances.

It is possible, however, to induce breakdown in an undervoltaged gap by introducing a burst of electrons (see Figure 1.1). These electrons will undergo ionizing collisions with the neutral gas molecules, temporarily alter the distribution of space charge in the gap — and in turn, alter the electric field profile — and cause runaway ionization. The voltage required to sustain a gas discharge is always lower than the voltage required to form it, so a stable conducting state can be reached at a moderate undervoltage after a single burst of electrons.

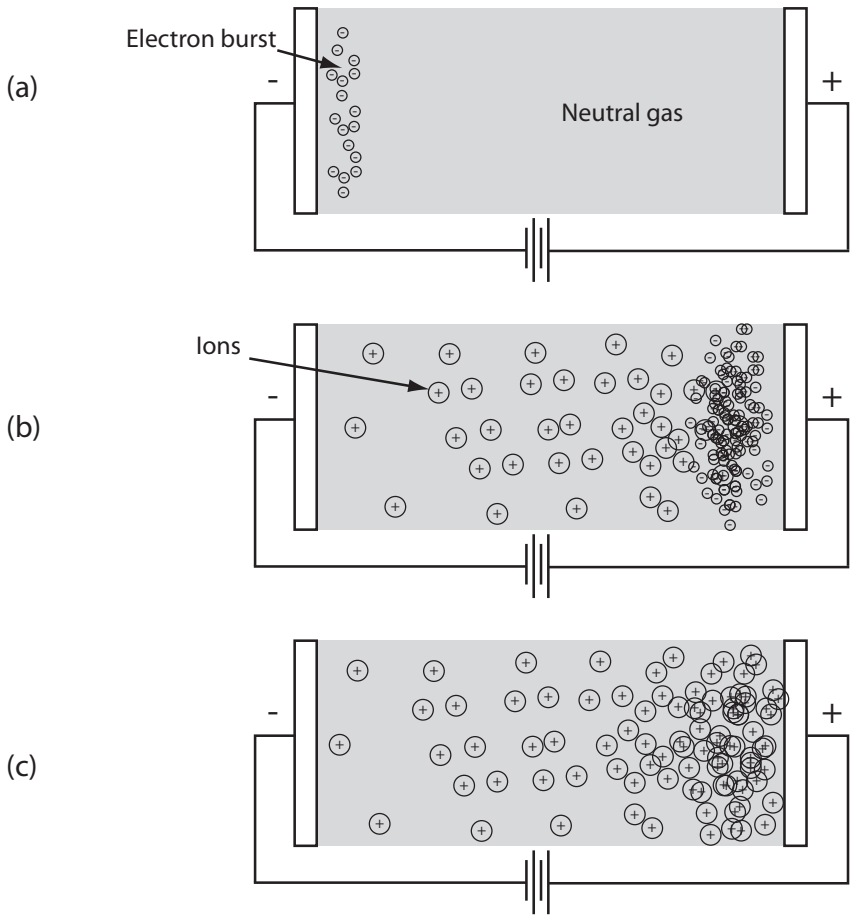

Figure 1.1: Undervoltage breakdown. (a) A burst of electrons is introduced at the cathode of an undervoltaged discharge gap. (b) The burst drifts toward the anode, ionizing neutral molecules, creating ions and more electrons. (c) The relatively immobile ions are left behind when the electrons are absorbed in the anode, enhancing the electric field and increasing further ionization.

This process is called *undervoltage breakdown*, and is the subject of this work.

In practice, the electron burst can be supplied in a number of ways: through ultraviolet flashes on a photoemissive surface [1–4], a source of α-particles [5, 6], or high-voltage pulses on needles, sparkplugs, or other electrodes [7–9]. Achieving breakdown at an undervoltage is an attractive technique for a number of applications because it is a particularly controllable, reliable, and repeatable method of triggering a gas discharge. As a result, numerous investigations [1–3, 10] have explored the phenomenon in order to understand basic processes in breakdown physics.

In addition, undervoltage breakdown is employed in a wide variety of devices ranging from gas avalanche particle detectors [11], to high-current switching applications such as discharge initiation in pulsed plasma thrusters [12], triggered spark gaps [13],and pseudospark switches [14].

The phenomenon was first observed experimentally by Kluckow [1] as reported in [15]. Work was carried out by others [2, 3], most extensively Sato and Sakamoto who investigated the phenomenon in air, theoretically and experimentally, over a range of pressures. Fonte [6] modeled breakdown of parallel-plate avalanche chambers and showed that the breakdown threshold — the minimum criteria under which breakdown will occur in those devices — corresponds to the conditions necessary for streamer formation predicted in [15]. This result is consistent with experimental measurements of breakdown threshold in parallel-plate avalanche chambers for a variety of conditions [11].

1.2 Motivation for This Thesis

Undervoltage breakdown has been experimentally achieved numerous times and theoretical models of significant sophistication have been produced that agree well with the experimental data. In general, though, the goals of each investigation have been to understand some phenomenon that is specific to that application — preventing breakdown in gas avalanche particle detectors, for example, or developing a robust, high-current gas switch.

A more fundamental approach, reaching conclusions about undervoltage breakdown that are universally applicable, has never been undertaken.

In particular, one issue that has received little attention in the literature is the question of threshold criteria: how many electrons are required to induce breakdown for a given set of undervoltage conditions? This question is of particular interest because it represents a design criterion for any device seeking to employ undervoltage breakdown. Furthermore, we will see that investigation of threshold criteria, and more generally, the conditions under which undervoltage breakdown might or might not occur, can lead to fundamental insight into how the phenomenon works.

That being said, it is not our goal to isolate our investigation in a vacuum of generality. We will seek to apply the universal understanding gleaned from our fundamental investigations to gain insight into a real-world problem: discharge initiation in gas-fed pulsed plasma thrusters (GFPPTs). GFPPTs are electric propulsion devices that offer several performance advantages over other thruster systems [16,17], but are hindered by the lack of a robust technique for plasma current sheet formation. Because the thrusters require precise discharge timing and control, such a technique is likely to rely on some form of undervoltage breakdown as a fundamental mechanism, and understanding the phenomenon is the first step toward improving them.

To that end, the research we present here was carried out to answer the following questions:

- How do we explain the phenomenon of undervoltage breakdown through electron pulse injection, specifically focusing on how that phenomenon behaves at low ionization gain (fewer than about 10 ionizing collisions during an electron transit)?
- Under what conditions can undervoltage breakdown occur?
- For a given set of favorable undervoltage conditions, how large a pulse of electrons is required to achieve a breakdown?
- What do our insights into undervoltage breakdown tell us about a particular applica-

tion: discharge initiation in gas-fed pulsed plasma thrusters?

We will employ a combined theoretical and experimental approach. Our theoretical work will be non-dimensional so as to be universally scalable and we will make simplifying assumptions for analytical clarity. Our experiments are abstracted from thruster hardware or other devices so as to reduce the number of complicating physical phenomenon while illuminating important fundamental processes.

1.3 Organization of This Thesis

We begin in Chapter 2 by reviewing some of the more important contributions to the understanding of breakdown physics in general, then discuss previous work that involved undervoltage breakdown specifically. This discussion has a dual purpose: we wish to establish a theoretical framework on which to base our own investigations, and also to review the state of this field of research so as to identify questions that still need to be explored. Chapter 3 contains a discussion of our theoretical work with undervoltage breakdown, reaching conclusions about the conditions under which the phenomenon will occur that are universally applicable.

We discuss our experimental investigations in Chapters 4 and 5, outlining the experimental setup, methods and results; comparing those results with our theoretical work; and identifying important insights into the phenomenon[1].

In Chapter 6, we turn to a specific application, focusing on the gas-fed pulsed plasma thruster. We outline the parameter space such a device is likely to inhabit and identify the requirements, with regards to plasma conductivity and breakdown time, a discharge initiation system must satisfy. We then use our fundamental insights into undervoltage breakdown to set some guidelines on how to construct a successful GFPPT triggering mechanism.

[1]Much of the theoretical and experimental work has been published in [18].

We conclude in Chapter 7 by summarizing our important findings and identifying areas of research in which work still needs to be done.

Chapter 2

Theoretical Background and Previous Work

In this chapter we review selected works that are relevant both to undervoltage breakdown and to breakdown physics in general. Our purpose is twofold: we seek not only to highlight the accomplishments of the past so as to identify research questions that still need to be answered, but also to establish a theoretical framework on which to base our own studies.

2.1 Breakdown Physics

2.1.1 The Townsend Breakdown

The first description of the fundamentals of steady-state gas discharges was put forth by Townsend [19], and the most well-understood form of breakdown bears his name. In a Townsend breakdown, a voltage is placed across two electrodes of a gas-filled discharge gap. Electrons, present in the gap due to natural processes such as high-energy muon interactions, are accelerated by the electric field and undergo ionizing collisions which produce more electrons:

$$\frac{dn_e}{dx} = \alpha(E,p)n_e, \tag{2.1}$$

where n_e is the electron density in particles per unit volume. α, the number of ionizing collisions per unit length that a single electron undergoes, is related to the electric field E and pressure p [20]:

$$\alpha = Ape^{-Bp/E}, \tag{2.2}$$

where A and B are empirical coefficients characteristic of a given gas[1]. The process of electron production through electron impact ionization is often referred to as the "α process," in contrast with a "γ process" that introduces electrons through secondary emission from a surface.

Equation 2.1 does not explicitly treat electron loss, though loss mechanisms such as recombination and diffusion could be subsumed into the empirical coefficients. Solving for n_e gives a gain coefficient for electron multiplication:

$$\frac{n_e(x)}{n_e(0)} = \exp\left[\int_0^x \alpha(x')dx'\right]. \tag{2.3}$$

Since each ionizing collision produces an electron and an ion, we see from Equation 2.3 that an electron that starts at the cathode and drifts to the anode a distance d away will produce

$$\exp\left[\int_0^d \alpha(x')dx'\right] - 1$$

ions. These ions will eventually drift back to the cathode. On impact with that surface, ions will release secondary electrons. The secondary electron emission coefficient, γ, is the ratio of emitted electrons to incident ions. Thus, each electron at the cathode will ultimately produce

$$\mu = \gamma\left[\exp\left(\int_0^d \alpha(x')dx'\right) - 1\right] \tag{2.4}$$

secondary electrons at the cathode. We call μ the breakdown parameter. The secondary electrons will undergo the same process as the original electron, each producing μ "third generation" electrons, which in turn produce more electrons and so on. We can see,

[1]This is the most common form in which α is expressed, but not the only one. See Section 3.2.

therefore, that if

$$\mu > 1 \tag{2.5}$$

the current in the gap will quickly increase. This is the criterion for breakdown as defined by Townsend [21]. The criterion is a function of cathode material, electrode separation

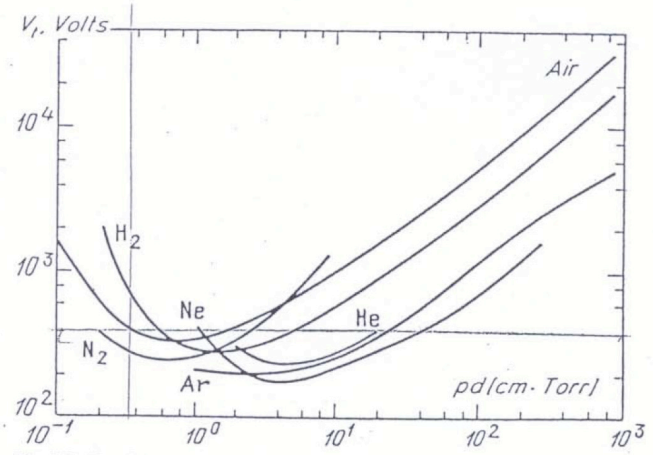

Figure 2.1: Paschen curves for various gases. Reprinted from [21], originally from [22, 23].

and shape, gas, neutral density, and electric field. Thus, for a given set of parallel-plate electrodes filled with a given gas at a given pressure, we can find the voltage for which this condition is met, called the breakdown voltage. Setting $\mu = 1$, assuming a uniform electric field $E_0 = V/d$ across the gap, and solving for V gives the well-known relationship between the breakdown voltage V_B, the gas pressure, and gap width:

$$V_B = \frac{Bpd}{\ln(A/\ln(1 + 1/\gamma)) + \ln pd} \tag{2.6}$$

Note that the product of neutral gas pressure and gap width, pd, is a scaling parameter for breakdown. Paschen curves, plots of the breakdown voltage as a function of pd, for various gases are plotted in Figure 2.1. Undervoltage breakdown can thus be thought of as setting a discharge gap at a voltage below V_B, or alternatively, with $\mu < 1$, then triggering a discharge through the injection of a pulse of electrons.

We can calculate that the pd value at which the breakdown voltage is minimized,

$$(pd)_{\text{min}} = \frac{e}{A} \ln\left(\frac{1}{\gamma} + 1\right), \tag{2.7}$$

and the minimum breakdown voltage,

$$V_{\text{min}} = \frac{eB}{A} \ln\left(\frac{1}{\gamma} + 1\right), \tag{2.8}$$

where e is the base of the natural logarithm, are both functions of the gas coefficients and surface material. The reduced electric field (E/p) at the minimum, however, is only a function of the gas:

$$\left(\frac{E}{p}\right)_{\text{min}} = B. \tag{2.9}$$

2.1.2 Streamer Breakdown and the Raether Criterion

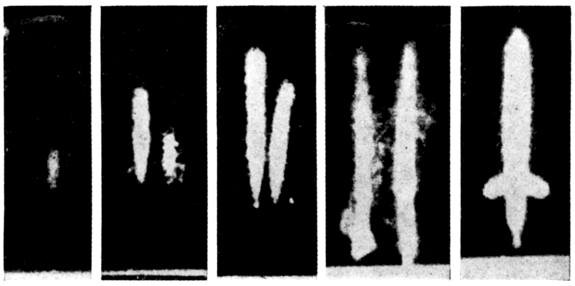

Figure 2.2: High speed photographs of streamer breakdowns [15]. A streamer is a well-defined region of plasma formation around a single electron avalanche.

Streamer breakdown is a phenomenon that is qualitatively different from Townsend breakdown. First observed experimentally by Raether in the 1930s [15], streamer breakdown is characterized by narrow, well defined regions of bright plasma produced by single electron avalanches. They result in significant current rise and self-sustaining plasma in less than one electron transit time (Figure 2.2). Though there exists some controversy over the exact nature of streamers [24], it is generally agreed that streamer breakdown is a space charge phenomenon; a streamer occurs when an electron avalanche becomes

so large that the electric field it produces at the avalanche front greatly enhances the amount of ionization there. Also commonly thought to be a feature of streamers is the role of advanced photoionization in which photons emitted from the avalanche plasma ionize neutrals ahead of the avalanche front.

In 1939, Raether issued his well-known criterion for streamer breakdown [25], empirically observing that a discharge gap will likely form streamers if the avalanche gain ($e^{\alpha d}$) reaches approximately 10^8. As described in his textbook [15], Raether deduced the criterion by balancing the electric field at the front of an avalanche with the applied electric field.

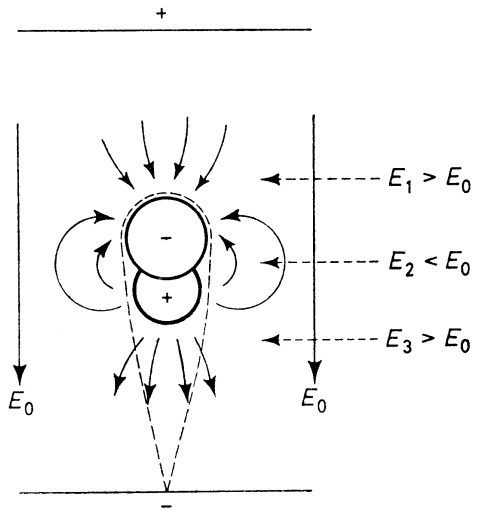

Figure 2.3: Electric field around a high-gain avalanche, reproduced from [15]. Raether used a two-dimensional argument to compare the electric field at the front of a single-electron avalanche to the applied field.

His argument employed the two-dimensionality of an avalanche at high-gain that starts from a single electron, arguing that after an avalanche has traveled a distance x, the charge at the avalanche front can be approximated as a sphere (see Figure 2.3). The electric field resulting from this spherical charge distribution is:

$$E_r = \frac{e \exp(\alpha x)}{4\pi\epsilon_{e0} r_D^2}. \tag{2.10}$$

r_D, the radius of the sphere, is the distance electrons will diffuse in the time of avalanche transit:

$$r_D^2 = 4Dt = 4D\frac{d}{v_d}, \tag{2.11}$$

where D is the electron diffusion coefficient and v_d the electron drift velocity. Speculating that streamers are space charge-induced phenomena, Raether hypothesized that a streamer would form when this space charge field was equal to the field induced by the applied voltage. By inserting values typical of streamer discharge experiments: gap widths on the order of centimeters and pressures on the order of 100 Torr, Raether found that his criterion will be met when $\alpha d \approx 20$, or $\exp(\alpha d) \approx 10^8$, which agrees with experimental observations.

Review of the literature reveals many citations of the "Meek-Raether criterion" for streamer breakdown or the "Raether limit" on the maximum gain a discharge gap can achieve without breaking down (see, for example, [26–32]). These can especially be found in the gas avalanche particle detector community where the gain limit on a particle counter determines the sensitivity of such a device. However, upon such review, one encounters two fundamentally distinct interpretations of this limit. Many describe the criterion, as Raether originally did, as a limit on the avalanche gain a discharge gap can reach before it is likely to breakdown through the streamer mechanism. The criterion thus specifies a relationship between gap width, voltage, and gas pressure only (given gas composition.) Others, however, express the Raether criterion as a maximum number of electron-ion pairs an avalanche can contain before forming a streamer. This interpretation thus includes a constraint on the number of injected electrons a discharge gap can handle without breaking down. The two interpretations are equivalent for an avalanche that is originated by a single electron, but the second interpretation allows for the possibility of an avalanche that is caused by a burst of electrons, provided that the burst is from a small, localized area. In this case, the Raether criterion can be re-written:

$$N_{e0}e^{\alpha d} \approx 10^8, \tag{2.12}$$

where N_{e0} is the number of electrons in the initial burst.

If a burst of electrons causes streamer formation and breakdown in a discharge gap that otherwise would not have broken down, then that gap is experiencing undervoltage breakdown. The Raether criterion can thus be thought of as a form of the threshold criteria that we seek. However, while the Raether limit has proven to be extremely useful in the community from which it originated, it is not a complete description of undervoltage breakdown for several reasons. First, it describes only streamer breakdown, or phenomena that occur during the first electron transit time. The criterion does not describe "Townsend-like" effects of multiple avalanche generations. Second, Raether relied on his two-dimensional picture of a single avalanche initiating from a small area and expanding into a roughly spherical wavefront. The criterion thus works well for high-gain discharge gaps in which the number of introduced charge carriers is much less than the number the avalanche will eventually contain. It does not describe undervoltage breakdown at lower gain, in which a much larger number of electrons is required to sufficiently distort the electric field. In such a situation, the space charge distortion will depend much more strongly on the geometrical distribution of the injected charge. Finally, the quantitative and empirical nature of the criterion, arriving at the conclusion that 10^8 electrons will achieve streamer formation for centimeters-wide discharge gaps at hundreds of Torr, limits its applicability to experiments operating in different parameter regimes.

2.2 Undervoltage Breakdown

Previous work on undervoltage breakdown has primarily been carried out by researchers in three areas: those studying electron avalanches in order to understand the fundamentals of breakdown physics, those investigating gas-avalanche particle detectors in which breakdown is undesirable, and those studying gas switching technology who seek controllable, triggerable, high-current and/or high voltage switches. In this section we review these works in order to understand the insights gleaned and the questions that remain

unanswered.

2.2.1 Electron Avalanche Studies

Much of the experimental work investigating undervoltage breakdown has been carried out in the interest of exploring the phenomena relevant to breakdown physics in general, specifically the effect of space charge on the transient development of current during a breakdown.

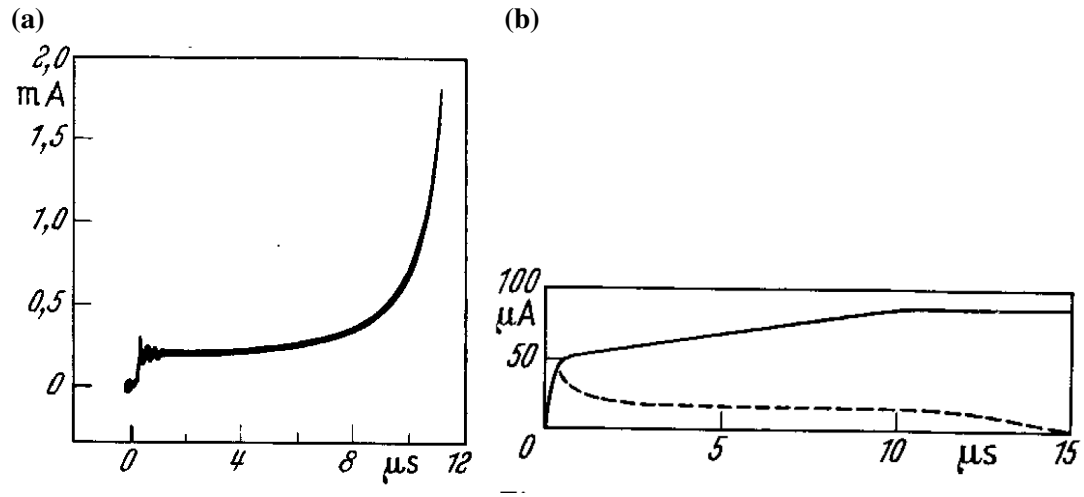

Figure 2.4: Kluckow's experimental results [1]. (a) Current started from a UV light flash with E/p =20 V cm^{-1} Torr^{-1} ; pd=824 cm Torr (20°C); d=2.5 cm; N_{e0}=2×10^6;$\mu_0 = 0.6$. (b) Current rise as calculated without the influence of space charge (- - - -), and as measured with E/p =20.4 V cm^{-1} Torr^{-1}; pd=824 cm Torr (20°C); d=2.5 cm; N_{e0}=4×10^5;$\mu_0 = 0.69$ (——)

The first example of this is the work carried out by Kluckow [1], who used ultraviolet light flashes focused onto the copper cathode of 2.5 cm discharge gap filled with hydrogen to 300 Torr. For some of the results he presents in that work, initial conditions were chosen such that $\mu_0 < 1$, and intense light flashes were used to produce large initial pulses containing on the order of 10^5 to 10^6 electrons. In Figure 2.4 (a) we see the current trace of an undervoltage breakdown event; the first few avalanche generations are apparent as the initial oscillations preceding the gradual, monotonic current rise. In (b), Kluckow demonstrates that this current growth is the result of space charge by overlaying a similar

experimental current trace with one calculated neglecting field distortion.

While Kluckow's aim was to demonstrate and explain the importance of space charge to avalanche formation and current development in a conventional discharge, he made important contributions toward understanding undervoltage breakdown. Aside from being the first to experimentally achieve the phenomenon in a controlled manner, he also convincingly showed that the phenomenon is the result of space charge distortion.

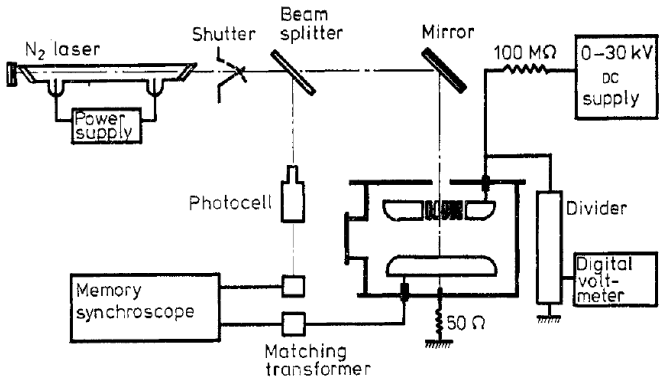

Figure 2.5: Experimental arrangement of Sato and Sakamoto [2]

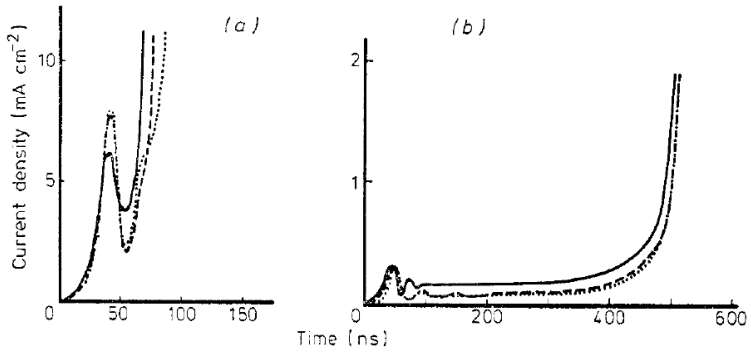

Figure 2.6: Comparison of theory with experiment from Sato and Sakamoto [2] in air at 20 Torr with a voltage at 99% of the breakdown voltage. Case (a) is for N_{e0}=5.53$\times 10^7$, case (b) for N_{e0}=5.53$\times 10^5$. In each case, the solid line represents experiment while the dotted or dashed lines represent theory.

More extensive work was carried out by Sato and Sakamoto [2], who investigated the phenomenon in air at pressures of 20 and 200 Torr using UV laser flashes to provide the initial electron pulses. Their experimental arrangement is diagrammed in Figure 2.5.

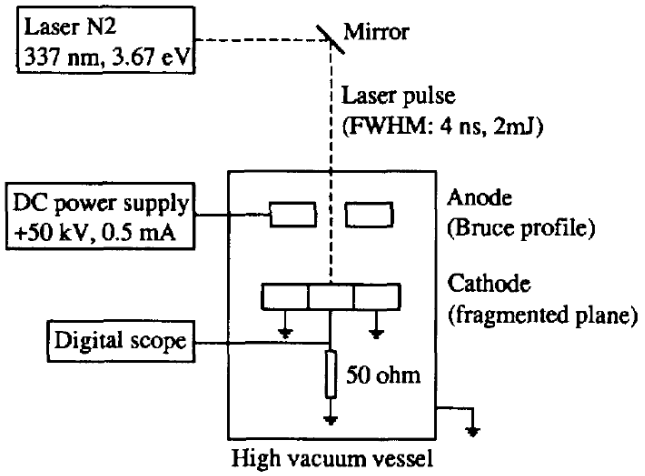

Figure 2.7: The experimental setup of Frechette et al. [3]. The electrodes were designed to produce a non-uniform electric field profile. The anode has a hole which admits the laser and the cathode is made up of concentric discs held at different potentials.

Those authors also developed a thorough theoretical model of the phenomenon, taking into account such physical phenomena as photon feedback from the cathode and the effect of negative oxygen ions. Those results are compared with experimental current traces in Figure 2.6.

Sato's and Sakamoto's model displayed good agreements with their experimental results, and they were able to uncover numerous insights into undervoltage breakdown: they modeled the development of electric field during an electron avalanche and demonstrated and explained a wide range of breakdown delay times occurring at a variety of initial conditions. Perhaps most significantly, they concluded that at low pressures, undervoltage breakdown is dominated by secondary emission from the cathode, while electron detachment due to ionization of the neutral gas atoms is predominant at higher pressures. Still, their findings were somewhat specific to the particular conditions of their experimental arrangement, especially with regard to the complex chemistry associated with a mixture of molecular gases.

Other examples of experiments designed to achieve undervoltage breakdown as a means of exploring avalanche physics include those carried out by Frechette, Bouchelouh, and Larocque at the Ecole Polytechnique in Quebec [3], as well as work done by

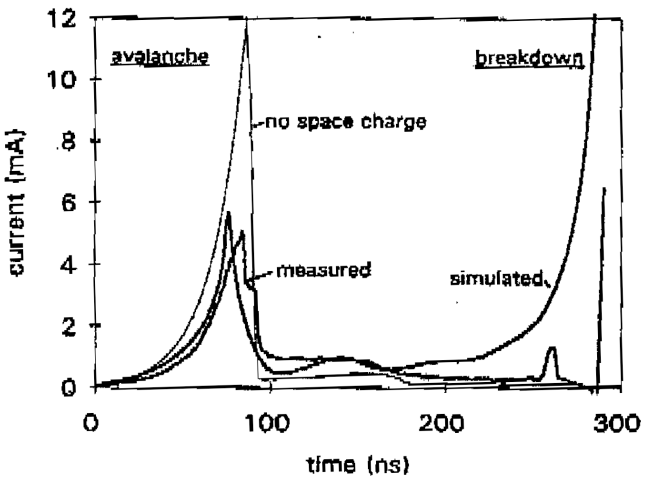

Figure 2.8: Current traces from Kennedy et al [10]. The measured current is overlayed with the result of the simulation calculated both with and without space charge distortion.

Kennedy et al. [10] at Eindhoven University of Technology in the Netherlands. In the Canadian experiment, the authors used electrodes that produced a non-uniform electric field profile, as diagrammed in Figure 2.8. This apparatus was used to measure time-resolved electron avalanches. The Dutch group performed an experiment similar to that of Sato and Sakamoto using atmospheric air and N_2, and developed a numerical simulation of the phenomenon. The conclusions of both these groups reiterate the findings of others that space charge plays a significant role in the development of avalanches.

2.2.2 Gas Avalanche Particle Detectors

Gas avalanche particle detectors represent the first and most commonly used devices in which undervoltage breakdown is observed. Such a device uses the ionization trail left over from a high-energy particle as the externally applied source of charge carriers. The devices are designed to minimize secondary avalanche generations, either through choice of fill gas and cathode material or electronically, and thus read only the charge resulting from the initial particle event.

One type of avalanche detector, the proportional counter [33], is particularly relevant because it employs two electrodes across which a voltage is placed that is below the breakdown voltage, but high enough that significant charge amplification through avalanching occurs. While these devices are designed specifically to *not* break down when charge is introduced, researchers seeking to understand their limits have contributed insight into the conditions under which breakdown at an undervoltage can occur.

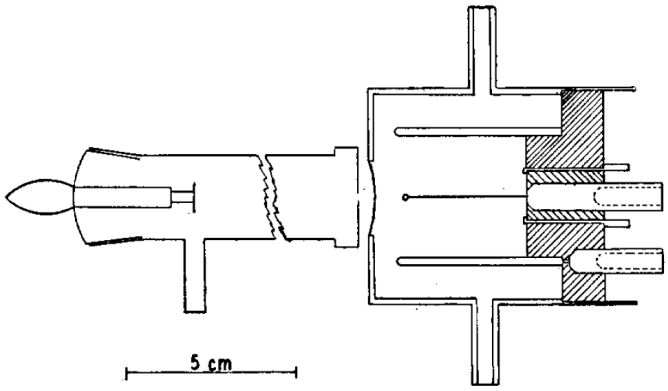

Figure 2.9: A diagram of a Geiger-Klemperer proportional counter [34]

The first proportional counter was introduced by Geiger and Klemperer in 1928 [35] and used a wire situated coaxially with a cylindrical electrode (Figure 2.9). Others followed [34, 36–38] along with a version using using parallel-plate electrodes instead of cylindrical [39].

Gas avalanche particle detectors typically operate at relatively high pressures (signif-

icant fractions of, and greater than, 1 atm), and are therefore fertile ground for streamer breakdown. As a result, Raether's criterion for streamer formation represents the upper limit on the amount of introduced charge a gas avalanche particle detector can handle before it breaks down. Since many gas avalanche detectors, especially proportional counters, are designed to operate below the breakdown limit, streamer formation in one of those devices is an example of undervoltage breakdown.

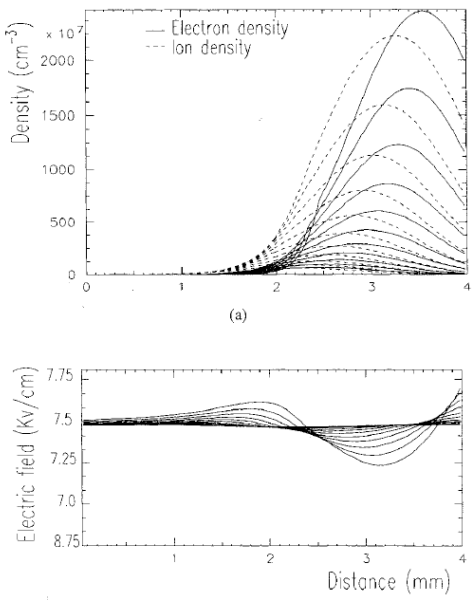

Figure 2.10: Development of densities and electric field during a single avalanche as calculated by Fonte [6]

Fonte and his collaborators [11] have performed thorough studies of the breakdown characteristics of parallel-plate avalanche chambers (PPACs). In [6], Fonte has carried out a more specific calculation of breakdown in one of those devices, calculating the development of electron and ion densities and electric field during the electron avalanche (Figure 2.10). In that work, he used his numerical model to calculate the breakdown limit for a range of gas pressures (Figure 2.11).

Because PPACS break down through the streamer mechanism, Fonte's work represents a verification and more specific calculation of the Raether limit, as well as a demonstration of the relative insensitivity of this limit to gas composition.

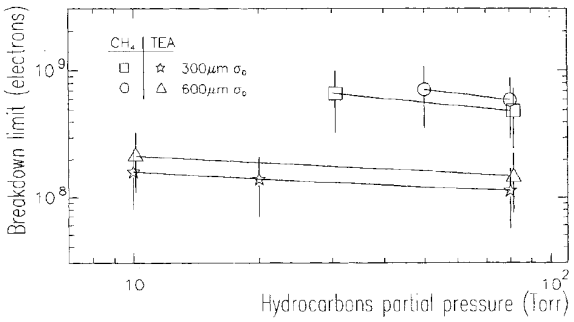

Figure 2.11: Breakdown limit of a parallel-plate avalanche chamber from [6]

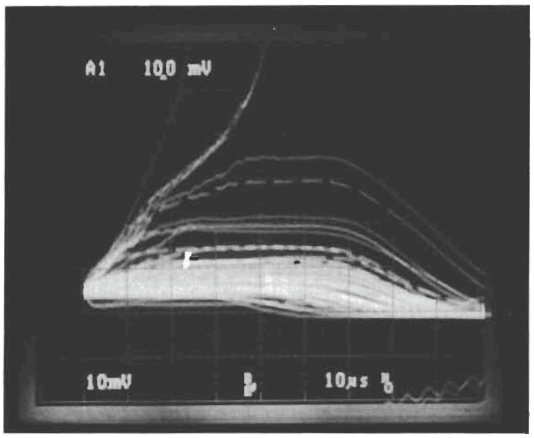

Figure 2.12: Current measurement traces from Fonte et al [11] of the effects of varied pulse sizes in a PPAC. For some pulses, breakdown is induced over a timescale of 10s of μs.

Another important observation reported by this group is the existence of two distinct breakdown timescales. In Figure 2.12 oscilloscope traces of current measurements in a PPAC are displayed. Pulses of varying sizes yield different behavior; some result in fast current rise and breakdown. The timescale of this breakdown, on the order of 10 μs, suggests the buildup of several avalanche generations akin to a Townsend breakdown.

In Figure 2.13, however, a single pulse produces breakdown on a much faster scale, on the order of 10 ns. This corresponds to the timescale of one electron transit across the gap and suggests a streamer-like behavior.

What is particularly interesting about these two experiments is that they took place at the same pd. The parameter spaces in which Townsend and streamer breakdown mechanisms are likely to occur are usually thought to be defined by pressure and overvoltage.

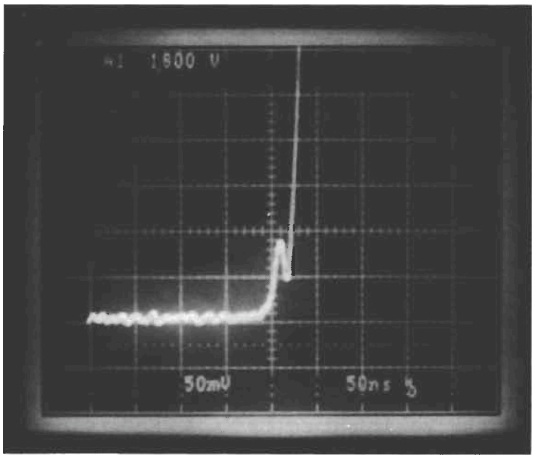

Figure 2.13: A faster breakdown on the order of 10 ns.

Here a group of researchers was able to induce both mechanisms at an undervoltage and without varying the pressure. Their method involved introducing “quencher” gases into the system, suppressing secondary emission through photon feedback and preventing the development of further avalanches. They showed that increasing the concentration of quenching gases makes slower breakdowns less likely and faster breakdowns more likely.

2.2.3 Switching Technology

Because it presents the possibility of on-demand discharge triggering, undervoltage breakdown takes place in many switching devices for pulsed power applications (the GFPPT is one example). This is an active and well-developed field, and many different devices have been researched that employ a wide variety of triggering techniques.

Undervoltage breakdown through space charge distortion as a result of injected charge carriers is only one of a number of phenomena that may or may not be at work in any given device. Others include electric field distortion by external electrodes; interactions between the gas molecules and photons, resulting either from bombardment processes during the course of the discharge, preliminary pre-discharges, or external sources; electrode processes including vaporization, release of adsorbed gases from electrodes, and thermionic emission of electrons or ions from electrode surfaces; "pseudospark breakdown" at low pressure [14]; or thermal effects changing local gasdynamic behavior. Here we discuss triggered spark gap applications where undervoltage breakdown through space charge distortion is at least thought to play a significant role in initiating the discharge.

In a triggered spark gap, two electrodes hold off the voltage to be switched until some form of trigger is applied. One example is the trigatron, introduced by Craggs, Haine, and Meek [13], in which the trigger is a high-voltage pulse applied to a third electrode placed between the electrodes (Figure 2.14). A preliminary discharge forms between the trigger electrode and one of the primary electrodes, and this discharge initiates the main discharge. In [8], it is proposed that the preliminary spark results in a large pulse of electrons being released from the cathode. This pulse in turn distorts the electric field, enhancing ionization. This is undervoltage breakdown as we have described it.

Many techniques for triggering spark gaps involve the use of optical pulses, either through flashlamps or lasers [40]. In some cases, this is manifested in the use of a laser to interact with gas at high pressure causing pre-ionization and/or direct optical breakdown (see, for example, [41]); such a device probably does not employ undervoltage break-

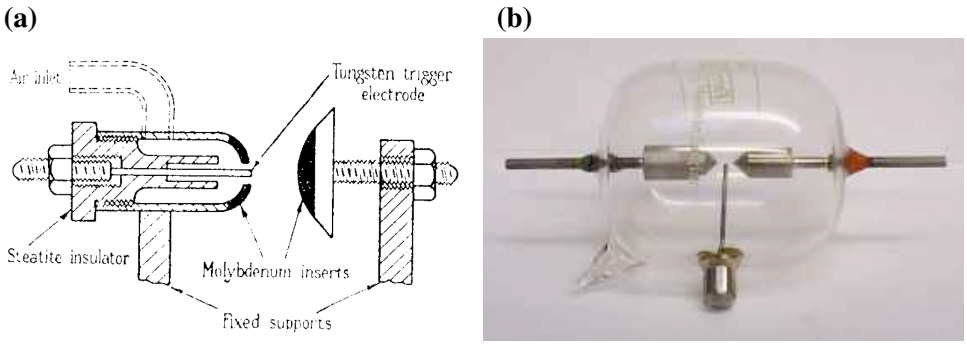

Figure 2.14: Two different electrode arrangements in trigatron switches. In (a), (from [13]) the trigger electrode is inside the anode, while it lies between the electrodes in (b).

down through space charge distortion. However, some triggered spark gap concepts use laser-surface interactions as sources of electrons to induce breakdown (see [42]), and undervoltage breakdown is more relevant in these devices.

2.3 Undervoltage Breakdown: Insights from Previous Work

Undervoltage breakdown has been studied to various degrees in a variety of different research settings. The most important conclusions that have been reached about the phenomenon are:

- Undervoltage breakdown occurs through space charge distortion of the electric field as a result of the initial electron avalanche.
- Higher pressure exaggerates the role of space charge.
- The delay between the introduction of the initial pulse and breakdown depends on the size of the initial pulse and the relative significance of photon-induced secondary emission from the cathode.
- The Raether limit, stating that an avalanche will form a streamer if it reaches on the order of 10^8 electrons, can be roughly thought of as a threshold criterion for

undervoltage breakdown when streamer formation is likely to occur: in high-gain discharge gaps with separation distances on the order of 1 cm and pressures on the order of 100 Torr and when secondary avalanching has been suppressed through gas choice.

- A slow, Townsend-like breakdown mechanism can also occur at lower and intermediate gain.

The phenomenon has been experimentally achieved numerous times and theoretical models of significant sophistication have been produced that agree well with the experimental data. However, in each case, the goal of the theoretical work was to simulate or describe one specific experiment. A more fundamental approach, reaching conclusions that are universally applicable, has to our knowledge never been undertaken. In addition, the issue of undervoltage breakdown threshold criteria has only been partially addressed; no investigation of this quantity for Townsend-like breakdown at low gain has been undertaken.

These issues are the primary focus of the work presented in this thesis. The research questions described in Section 1.2: an understanding of the mechanism behind undervoltage breakdown; the conditions under which it will be possible; and the number of injected electrons required to achieve breakdown, will be addressed with the goals of fundamental understanding and universal applicability. To that end, our approach will be non-dimensional so as to be universally scalable and many physical assumptions will be made on the basis of analytical clarity. Our experiments are simplified and abstracted from thruster hardware or other devices so as to reduce the number of complicating physical phenomenon.

Chapter 3

Undervoltage Breakdown Theory

3.1 Introduction

The investigations discussed in Chapter 2 explored a wide range of conditions and different physical phenomena were found to be more or less relevant in different parameter regimes. They all agree, however, that undervoltage breakdown is caused by a distortion of the space charge distribution in the discharge gap resulting from the charge imbalance produced by the electron avalanche. The space charge distortion in turn distorts the electric field, increasing locally the Townsend ionization coefficient, α, so that ionization increases to the point where breakdown occurs.

To this point, no general, fundamental study of the conditions under which the undervoltage breakdown might occur has been undertaken, and that will be our aim in this chapter.

We will begin in Section 3.3 by focusing specifically on the effect that the first electron avalanche has on the amplification of subsequent avalanches. In that section, we will identify dimensionless scaling parameters which describe the electron avalanche problem, and observe an important criticality displayed by one of those parameters. In Section 3.4, we will look at the subsequent avalanches and outline the conditions under which breakdown will occur. Section 3.5 contains calculations of dimensionless threshold curves

describing the minimum areal density of the injected electron pulse required to achieve breakdown for a given set of conditions.

3.2 Assumptions

Before we begin, we will explicitly list the major assumptions we make in the formulation of this theoretical description. For each, we will discuss the conditions under which we expect it to be valid and briefly speculate on how a violation would affect the conclusions. Appendix C contains more details about the specific validity of these assumptions with regard to the undervoltage breakdown experiment.

- **The problem is one-dimensional.** This is obviously a function of geometry; it is true if the electrodes are parallel plates with an aspect ratio large enough that edge effects can be neglected in the region where the discharge takes place. In addition, the electron pulse has to be uniformly distributed over the surface of the cathode, or at least distributed over a wide enough area that electron diffusion can be ignored (in Appendix C, we show that this holds for the undervoltage breakdown experiment). Electric field distributions will be most significantly affected by multi-dimensionality. In one dimension, the electric field at any point is only determined by the total amount of charge on either side of that point, whereas in two dimensions the spatial distribution of that charge is relevant. In addition, transverse fields will be induced by distributions of space charge that are non-uniform in this direction.

  Raether's derivation of his criterion for streamer formation (see Section 2.1.2) is a clear indication that multi-dimensional effects are relevant in avalanche and breakdown physics. However, the role of complex distributions of charge will be heavily dependent on the geometry of the experiment in question. A multi-dimensional treatment would therefore have limited universality. We choose a one-dimensional approach (and a one-dimensional experiment) in the hope that our fundamental insights will be widely applicable, even if our quantitative results are not.

- **Secondary emission is dominated by ion impact at the cathode and γ is independent of electric field.** This assumption likely holds for clean surfaces and discharge gaps with intermediate E/n (10^2-10^3 Td in argon) [43] (see Appendix C for a more detailed explanation). If photoelectric emission is significant, we expect discharge time scales to be reduced. The critical charges for undervoltage breakdown should also be affected, though it is not obvious in what way. We will call on the assumption of constant γ to argue that ionization is the only process affected by field distortions.

  A field-dependent γ could play a significant role in undervoltage breakdown. We will see that the space charge distortion produced by an electron avalanche augments the electric field near the cathode. If such field distortion resulted in a significant change of the effective secondary emission coefficient (either an enhancement or suppression of γ with increasing field is possible, see Appendix C), subsequent avalanches would be affected and breakdown would be more or less likely. It is also relevant that certain secondary emission processes, such as photoelectric emission, are nonlocal effects, depending on the global distribution of E/p as opposed to the value near the cathode. The relationship between a complex field distribution and secondary emission could therefore be non-intuitive.

- **There is no loss of particles.** Recombination, either through a radiative process, a three-body process, or a dissociative process, could be relevant in any given experiment depending on gas composition, pressure, or instantaneous charge density. However, the time scale of a single electron avalanche is usually short compared to the lifetimes associated with these processes, and neglecting them will usually be a valid assumption [21].

  Diffusive loss could be significant depending on the geometry, playing a large role in discharge gaps whose transverse dimension is smaller than the separation distance. In Appendix C, we show that this process is the dominant loss mechanism in our

experiment, though the loss rate is still short compared to the breakdown time scale.

Clearly loss of particles will make undervoltage breakdown less likely and increase the required injected charge.

- **The first Townsend coefficient can be expressed in its standard form.** We assume that the ionization coefficient can be expressed in the form:

$$\alpha = Ape^{-\frac{Bp}{E}}, \tag{3.1}$$

where A and B are gas-dependent constants that are independent of electric field in the range of the perturbation.

The relationship between α, pressure, and field is determined empirically and is most commonly expressed in this form. However, depending on the composition of gas and the range of E/p, various other functional relationships are used, including $\alpha = Ape^{-Bp^k/E}$ [6], and $\alpha = \sum_i A_i pe^{-B_i p/E}$ [43]. Regardless of the form that works best for a given parameter regime, a number of processes are implicitly incorporated into the empirical fit parameters. These include electron kinetics, the energy dependence of ionization cross-sections, other inelastic scattering, recombination loss, and dissociation or other reaction processes. For the most part, relations such as Equation 3.1 are at least approximately correct for a certain range of E/n, and our approach should be valid so long as field distortions are not too large.

One caveat, however, is that we should consider non-local ionization effects, the existence of which could invalidate our approach. The concept of expressing α in the form of Equation 3.1 carries with it the implicit assumption that ionization everywhere can be determined by the local electric field. This holds as long as the electron mean free path is small compared with electrostatic potential gradient length scales. However, in regions of high E/n, such as a fully developed cathode sheath [44], or Townsend discharges on the left side of the Paschen curve [45], this condition is not

satisfied. In such a case, the local energy of the electron will depend on the distance it has traversed and the Townsend approach to ionization will not work.

Cross-sections for inelastic electron scattering, including ionization, tend to have maxima in the range of approximately 20-50 eV [21]. Thus, if electron kinetics are influenced by nonlocal effects such that they gain up to this amount of energy between collisions, the rate of ionization will be higher than that predicted by relations such as Equation 3.1. However, if the electrons gain more than the critical energy between collisions, elastic losses will drop off and the electrons will continually accelerate across the discharge gap. These "runaway" electrons will not contribute to ionization and Equation 3.1 will be an overprediction.

For undervoltage breakdown, then, we also must consider the energy distribution of the injected electrons. Highly energetic electrons will interact differently with neutrals and our local Townsend approach may not be valid.

In Appendix C, we show that, for the parameter space occupied by our experiment, injected electrons are relatively non-energetic. Electron kinetic effects should therefore not play a part in that analysis.

- **The ratio of electron to ion mobility is field-independent.** This will hold as long as each of these parameters is field-independent, an assertion that holds within a given E/p regime. Mobility, however, like ionization, is an energy-dependent inelastic scattering process. Thus, the same caveats for situations of high E/n or energetic electrons that we discussed for ionization will apply.

3.3 Scaling Parameters for the First Electron Avalanche

3.3.1 Formulation

Governing Equations

Our starting point is the fluid-based "classical model" for glow discharges in one-dimensional geometries with non-attaching gases that was originally presented by von Engel and Steenbeck [46] but treated by many other authors (see, for example, [15, 21, 47]). The governing equations are continuity equations for electrons and singly charged ions and Poisson's equation:

$$\frac{dn_e}{dt} = \alpha\Gamma_e - \frac{d}{dx}\Gamma_e \tag{3.2}$$

$$\frac{dn_+}{dt} = \alpha\Gamma_e + \frac{d}{dx}\Gamma_+ \tag{3.3}$$

$$\frac{d^2\phi}{dx^2} = \frac{-e}{\epsilon_0}(n_+ - n_e) \tag{3.4}$$

$$E = -\frac{d\phi}{dx}. \tag{3.5}$$

We assume that the velocities of electrons and ions are the drift velocities so that $\Gamma_{e,+} = n_{e,+}\mu_{e,+}E$ is the flux of each respective species. If we define $x = 0$ as the cathode position and $x = d$ as the anode, then the governing equations are subject to the boundary conditions:

$$\phi(0,t) = 0 \tag{3.6}$$

$$\phi(d,t) = V \tag{3.7}$$

$$\Gamma_e(0,t) = +\gamma\Gamma_+(0,t) + \Gamma_{pulse}(t). \tag{3.8}$$

Equations 3.6 and 3.7 hold the potential difference across the electrodes at that mandated by the applied voltage. Equation 3.8 is the boundary condition for electron flux and the cathode and includes secondary emission from the cathode from ions and photons. γ is the secondary emission coefficient from ion impact on the cathode. We neglect secondary emission due to photon impact. The cathode boundary condition treats the external pulse of electrons:

$$\Gamma_{pulse}(t) = \frac{N_{e0}}{\tau\sqrt{\pi}} e^{-(\frac{t-3\tau}{\tau})^2}. \tag{3.9}$$

τ is the time width of the pulse and N_{e0} is the total number of electrons per unit area to be released during the duration of the pulse. We assume that secondary ion emission due to electron impact at the anode is negligible, so that the inward fluxes of ions at the cathode and anode and electrons at the anode are zero:

$$\Gamma_+^{in}(x = d) = \Gamma_+^{in}(x = 0) = \Gamma_e^{in}(x = d) = 0. \tag{3.10}$$

We use the generally accepted form for Townsend's first coefficient:

$$\alpha(E, p) = Ape^{-(\frac{Bp}{E})}. \tag{3.11}$$

Gas Amplification Factor

Taking into account the possibility of a non-uniform electric field, we can write a differential equation for electron current in the gap:

$$\frac{d}{dx} j_e(x) = \alpha(x) j_e(x), \tag{3.12}$$

which gives

$$j_e(d) = j_e(0) \exp \int_0^d \alpha(x) dx. \tag{3.13}$$

We therefore define

$$\sigma \equiv \int_0^d \alpha(x) dx \tag{3.14}$$

and recognize σ as the gap's electron amplification factor, or the total number of ionizing collisions an electron undergoes during its transit. We can rewrite Townsend's well-known breakdown criterion as:

$$\mu \equiv \gamma(e^\sigma - 1) \geq 1. \tag{3.15}$$

In undervoltage breakdown, we choose $\mu < 1$ as an initial condition. If we neglect the dependence of γ on electric field, we can interpret undervoltage breakdown as an increase in μ resulting from an increase in σ[1]. Clearly, undervoltage breakdown can only be achieved if the space charge distortion has the effect of increasing σ, and we will see that this only occurs in certain parameter regimes.

Similarity Parameters

If we focus our interest only on the effect that the first electron avalanche has on σ, we can neglect ion mobility and secondary emission, so the relevant dimensional parameters and their units are:

$$[p] = \frac{M}{LT^2} \qquad [d] = L \qquad [V] = \frac{ML^2}{QT^2}$$
$$[A] = \frac{T^2}{M} \qquad [B] = \frac{L^2}{Q} \qquad [N_{e0}] = L^{-2}$$
$$[\epsilon_0] = \frac{Q^2T^2}{ML^3} \qquad [e] = Q.$$

From the Buckingham Pi theorem [48], we can calculate that their are four independent, dimensionless parameters that describe our problem. We have identified such a set [18]. It contains:

$$\Pi_1 = \frac{pBd}{V}, \tag{3.16}$$

which incorporates the pressure, voltage, and gas and,

$$\Pi_2 = \frac{N_{e0}ed}{V\epsilon_0} \tag{3.17}$$

which includes the injected pulse density. The third parameter is

$$\sigma_0 = Apde^{\frac{-Bpd}{V}}, \tag{3.18}$$

[1] Raising μ temporarily above unity will not necessarily cause breakdown at an undervoltage. Indeed, $\mu(t) > 1$ is a necessary but not sufficient condition for undervoltage breakdown. This will be addressed in Section 3.4.

the initial value of σ. These three parameters incorporate all of the relevant dimensional values, but a fourth is needed to complete the set. For this we choose σ_1, the value of σ at the instant the initial electron avalanche completes its transit. Using these four similarity parameters, we have reduced the problem to one of calculating σ_1 given Π_1, Π_2 and σ_0.

In the next section, we will carry out a more thorough non-dimensionalization, normalizing every variable so that we can dimensionlessly observe the spatio-temporal development of the electron and ion densities and the electric field as intermediate steps toward calculating σ_1.

Non-Dimensionalization

We normalize each variable, q, to a reference variable, q', to form a non-dimensional parameter, $\overline{q}$, such that

$$\overline{q} \equiv \frac{q}{q'}. \tag{3.19}$$

For α', we choose α_0, the steady-state value of α before the introduction of the electron pulse:

$$\alpha' = \alpha_0 = Ape^{-\frac{Bpd}{V}} \tag{3.20}$$

We also use α_0 to determine the characteristic length:

$$x' = \frac{1}{\alpha_0}, \tag{3.21}$$

which is the electron ionization mean free path. The characteristic velocity is the electron drift velocity with no space charge distortion,

$$v' = \mu_e \frac{V}{d}. \tag{3.22}$$

This allows us to calculate a characteristic time scale,

$$t' = x'/v' = \frac{d}{\mu_e V \alpha_0}. \tag{3.23}$$

The characteristic density is determined from the injected pulse density and the characteristic length scale:

$$n' = \alpha_0 N_{e0}. \tag{3.24}$$

Electric field and potential are referenced to the applied field,

$$E' = E_0 = \frac{V}{d} \tag{3.25}$$

$$\phi' = E'd' = \frac{V}{\alpha_0 d}. \tag{3.26}$$

Our choice of characteristic pressure will be guided by the form of α (Equation 3.11):

$$p' = \frac{E_0}{B}. \tag{3.27}$$

The dimensionless pressure is essentially the inverse of the well-known reduced electric field E/p, and it is equivalent to the first of the dimensionless similarity parameters introduced in the previous section:

$$\bar{p} = \Pi_1. \tag{3.28}$$

The characteristic areal density, against which we will reference our injected pulse density N_{e0}, will be a function of applied voltage:

$$N' = \frac{\epsilon_0 V}{ed}, \tag{3.29}$$

where e is the electron charge. The quantity N' is the density of charge on an electrode due to the applied voltage. The dimensionless pulse density is equivalent to the second scaling parameter:

$$\bar{N}_{e0} = \Pi_2. \tag{3.30}$$

Dimensional Quantity q	Description	Reference Quantity q'
α	ionization coefficient	$\alpha' = \alpha_0 = Ape^{-\frac{Bpd}{V}}$
x	position coordinate	$x' = \frac{1}{\alpha_0}$
d	gap width	x'
v_e	electron velocity	$v' = \mu_e \frac{V}{d}$
v_+	ion velocity	v'
t	time	$t' = x'/v'$
τ	temporal pulse width	t'
n_e	electron density	$n' = \alpha_0 N_{e0}$
n_+	ion density	n'
p	neutral pressure	$p' = \frac{V}{Bd}$
N_{e0}	electron pulse density	$N' = \frac{V\epsilon_0}{ed}$
ϕ	electrostatic potential	$\phi' = \frac{V}{\alpha_0 d}$
E	electric field	$E' = V/d$
Γ	flux	$\Gamma' = n'v'$
μ_+	ion mobility	μ_e

Table 3.1: Dimensional variables and reference quantities used in the calculation.

Normalizing the gap width d to the characteristic length x' gives the third dimensionless similarity parameter:

$$\bar{d} = \alpha_0 d = \sigma_0. \tag{3.31}$$

Table 3.1 summarizes the above discussion by listing all of the relevant variables we will use in our calculation along with the quantities to which each is referenced.

The dimensionless governing equations are:

$$\begin{aligned}
\frac{d\bar{n}_e}{d\bar{t}} &= \bar{\alpha}\bar{n}_e\bar{v}_e - \frac{d}{d\bar{x}}\bar{n}_e\bar{v}_e && (3.32)\\
\frac{d\bar{n}_+}{d\bar{t}} &= \bar{\alpha}\bar{n}_e\bar{v}_e + \frac{d}{d\bar{x}}\bar{n}_+\bar{v}_+ && (3.33)\\
\frac{d^2\bar{\phi}}{d\bar{x}^2} &= -\bar{N}_{e0}(\bar{n}_+ - \bar{n}_e) && (3.34)\\
\bar{E} &= -\frac{d\bar{\phi}}{d\bar{x}} &&\\
\bar{\alpha} &= \exp\left[\bar{p}(1 - 1/\bar{E})\right]. && (3.35)
\end{aligned}$$

The boundary conditions (Equations 3.6-3.10) become:

$$\begin{aligned}
\bar{\phi}(0,\bar{t}) &= 0 && (3.36)\\
\bar{\phi}(\bar{d},\bar{t}) &= \bar{d} && (3.37)\\
\bar{\Gamma}_e(0,t) &= \gamma\bar{\Gamma}_+(0,\bar{t}) + \frac{\bar{N}_{e0}}{\bar{\tau}\sqrt{\pi}}e^{-(\frac{\bar{t}-3\bar{\tau}}{\bar{\tau}})^2}. && (3.38)
\end{aligned}$$

The Criticality of Π_1

In their textbook [46], von Engel and Steenbeck treat the problem of the effect of space charge on the growth of current during the transition from a Townsend to a glow discharge: a classic "stationary" breakdown. In that work, the authors argue that regardless of the distribution of space charge in the gap or the functional form of α, ionization will be enhanced if $\alpha''(E_0) > 0$ but will be suppressed if the opposite is true. Here we use a similar argument to demonstrate Π_1's importance to undervoltage breakdown.

We begin by expanding α to second order about E_0. If we write:

$$E(x) = E_0 + \Delta E(x), \tag{3.39}$$

then the expansion of α about E_0 takes the form:

$$\alpha = \alpha(E_0) + \alpha'(E_0)\Delta E + \frac{\alpha''(E_0)}{2}(\Delta E)^2 + \ldots \tag{3.40}$$

$\sigma = \int_0^d \alpha(x)dx$ can therefore be written as:

$$\sigma = \sigma_0 + \alpha'(E_0)\int_0^d \Delta E dx + \alpha''(E_0)\int_0^d (\Delta E)^2 dx + \ldots \tag{3.41}$$

For this problem, the electrodes are held at fixed potential (the boundary condition expressed in Equations (3.6) and (3.7)), the integral of the electric field perturbation must vanish and the first order term drops out. The perturbation on σ can thus be written simply as:

$$\Delta\sigma = \alpha''(E_0)\int_0^d (\Delta E)^2 dx + \ldots \tag{3.42}$$

The sign of the perturbation on σ is determined only by the sign of $\alpha''(E_0)$, so long as the higher order terms are not significant. The critical value for space charge to enhance ionization is that which gives $\alpha''(E_0) = 0$.

In the case of undervoltage breakdown, this criticality defines two regions of parameter space: one in which space charge distortion enhances ionization and the phenomenon is possible, and one in which space charge distortion suppresses ionization and the opposite is true. We can express the dimensionless α using Equation (3.35) and calculate:

$$\left(\frac{d^2\bar{\alpha}}{d\bar{E}^2}\right)_{\bar{E}=1} = \bar{p}^2 - 2\bar{p} = 0 \Rightarrow \bar{p}^* = 2. \tag{3.43}$$

The importance of the first similarity parameter, $\Pi_1 = \bar{p}$, to undervoltage breakdown is now clear. There exists some critical value of that parameter, $\bar{p}^*$, above which undervoltage breakdown may occur and below which it may not. While this analysis predicts that $\bar{p}^*$ should always be equal to 2, it assumes a second-order field perturbation to arrive at that value. In the next section, we will calculate the true electric field distortion in order to calculate σ_1 and the actual values of $\bar{p}^*$ given the three dimensionless input parameters.

3.3.2 Solution and Results

The Numerical Method

We solve Equations 3.32 - 3.38 numerically using a 1D time-dependent finite-volume method [49]. Equations 3.32 and 3.33 are advection-reaction equations and are solved using an upwind scheme so that at the mth time step at position i,

$$n_i^m = n_i^{m-1} - \frac{v\Delta\bar{t}}{\Delta\bar{x}}(n_i^{m-1} - n_{i-1}^{m-1}) + \Delta\bar{t}\bar{\alpha}_i^{m-1}\bar{v}_e\bar{n}_e, \tag{3.44}$$

where n is either the non-dimensional ion or electron density and v is the relevant non-dimensional drift velocity. Time steps are dynamically calculated to satisfy the CFL stability condition,

$$\Delta\bar{t} = \frac{\Delta\bar{x}}{\max|\bar{v}|}\nu. \tag{3.45}$$

ν is the Courant number and the calculation will be stable so long as $\nu < 1$. We hold it at a fixed value of $.8$. The relevant wave speed during the electron pulse transit is the electron drift velocity, which will be greatest at the electric field maximum. Poisson's equation (3.34) is solved subject to the boundary conditions (3.36) and (3.37) at every time step using a tridiagonal inversion method [50].

Parameter Values

An implicit assumption when discussing undervoltage breakdown is that the initial conditions are chosen so that μ is on the order of but below unity. We can therefore calculate the range of interest of $\bar{d} = \sigma_0$ by setting $\mu = 1$ and calculating what σ_0 will be required for a reasonable range of γ values. Using values ranging from $\bar{d} = 3$ to $\bar{d} = 11$ covers the range of γ from $.1$ to 10^{-5}. However, above $\bar{d} \approx 9$, we have found that any injected pulse large enough to cause any measurable field distortion will in fact cause such a large distortion so as to completely cancel out the applied electric field, causing the field to reverse direction near the anode. In practice, if an avalanche gets this large, streamer physics such as radiative pre-ionization and multidimensional effects would be relevant. This is outside the

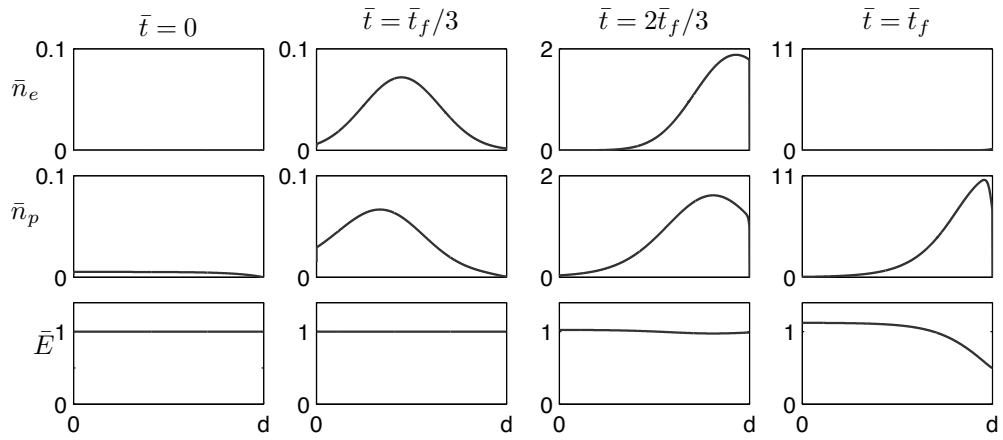

Figure 3.1: Time dependent variation of normalized electron density, ion density, and electric field at various times during the initial electron avalanche transit. Here $\bar{p} = 2.15$, $\bar{d} = 7.08$, and $\bar{N}_{e0} = 4 \times 10^{-2}$. Note the scale changes on the density plots.

scope of the current investigation. The appropriate range of $\bar{d}$ for our purposes thus spans from approximately 3 to 9.

Similarly, we choose a range of $\bar{N}_{e0}$ such that the smallest pulse barely distorts the applied field and the largest value cancels it out. This range varies with the other inputs, but in general spans the orders of 10^{-3} to 10^{-2}.

$\bar{\tau}$, the non-dimensional time width of the injected electron pulse, is held at a fixed value of 2, which is always smaller than the electron transit time. The ratio between ion and electron mobilities, $\bar{\mu_+} = \mu_+/\mu_e$ is held at a fixed value of .01, roughly what it would be for hydrogen. This is the only factor in the non-dimensional model that would be affected by changing the working gas, but ion dynamics should not be relevant on the time scale of interest.

Results

We can now use the dimensionless model to chart the development of the intermediate variables in order to calculate σ_1 as a function of the other three similarity parameters. In Figure 3.1 we plot the spatial distributions of $\bar{n}_e$, $\bar{n}_p$, and $\bar{E}$ before, during, and after

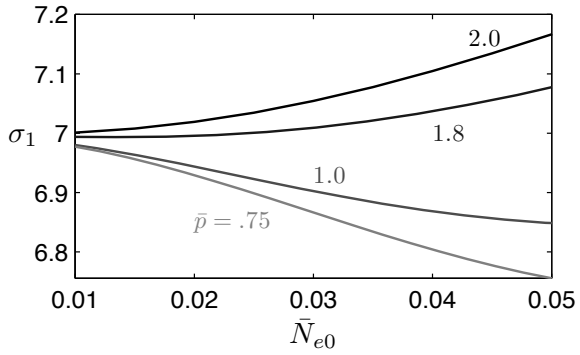

Figure 3.2: σ after the first electron avalanche versus $\bar{N_{e0}}$ for $\bar{d} = 7$

the electron pulse transition as calculated numerically. The electron pulse enters at the cathode, drifts toward the anode, grows due to ionizing collisions, then exits the volume at the anode. Each ionizing collision also produces an ion, so the ion density grows as the electron pulse traverses, but the ions remain stationary on this time scale due to their much lower mobility. Thus, when the electrons exit the volume, the ions they leave behind cause a charge imbalance which distorts the electric field. After the pulse transit, the electric field is augmented near the cathode but diminished near the anode.

It is this electric field distortion which alters the value of σ, but since the electric field is increased in one region and decreased in another, it is not obvious what net effect a pulse will have on gas amplification. Figure 3.2 contains a plot of σ_1 vs $\bar{N}_{e0}$ for several values of $\bar{p}$ (E/p). At high values of $\bar{p}$, gas amplification is in fact enhanced with increasing pulse size and undervoltage breakdown may occur with a large enough pulse. However, at low values of $\bar{p}$, an electron pulse will have the net effect of decreasing σ.

We define $\bar{p}^*$ as the value of $\bar{p}$ at which $\sigma_1 = \sigma_0$. In Figure 3.3, we plot $\bar{p}^*$ vs $\bar{N}_{e0}$ for three different values of $\bar{d}$. For each case, the range of $\bar{N}_{e0}$ was chosen so that the smallest pulse does not significantly distort the electric field and the largest value completely cancels the applied field. We can see that in all cases $\bar{p}^*$ lies between 1.6 and 2, but varies weakly with $\bar{N}_{e0}$: at certain dimensionless pressures, a small amount of space charge distortion will hinder ionization, but a larger amount of distortion will enhance it.

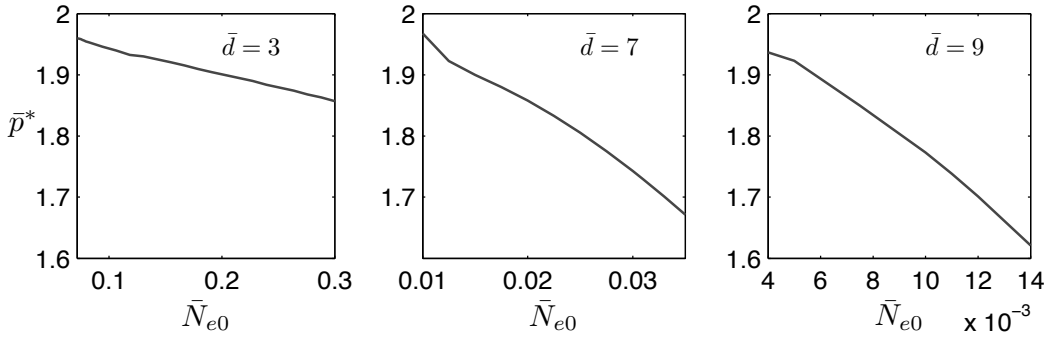

Figure 3.3: Critical dimensionless pressure as a function of $\bar{N}_{e0}$ for various $\bar{d}$

3.3.3 Discussion and Interpretation

Discussion

As seen in Figure 3.3, $\bar{p}^*$ approaches 2, the value predicted by the second-order analysis, at low values of $\bar{N}_{e0}$, but the electric field distortion resulting from a larger pulse is too great to be treated as a second-order perturbation. Still, $\bar{p}^*$ varies only weakly with $\bar{N}_{e0}$ and $\bar{d}$, reaching values as low as approximately 1.6.

These results are consistent with experimental reports of undervoltage breakdown in that review of the literature reveals no reported instance of undervoltage breakdown occurring at dimensionless pressures below 2. Christiansen's original experiment [39] used H_2 with a $\bar{p}$ of 64. Sato and Sakamoto [2] achieved undervoltage breakdown in air at pressures and voltages corresponding to $\bar{p}$ values ranging from 4.4 to 8.5. Frechette et al. [3] used atmospheric N_2 to achieve the phenomenon in a range of $6.3 < \bar{p} < 7.5$. Fonte et al. [11] performed a thorough study of the breakdown limit of parallel-plate avalanche chambers in the presence of X-ray and α sources using noble gases at atmospheric pressure mixed with hydrocarbons such as triethylamine, CH_4, and C_2H_6 at partial pressures ranging from 1-100 Torr. Using the empirically determined values of B they present for their various gas mixtures, we can calculate that dimensionless pressures at which breakdown occurred ranged from 2 to 5.

Physical Interpretation

α, the number of ionizing collisions an electron undergoes per unit length, is controlled by two phenomena: the number of neutrals per unit length and the likelihood that an electron-neutral collision will cause ionization, which in turn is influenced by the amount of acceleration an electron undergoes between each collision. Based on arguments presented by Raizer [21], we can interpret the non-dimensional pressure in terms of the the first ionization energy of the gas, ε_i, and the ionization mean free path, λ:

$$\bar{p} = \frac{pB}{E_0} = \frac{\varepsilon_i / e}{E_0 \lambda}. \tag{3.46}$$

The parameter represents a ratio between the ionization potential and the potential through which an average electron falls between ionizing collisions. (That this parameter could exceed unity with ionization still occurring is not surprising; it is common for only a small fraction of electrons at the high end of the energy distribution function to have enough energy to cause ionization.)

The threshold behavior we observe is therefore a manifestation of a saturation. While increasing electric field will always increase ionization (in the absence of runaway effects) and decreasing electric field will always decrease it, one effect may be more or less sensitive to such changes, depending on $\bar{p}$. At low values of $\bar{p}$, there exists enough of a potential difference between ionizing collisions that a large fraction of the electrons have enough energy to ionize and ionization is limited by the number of neutral atoms there are to ionize per unit length. Increasing the electric field does not have a large effect on the amount of ionization because the electron distribution is energy-saturated and neutral density-starved; decreasing electric field in this regime has a larger effect on ionization because it reduces the population of electrons with sufficient energy and moves the system away from saturation. Alternatively, at high values of $\bar{p}$, the system is neutral density-saturated but energy-starved. There are plenty of neutrals per unit length, but the system needs a higher fraction of electrons with sufficient energy to ionize, so increasing the energy gain

between collisions has a greater effect on ionization than decreasing it.

At the minimum of the Paschen curve, $E/p = B$, which is equivalent to the statement $\bar{p} = 1$. It is therefore clear that undervoltage breakdown through space charge distortion is only possible on the right-hand branch of the Paschen curve.

3.4 Subsequent Avalanches and Breakdown

3.4.1 Extending the Model to Longer Time scales

In the previous section, we focused our theoretical attention on the first electron avalanche of an undervoltage breakdown event, noting that much can be said about the conditions under which the phenomenon is possible by looking at the effect of space charge on ionization during that early stage of development. We now wish to explore longer-time scale ion dynamics, tracking the development of further avalanches and their progression towards breakdown.

We will use the same formalism, solving Equations 3.32-3.38, and numerical method outlined in the previous section, but since we wish to track ion dynamics, coarser time steps are required. On this time scale, we can assume a steady-state flux distribution at every time step. This allows for replacing Equation 3.32 with the approximation:

$$\bar{\Gamma}_e(\bar{x}, \bar{t}) \approx \bar{\Gamma}_e(0, \bar{t}) \exp \int_0^{\bar{x}} \bar{\alpha}(\bar{x}, \bar{t}) d\bar{t}. \tag{3.47}$$

This approximation is valid so long as the electron flux from the cathode does not change significantly during an electron transit time, an assertion that is true for the majority of the breakdown process. However, that assertion does not hold during the injection of the initial electron pulse. We therefore treat the problem in two phases: Phase 1 starts at $t = 0$ and lasts until the instant the first electron avalanche enters the anode, at which point Phase 2 begins. During Phase 1, we calculate the electron density using the continuity equation (Equation 3.32) and the relevant wave speed used to calculate time steps (Equation 3.45)

is the dimensionless electron drift velocity. We calculate electron density during Phase 2 using Equation 3.47 and use the dimensionless ion drift velocity to calculate the larger time steps.

We will continue to use the three dimensionless inputs $\bar{p}$, $\bar{d}$, and $\bar{N}_{e0}$ (Equations 3.16-3.18), but we will require two additional dimensionless inputs to specify the problem: the secondary emission coefficient, γ, and the ratio of electron and ion mobilities, μ_e/μ_p. In addition, while we do not change the definition of the normalized time coordinate, $\bar{t}$, in the continuity equations, we introduce a new dimensionless time parameter for convenience:

$$\xi \equiv \frac{t}{T_+ + T_e}, \tag{3.48}$$

where $T_{+,e} = d/(\mu_{+,e}E_0)$ are the transit times of the ions and electrons as a result of the unperturbed field. In the absence of space charge effects, 1 ξ would be the duration of one avalanche generation.

3.4.2 Results: Multiple Avalanche Generations

We plot the normalized ion density distribution as a function of ξ for two cases: in Figure 3.4 an injected electron pulse that is not large enough to cause breakdown and In Figure 3.5 a larger pulse which does cause breakdown. The first electron avalanche appears instantaneous on this time scale, so the initial condition is the ion distribution resulting from that avalanche. The ions drift toward the cathode ($\bar{x} = 0$), releasing second-generation electrons due to secondary emission. Those electrons instantaneously result in second-generation ions, which in turn drift toward the cathode, producing further avalanche generations. Since $\mu < 1$ is always an initial condition, we expect each generation to be smaller than the previous in the absence of space charge distortion. For case (a), we see this behavior, as successive avalanches gradually die out in magnitude. For case (b), however, the space charge distortion is large enough to reverse that trend; the avalanches increase in size and quickly bleed together, which will result in breakdown.

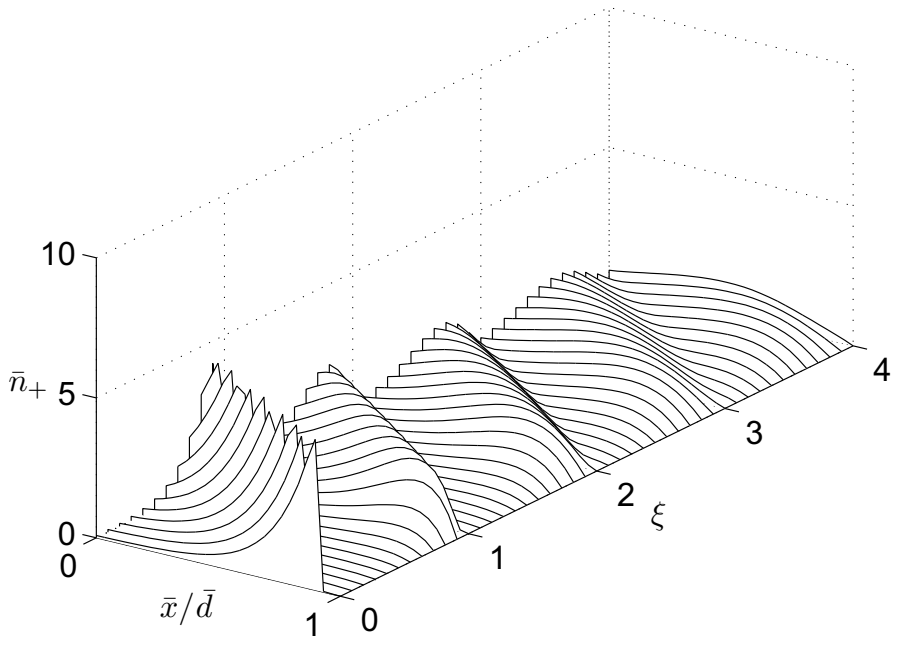

Figure 3.4: Normalized ion density distribution as a function of ξ for $\bar{p} = 2.15, \sigma_0 = 7.2, \gamma = 7.13 \times 10^{-4}, \mu_e/\mu_+ = .004$ and $\bar{N}_{e0} = 5 \times 10^{-3}$. The avalanche generations gradually die out and no breakdown will occur.

The key to achieving breakdown is the ability to raise μ above unity through an increase in σ_0. In Figure 3.6 we plot μ vs ξ for various injected pulse densities. In each case, μ's initial value, μ_0, is .85, but is instantaneously increased as a result of the initial electron avalanche. As successive avalanches develop, μ rises and falls with the redistribution of ion density.

In all cases, μ is made to exceed unity at least temporarily. However, in some cases, μ falls below it again and a breakdown is not achieved. Furthermore, there are cases in which μ exceeds unity, then drops below it, then increases again resulting in breakdown. It is therefore clear that Townsend's classic breakdown condition, $\mu > 1$, does not apply for undervoltage breakdown.

The Townsend model requires positive gain over several avalanche generations in order for breakdown to be achieved. μ is intended to be the ratio of the number of electron-ion pairs in one generation to the previous one. However, the quantity μ varies *during* each ion

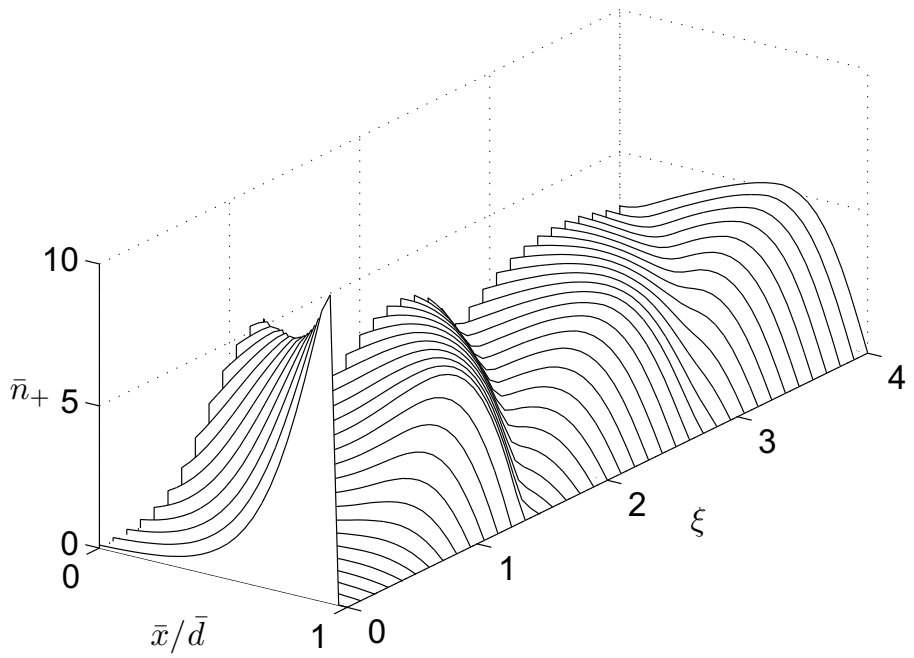

Figure 3.5: Normalized ion density distribution as a function of ξ for $\bar{p} = 2.15, \sigma_0 = 7.2, \gamma = 7.13 \times 10^{-4}, \mu_e/\mu_+ = .004$ and $\bar{N}_{e0} = 1.5 \times 10^{-2}$. Here the avalanches build in magnitude; a breakdown will eventually result.

avalanche transit. It is not surprising, then, that one can instantaneously achieve $\mu > 1$, temporarily producing a lot of next-generation electrons, but not sustain that state for the entire ion transit. In such a case, the total number of charge carriers produced in the next generation might not be greater, and breakdown would not be achieved. Still, it seems obvious that if μ never exceeds unity, a breakdown will never occur. We can thus say that $\mu(t) > 1$ is a necessary but not sufficient condition for undervoltage breakdown.

3.5 Threshold Curves

We now turn our attention to one of the primary research questions we outlined in Section 1.2: given a set of initial conditions that is favorable to undervoltage breakdown, how many electrons are required in the injected pulse to achieve breakdown? Restated in terms of our dimensionless scaling parameters, we seek to find, given μ_0, $\bar{p}$, γ, and μ_e/μ_+, the

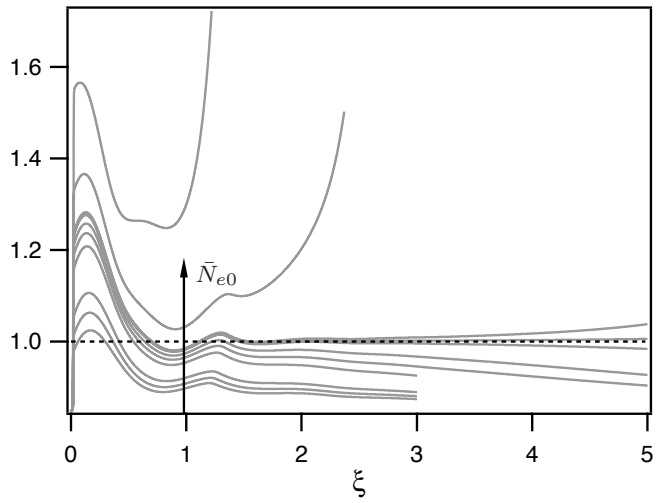

Figure 3.6: The temporal development of μ for various injected pulse sizes.

minimum $\bar{N}_{e0}$ that will result in breakdown[2]. We will call this critical parameter $\bar{N}^*_{e0}$.

To find $\bar{N}^*_{e0}$, we use our theoretical formalism and numerical method outlined in Sections 3.3 and 3.4. For a given set of initial conditions, we choose an initial guess of $\bar{N}_{e0}$ and calculate the development of ion and electron densities and electric field. An event is designated as a breakdown if μ trends upward over several ξ. A next guess is chosen using the method of bisection [50], evaluated, and the process is repeated. The system will converge to within the desired tolerance ϵ of the true critical value in $\log_2(\epsilon_0/\epsilon)$ guesses, where ϵ_0 is the size of the initial interval.

Figures 3.7-3.9 contain threshold curves, plots of $\bar{N}^*_{e0}$ as a function of μ_0, for various values of $\bar{p}$, γ, and $\bar{\mu_+}$.

From these plots, we can distinguish several important trends:

- It is clear that increasing $\bar{p}$ decreases the required number of electrons in all cases.
- Increasing γ increases $\bar{N}^*_{e0}$ because, at constant μ_0, higher γ implies lower σ_0. Since undervoltage breakdown, as we have defined it, is achieved through manipulation of

[2]We will find it more convenient from now on to refer to $\mu_0 = \gamma(e^{\sigma_0} - 1)$ instead of simply σ_0 since σ_0 is constrained such that $\mu_0 < 1$

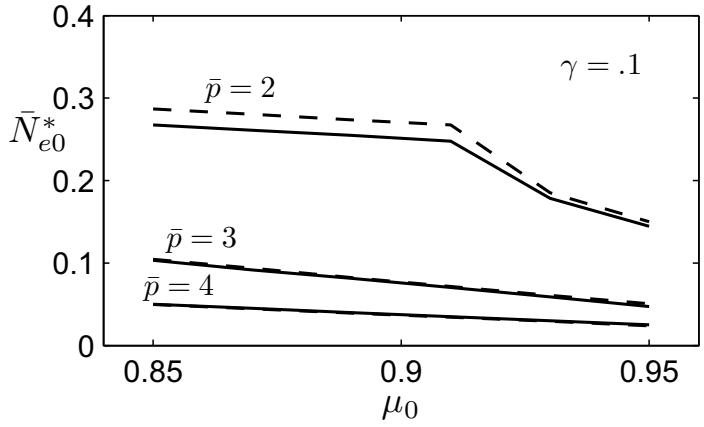

Figure 3.7: Threshold curves for γ=.1, $\bar{\mu}_+$=.004 (solid) and $\bar{\mu}_+$=.01 (dashed)

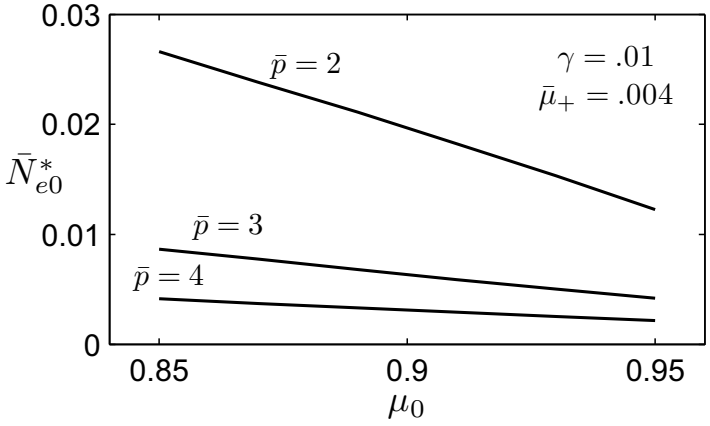

Figure 3.8: Threshold curves for $\bar{\mu}_+$=.004 and γ=.01.

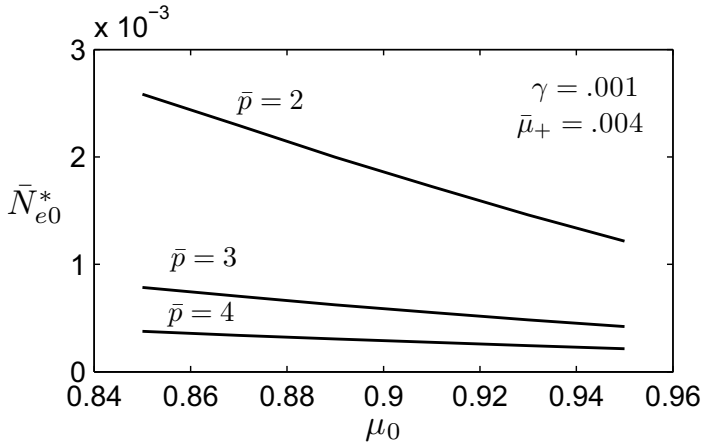

Figure 3.9: Threshold curves for $\bar{\mu}_+$=.004 and γ=.001.

gas amplification and not secondary emission, the phenomenon is more difficult to achieve when the amplification factor is reduced.

- There is a weak dependence on ion mobility. This suggests that breakdown is determined during the first electron avalanche when the field distortion is largest, but ions are stationary.

3.6 Conclusions

Our theoretical investigation of undervoltage breakdown through electron pulse injection in parallel-plate discharge gaps has allowed us to achieve the following physical insights:

- Four similarity parameters universally describe the effect of the first electron avalanche on ionization for subsequent avalanches.
- One of these, $\Pi_1 = Bpd/V$, exhibits a critical behavior, allowing undervoltage breakdown when the parameter exceeds a critical value and prohibiting it otherwise. This critical value varies between 1.6 and 2, depending weakly on two other similarity parameters $\Pi_2 = N_{e0}ed/(\epsilon_0)$ and $\sigma_0 = \alpha_0 d$.
- Bringing μ above unity is necessary for undervoltage breakdown, but not sufficient.

- Increasing Π_1 ($\bar{p}$) makes undervoltage breakdown easier because it increases the degree to which ionization is limited by electric field.

- Whether or not breakdown will occur is decided during, and immediately after, the transit of the first electron avalanche that results from the injected pulse. The phenomenon is therefore insensitive to ion mobility.

Chapter 4

Experimental Setup and Methods

The undervoltage breakdown experiment is designed to measure the minimum injected charge required to achieve undervoltage breakdown for a given set of initial conditions. Intended to be as simple as possible for phenomenological clarity, the apparatus is a parallel-plate discharge gap and argon is used as the working gas. We carried out experiments in which short (10 ns), high-powered laser pulses were directed onto a flat target fixed on the cathode of a set of parallel-plate electrodes. We used this experiment to measure threshold criteria: the number of electrons in an initial pulse required to achieve breakdown for a given set of undervoltage conditions.

We carried out two different series of experiments. In the first, infrared laser pulses of relatively high intensity (up to about 500 mJ) were directed onto a tungsten target. In the second, ultraviolet laser pulses of relatively low intensity ($<$ 4 mJ) were directed onto a copper target, releasing electrons through the photoelectric effect.

The use of infrared laser pulses is a somewhat unique method for inducing undervoltage breakdown as the photons of the laser light do not possess enough energy to release electrons from the metal surface through the photoelectric effect. Indeed, the feasibility of such a technique was only discovered accidentally (see [51]) and explained later (see [52]) as resulting from gases that are desorbed through local heating of the cathode surface, then quickly ionized. Still, thermal modeling of the laser-surface interaction,

discussed in more detail in Appendix A, suggested that, if tungsten were chosen as the cathode material, significant *thermionic* emission of electrons could be achieved without vaporizing the cathode material. It should therefore be possible to build a long-life cathode that does not erode as part of its emission process. In addition, infrared-induced breakdown demonstrated itself to be a relatively robust technique, requiring neither high vacuum levels nor exhaustive surface preparation techniques used by photocathodes.

Still, the heating caused by the high-powered laser pulses inevitably caused the release of adsorbed gases, altering the pressure and gas composition and complicating an experiment that had been designed to be as simplified as possible for physical clarity. Thus, lower-intensity UV pulses were used to produce pure electron pulses through the photoelectric effect from a copper photocathode.

In this chapter, we describe the experimental apparatus used in these experiments and the methods used to carry them out. Results from both the IR and UV experiments will be presented and compared.

4.1 Experimental Setup

4.1.1 Overview

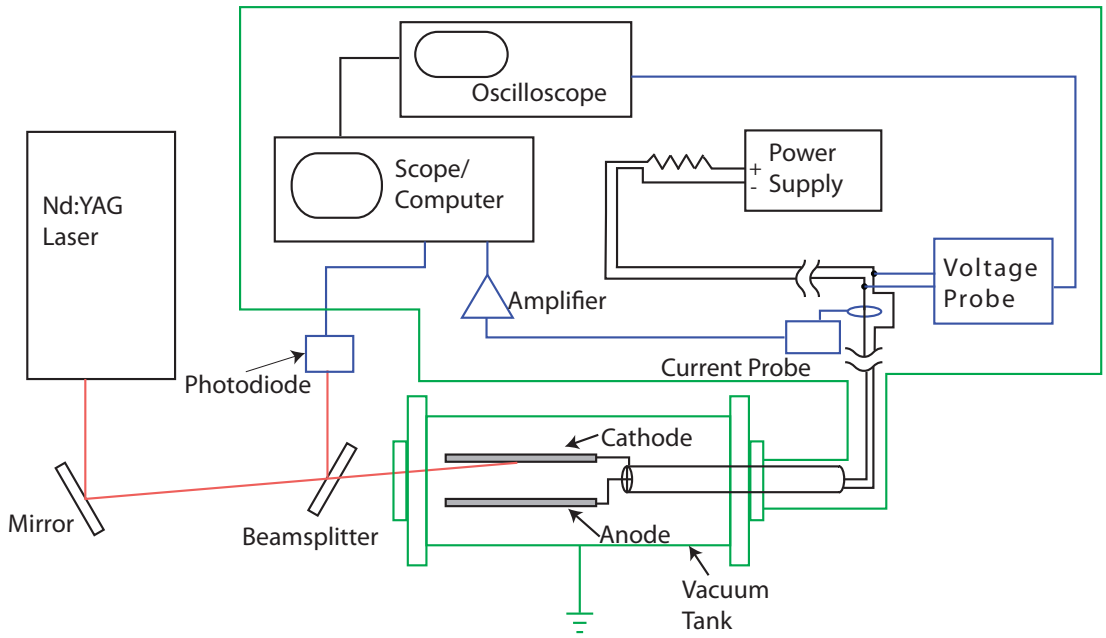

Figure 4.1: Schematic of the undervoltage breakdown experiment. Blue represents measurements, green represents grounded shielding.

Figure 4.1 is a schematic of the undervoltage breakdown experiment. A pulsed Nd:YAG laser is directed to a beamsplitter which reflects a small fraction of the beam onto a photodiode. The bulk of the beam passes through the beamsplitter, then through the window of a vacuum chamber and onto the cathode of a set of parallel-plate electrodes. Current signals are carried from the plates by way of a 50 Ω transmission line and are measured by an amplifier and oscilloscope, which also measures the photodiode signal. The voltage across the plates is measured and recorded by a separate oscilloscope. All measurement electronics sit inside a grounded Faraday cage that isolates them from electromagnetic noise. The system is run by an automated Labview data acquisition system.

Each subsystem is described in more detail in the following sections.

4.1.2 Electrodes

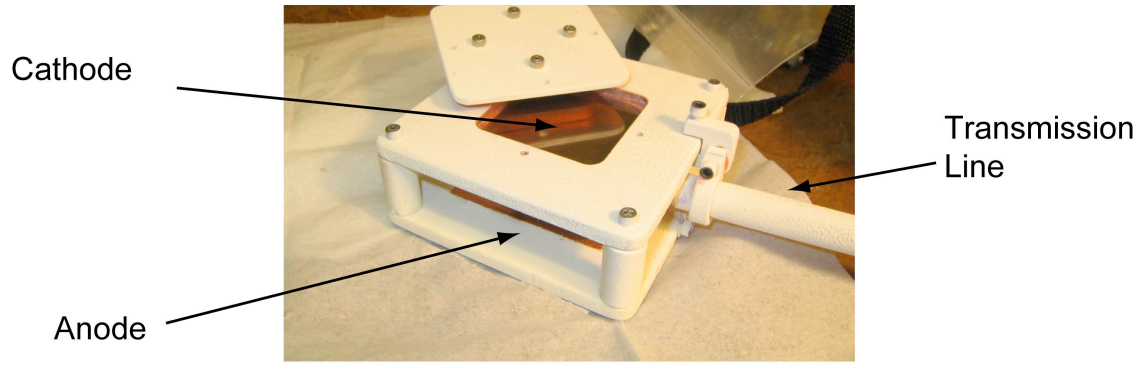

Figure 4.2: Electrodes used in the undervoltage breakdown experiment.

The electrodes are square copper plates, 10 cm on a side and separated by 2.54-cm ceramic spacers. Both plates are covered with boron nitride insulator that can be sprayed on, except for a 7.6 cm by 7.6 cm square conductive region on the inside of the anode. The cathode has a 5 cm by 5 cm cutout into which a laser target plate is placed, then secured with a clamp (Figure 4.2). In the IR experiments, the laser target was tungsten foil while OFHC copper polished to 1μm smoothness was used as a photocathode for the UV experiments. In either case, the arrangement of the conductive areas of the electrodes restricts current conduction to the region in the center of the plates where the electric field is most uniform.

Attached to the electrodes is the 50 Ω transmission line that was specially constructed to be suitable for ultra-high vacuum conditions. The line consists of two coaxial copper tubes, one .125 cm with an inner diameter of 1.1 cm and one .476 cm separated by ceramic spacers. Using the relation for impedance of a cylindrical coaxial transmission line [53]:

$$Z_0 = \frac{2}{2\pi}\sqrt{\frac{\mu_0}{\epsilon_0}}\ln\frac{b}{a}, \tag{4.1}$$

with b the inner diameter of the outer conductor and a the outer diameter of the inner conductor, we get Z_0=50.597 Ω. The outer conductor is coated with boron nitride. The

transmission line is terminated with a standard BNC connector which attaches to a BNC vacuum feedthrough.

4.1.3 The Vacuum Facility

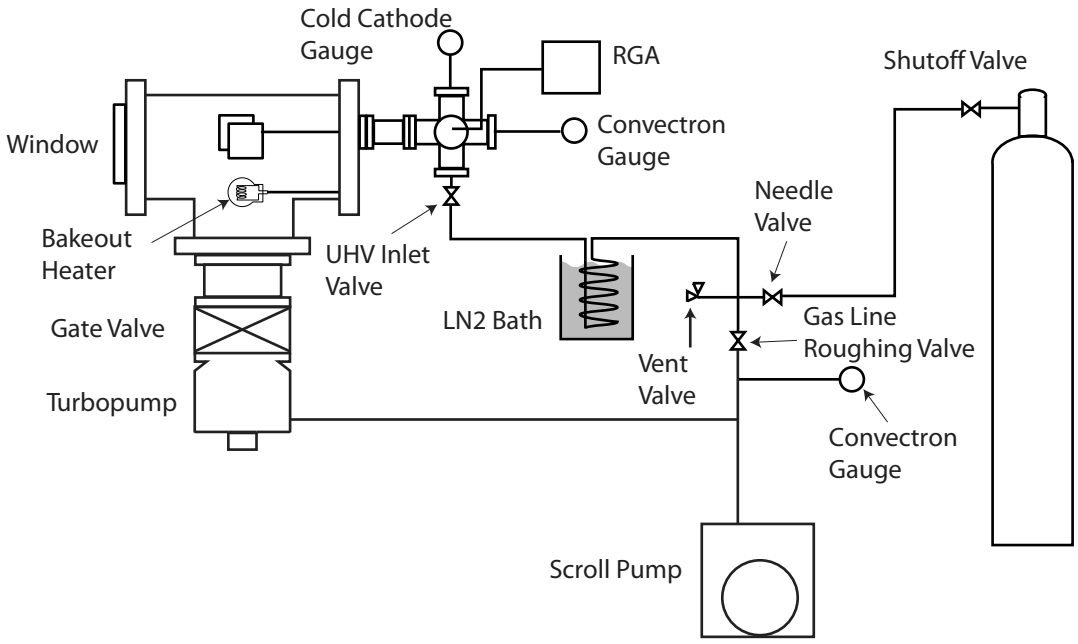

Figure 4.3: Schematic of the vacuum and gas feed systems.

Because we require repeatable surface conditions and gas composition, we constructed a clean vacuum facility that can reach very low pressure (Figure 4.3). The facility is capable of reaching pressures in the high 10^{-10} Torr range and uses no oil, grease, or other liquid in any component exposed to vacuum.

The chamber itself is a 10-inch Conflat "tee" made of stainless steel, and all seals in the system are Conflat copper gasket seals. Inside the chamber is a shelf constructed of an aluminum frame with alumina tubes supporting the electrodes. Flanges on each branch of the tee act as caps on the end of the chamber and as access ports onto which

necessary components can be attached. One of the horizontal caps contains a 2-inch sapphire window that admits laser pulses and gives visual optical access. There is a 6-way, 2.75-inch Conflat cross mounted on the other horizontal cap. On this cross is mounted a Granville-Phillips Convectron vacuum gauge for measuring pressures from atmosphere down to 1 mTorr, an MKS Cold Cathode gauge used for measuring pressures from 1 mTorr down to 10^{-9} Torr, an MKS Vac-Check residual gas analyzer for monitoring gas composition, a gas inlet valve, and the BNC feedthrough for the transmission line. Also mounted on the cap is a feedthrough for the internal heater. The heater is a quartz light bulb that can bring the chamber and electrode surfaces to 200° C. This bakeout procedure removes adsorbed gas from all the surfaces and reduces the background pressure.

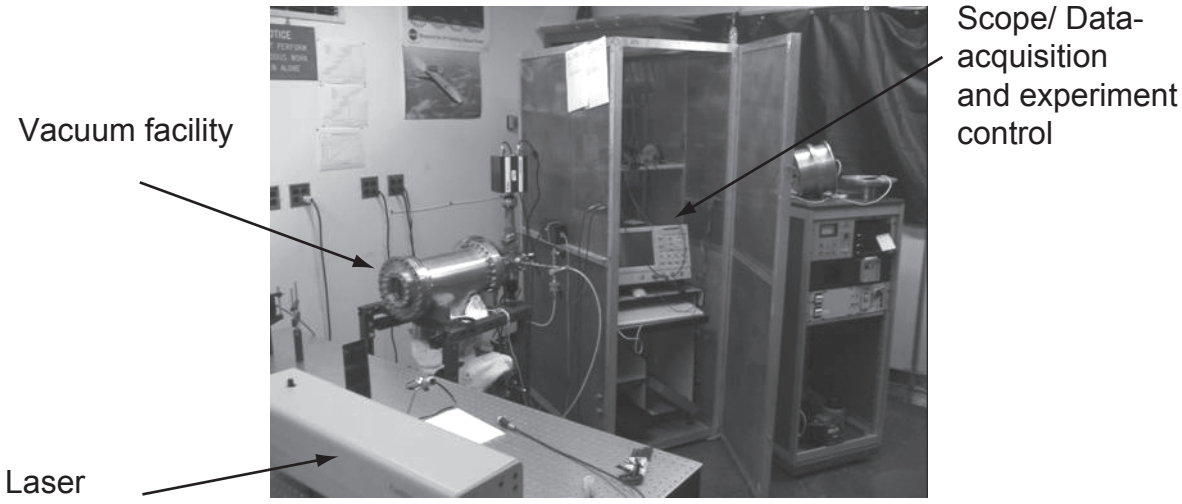

Figure 4.4: The experimental facility.

The third branch of the tee faces down and acts as the pumping port. An oil-free Varian Tri-Scroll mechanical pump provides roughing for the vacuum system. High-vacuum pumping is accomplished with a Leybold Turbovac 150 turbomolecular pump with a rated throughput of 150 L/s. Above the turbopump is an all-metal gate valve that is capable of sealing the chamber while under vacuum but is also used both as a radiation shield to protect the turbopump rotor during bakeout and also as a conductance controller when gas is continuously flowed through the system.

Gas is admitted into the chamber through a gas inlet valve. The gas feed line is connected to the roughing pump and can be evacuated to approximately 25 mTorr. The gas feed line is held under vacuum at all times when not in use, both to reduce the pressure differential across the UHV gas-inlet valve and to minimize the amount of water or other impurities adsorbed in the line's material surfaces. In order to further maintain gas purity, specifically to prevent water vapor from entering the chamber, the gas line is coiled and submersed in a liquid nitrogen bath. Water and other impurities are therefore condensed just before gas passes into the main chamber.

4.1.4 Laser and Optics

The laser used to produce IR laser pulses is a Continuum Surelite Nd:YAG laser operated at its fundamental wavelength of 1064 nm. It is Q-switched and delivers 20 ns pulses with pulse energies up to 800 mJ at the fundamental. For the UV experiment, a Continuum Minilite Nd:YAG laser was used with its second and fourth harmonic generators installed so that it operated at 266 nm. At this wavelength, the laser has a maximum pulse energy of 4 mJ. In each case, the beams intercept the cathode surface at an angle of 20°. The Surelite (IR) laser has a spot size of 1 cm while the Minilite (UV) has a spot size of 8 mm.

For both lasers, pulse energy can be varied by adjusting the delay between the firing of the flashlamp and the Q-switch trigger.

The Surelite laser has an RS-232 interface which allows it to be controlled by the automated data acquisition system. The system can start the flashlamps firing (usually at 10 Hz), open the shutter, adjust the Q-switch delay, and trigger the Q-switch, causing the laser to fire. For the Minilite, flashlamp and Q-switch timing has to be done externally.

Two right-angle prisms direct the beam through the beamsplitter,into the chamber, and onto the cathode target. The beamsplitter is simply a microscope slide off of which the beam is sampled and measured by the photodiode detector.

All optics are mounted on a Newport RS1000 optical table with vibration-isolating dampers.

4.1.5 Automated Data Acquisition System

A large number of data points are required to get statistically significant results. As a result, one experimental run can last for several days of continuous operation. An automated data acquisition system (DAQ) is therefore used to manage the experiment with minimal operator involvement. We have designed such a system using the Labview environment that controls every aspect of the experiment with the exception of the vacuum and gas feed subsystems. The DAQ has the following capabilities:

- Setting the voltage across the electrodes.
- Measuring a steady-state electrode voltage.
- Recording oscilloscope traces of current, photodiode signal, and time-dependent electrode voltage and saving each trace as binary data file.
- Setting the Q-switch delay on the laser and commanding it to fire.

By combining these basic capabilities, we can instruct the system to perform complex series of experimental tasks. For example, given a chamber filled with gas to the desired pressure, the DAQ can slowly increase the electrode voltage until a breakdown occurs; record the breakdown voltage; use that information to calculate an appropriate undervoltage at which to operate and set the electrodes to that voltage; fire the laser with a given intensity; record current, voltage, and photodiode traces; save those traces as data files; determine whether or not undervoltage breakdown occurred and in the event of a breakdown, zero the electrode voltage until the plasma is extinguished, then reset the undervoltage; and repeat the sequence.

4.2 Experimental Procedures

Before we attempt to measure the undervoltage breakdown threshold requirements at a given pressure and gas, we first perform two experiments that give us necessary informa-

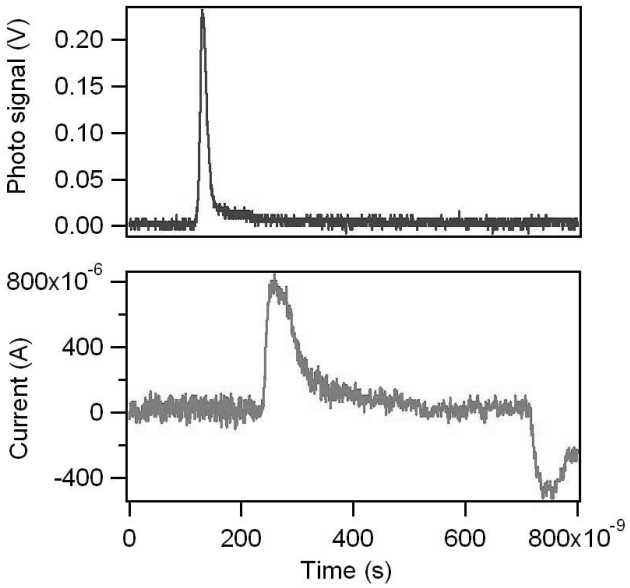

Figure 4.5: Current and photodiode signal during a calibration pulse. For this shot the plate voltage was 300 V and the pressure was 1×10^{-9} Torr. These resulted from IR pulses.

tion about the behavior of the experimental setup: a calibration determining the number of electrons released for a laser signal of a given size, and a measurement of the current between the electrodes as a function of applied voltage.

4.2.1 Pulse Calibration

Although we will measure the current during a breakdown event, the presence of gas and electric fields will induce charge amplification through ionization. Thus, we can never get a direct measurement of the charge released during a laser pulse as long as there is gas in the discharge gap. We therefore perform what we call a *pulse calibration* (or more often, just *calibration*) experiment, in which we measure the amount of charge released during a laser pulse as a function of laser intensity and plate voltage in the absence of gas. In Figure 4.5 we see traces of photodiode signal and current during a calibration pulse. Note the delay due to differences in cable length and the reflection at the end of the current signal. The current signal before the reflection is integrated to give total charge. Example calibration data are plotted in Figure 4.6. The photodiode signal values are divided into

bin ranges which are represented by the photosignal error bars. The error bars on charge represent the error on the mean as calculated from the statistical distribution of all shots which lie in a given photosignal bin.

Note the dependence of released charge on plate voltage. This is a manifestation of space charge effects; similar to the Child-Langmuir law for space-charge limited current, there is a limit to the amount of charge that can be released in a transient pulse into a vacuum gap[1], and that limit is dependent on gap voltage. Using these data, we can calculate a quantum efficiency on the order of 10^{-7}, which is consistent with previous measurements and predictions for copper and 266 nm photons [57].

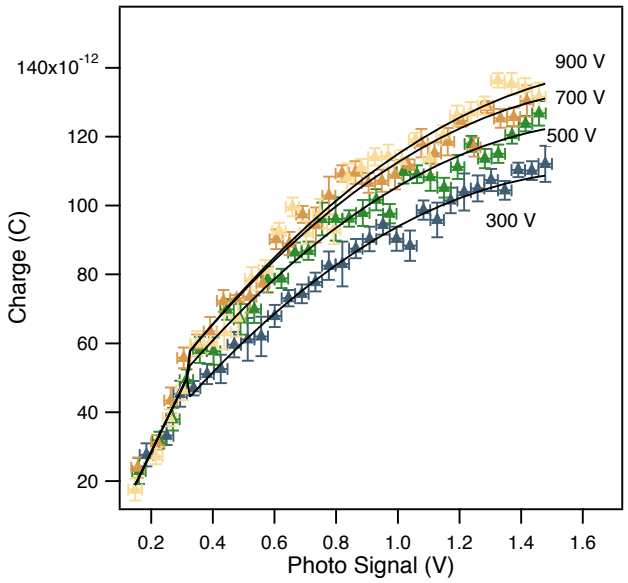

Figure 4.6: Example calibration data plotting charge released as a function of photodiode signal and voltage. These were taken using UV laser pulses. A fit of Equation 4.2 is plotted for 300, 500, 700, and 900 V.

Charge data such as these are fit to a multivariate function of voltage and photodiode

[1]The well-known Child-Langmuir law [54, 55]for space charge limited current applies to steady-state situations in which the distribution of charges acts to screen out the applied electric field, preventing additional current to be drawn from the cathode. In transient cases, there is a limit to the amount of total charge that can be released. In [56], it is argued that, as long as the pulse is short compared with the electron transit time, that limit is given by $Q = \epsilon_0 VA/D$, where V is the gap voltage, A the area of the injected pulse, and D the gap width. Thus, the space charge limit is linearly dependent on voltage, unlike a steady-state case where $J_{crit} \sim V^{3/2}$.

signal of the form:

$$Q = k_0 + (k_1 V + k_2 P) \log (k_3 P), \tag{4.2}$$

where V is the voltage, P the photodiode signal, and $k_0 - k_3$ are fit coefficients. This functional form was empirically chosen to appropriately fit the data and does not necessarily represent any dependence predicted from physical arguments (though the linear relationship between released charge and electrode voltage does agree with the predictions presented in [56].)

When we later introduce the gas, we still have the measurement of laser intensity that allows us to calculate the charge released based on the *a priori* calibration fit. Using conventional propagation of error techniques [58], we can calculate that the uncertainty in the charge measurement is:

$$\begin{aligned} \Delta Q^2 &= \Delta k_0^2 + \frac{\Delta k_3^2}{k_3^2}(k_1 V + k_2 P)^2 + (V^2 \Delta k_1^2 + k_1^2 \Delta V^2 + P^2 \Delta k_2^2)[\log (k_3 P)]^2 \\ &\quad + \frac{\Delta P^2}{P^2}[k_1 V + k_2 P(1 + \log (k_3 P))]^2. \end{aligned} \tag{4.3}$$

However, there is a significant physical difference between charge introduced into a vacuum and charge introduced into a gas-filled gap. The presence of neutral gas atoms slows the electrons through collisions and extends the transit time of the burst. In a vacuum, the front of the pulse may reach the anode while additional electrons are being introduced. That part of the burst thus does not contribute to space charge limitations on the current pulses. In Appendix B, we describe a numerical conversion method, based on the theoretical framework we describe in Chapter 3, that we use to calculate the actual charge released given a calculated vacuum pulse.

Using this setup, we are able to produce and measure pulses in the range of 10^{-11} - 10^{-9} C.

4.2.2 Current-Voltage Characteristics

We also need to measure the breakdown properties of the gap: not only the breakdown voltage, but also the voltage below which plasma cannot be sustained. It is between these two values that undervoltage breakdown might be achieved, so we take current-voltage characteristics before beginning the undervoltage breakdown experiment.

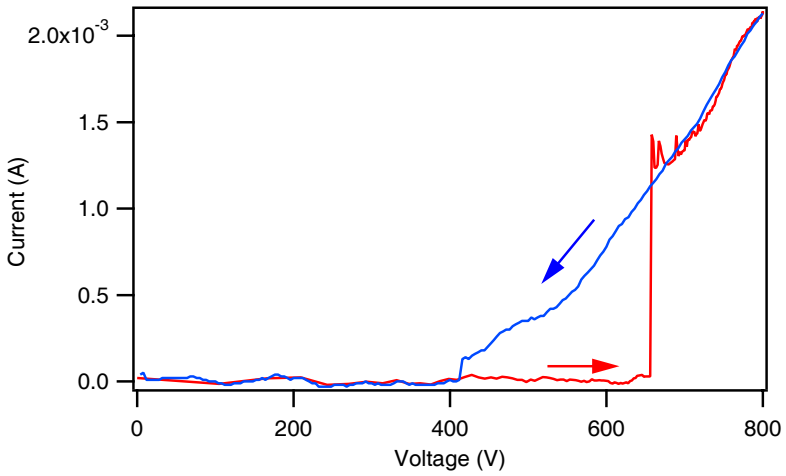

Figure 4.7: An example current-voltage characteristic for the undervoltage breakdown experiment.

Figure 4.7 contains a current-voltage characteristic, displaying the plasma current as the voltage is increased to a maximum, then decreased. The red part of the trace represents the current as the voltage is increased. It stays near zero until the breakdown voltage, in this case about 650 V, is reached. At breakdown, the current discontinuously jumps to finite value of around 1 mA, then increases approximately linearly with voltage. The blue section of the trace is the current as the voltage is decreased. We can see that a hysteresis occurs; plasma can be sustained below the breakdown voltage, so the current does not fall to zero as the voltage is brought below 650 V. Measurable current is conducted at a voltage as low as about 415 V. In this case, therefore, undervoltage breakdown might be achieved between 415 V and 650 V.

Once the calibration is established, gas is introduced into the chamber to the desired pressure and the breakdown voltage of the gap is measured. The plates are set to the de-

sired undervoltage, then the laser fires shots of varying intensity. Photodiode and voltage traces are saved after each shot. If the shot caused a breakdown, the voltage is turned off, plasma is extinguished, the plates are set back to the correct voltage, and the process is repeated. About 400 shots are necessary at each voltage to get significant statistics to establish probabilistic trends.

4.2.3 Sequence of Events in an Undervoltage Breakdown Experiment

The primary purpose of the undervoltage breakdown experiment is to generate threshold curves, measurements of the number of electrons required to induce breakdown as a function of initial conditions. In order to produce those results, the following experimental procedure is carried out:

1. Evacuate the chamber to ultra-high vacuum levels (10^{-9} Torr and below) and bake the facility and electrodes to desorb gases from all surfaces.
2. Perform a pulse calibration measurement.
3. Introduce high-purity gas to the desired pressure using the gas feed system.
4. Perform a current-voltage characteristic measurement.
5. Determine the voltages appropriate for undervoltage breakdown measurements.
6. Initiate an automated threshold measurement: setting the electrodes to the appropriate voltage; firing laser pulses of varying size; downloading the resulting current, voltage, and photosignal traces; extinguishing the plasma if needed and resetting the voltage; and repeating until the required amount of data has been recorded.

4.3 Data Analysis

Figure 4.8 contains examples of the raw data files used to calculate the threshold curves. For each laser firing, one set of photodiode and voltage traces is recorded and analyzed.

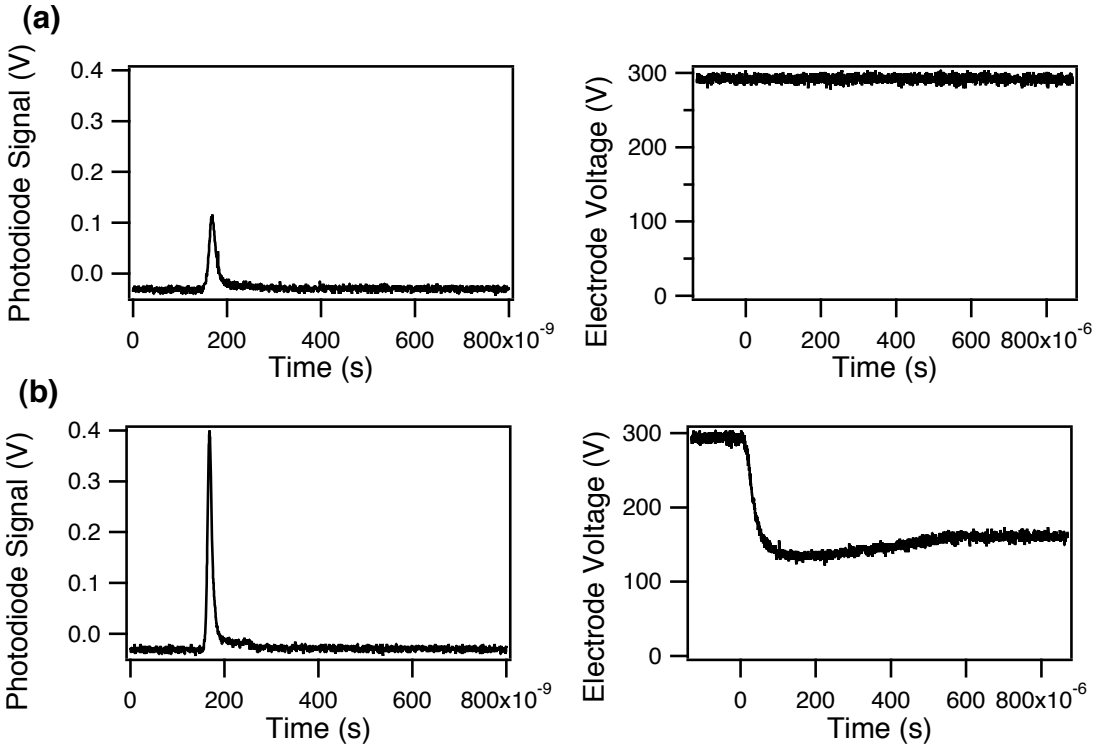

Figure 4.8: Two pairs of oscilloscope traces recorded in the undervoltage breakdown experiment. These were taken with UV laser pulses, argon at 3 Torr, and an initial electrode voltage of 295 V.

The timescales on the two traces are different; a laser pulse would appear as instantaneous at $t = 0$ on the voltage trace. The traces in Figure 4.8 (a) represent a relatively weak laser pulse that does not result in a breakdown; no change in voltage is observed. In (b), however, a more intense pulse does result in breakdown. This is manifested in a drop in voltage across the electrodes. Such a voltage drop always corresponds to formation of visible plasma between the electrodes (Figure 4.9.)

For each photodiode trace, the small DC offset (resulting from an applied bias voltage on the photodiode) is subtracted and the maximum value is recorded. The calibration fit (Equations 4.2 and 4.3) is then used to calculate the initial charge released based on this value and the applied voltage. The corresponding voltage trace is then analyzed to determine if a breakdown occurred: if the minimum voltage value observed is less than 90% of the pre-pulse value, that trace is considered to represent a breakdown. A weighted

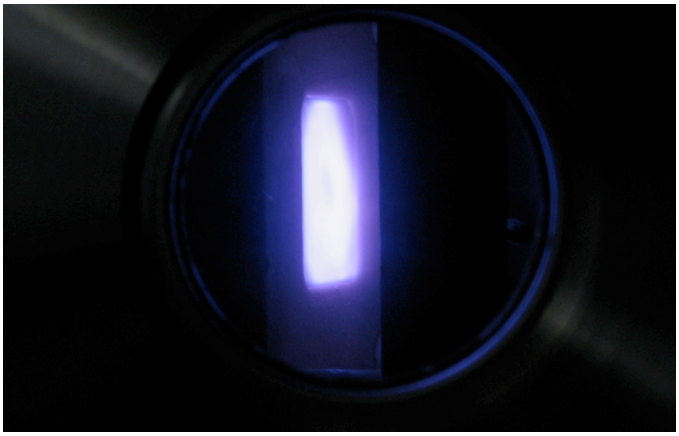

Figure 4.9: Visible plasma between the electrodes as resulting from a laser pulse.

histogram is then calculated which divides the entire range of charge values into bins and specifies the fraction of shots within each bin that resulted in a breakdown. Such a histogram is plotted in Figure 4.10. Charge error bars are calculated from the calibration fit parameters and Equation 4.3 using the photosignal bin width as the uncertainty in the photo error and neglected uncertainty in the initial voltage. Error bars on the probability are calculated based on binomial error, $\sigma = \sqrt{p(1-p)/n}$ where p is the fraction of times a pulse in that charge bin caused a breakdown and n is the number of pulses in the bin.

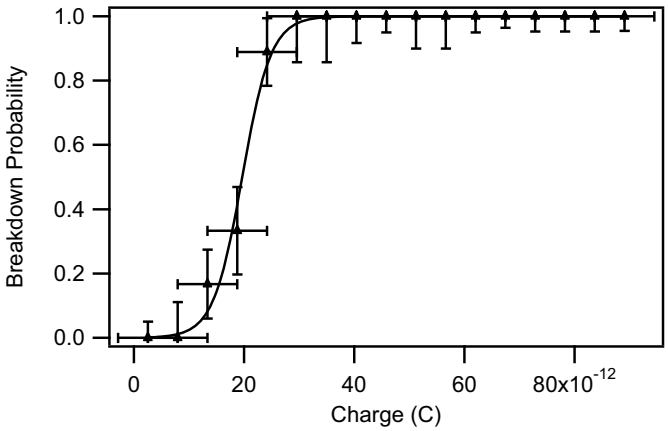

Figure 4.10: Probability of breakdown as a function of charge in the initial pulse for argon at 3 Torr and 295 V. UV laser pulses were used for this experiment. A least-squares fit of Equation 4.4 is overlayed.

What we see is that at very low values of initial charge, breakdown is very unlikely,

at very high values, breakdown is very likely, and some intermediate regime exists. The quantity we are seeking, the number of electrons (or the total charge) in a pulse required to achieve undervoltage breakdown, can be gleaned from graphs such as this. Charge error bars are calculated from the calibration experiment and represent the root mean square deviation of charges for a given photosignal bin as calculated from Equation 4.3.

Data such as these can be fit to sigmoid functions of the form:

$$y(x) = y_0 + \frac{y_{max}}{1 + \exp\left(\frac{x_{1/2} - x}{\nu}\right)} \tag{4.4}$$

An example is plotted in Figure 4.11. The fit parameters are y_0, which represents the limit as $x \to -\infty$; y_{max}, the limit as $x \to \infty$; ν, which describes the steepness of the transition region of the curve; and $x_{1/2}$, the x value where the curve reaches $(y_{max} - y_0)/2$. When fitting this function, if we fix y_{max} at unity and y_0 at zero, $x_{1/2}$ represents the charge value at which the breakdown probability is 50%. We will define this value as the threshold charge and plot it for varied experimental conditions.

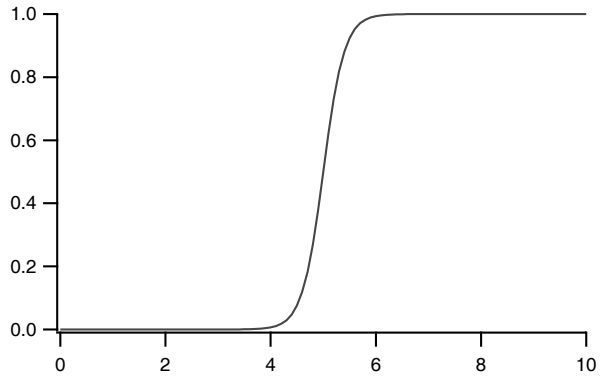

Figure 4.11: Sigmoid function used to fit the breakdown probability data.

4.4 Experimental Results

4.4.1 Results of the UV Experiments

Oscilloscope traces such as those in Figure 4.8 are analyzed, in combination with pulse calibration data, to generate weighted histograms such as in Figure 4.10. Each of those histograms represents about 400 data files, each corresponding to a laser shot of varying intensity, but at the same conditions of voltage and pressure. Each histogram is then fit to a sigmoid function to determine the breakdown threshold for that particular set of experimental conditions. The threshold data we present in Figure 4.12 thus represent the distilled results gleaned from thousands of individual data sets.

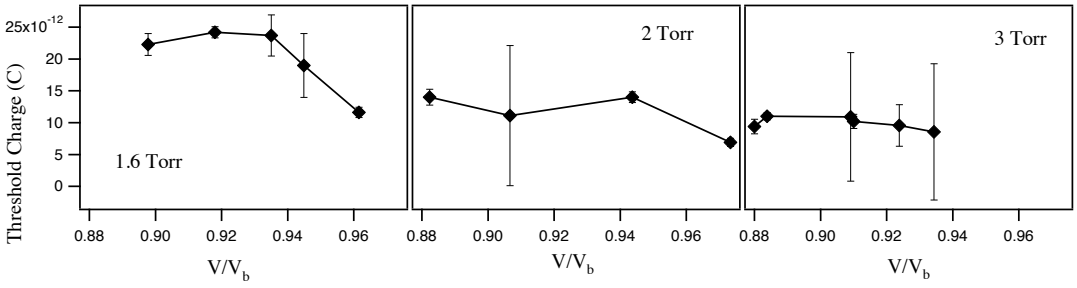

Figure 4.12: Threshold charge as measured by the undervoltage breakdown experiment in argon at 1.6 Torr, 2 Torr, and 3 Torr.

Figure 4.12 plots the experimentally measured threshold charge as a function of V/V_b (plate voltage normalized to the breakdown voltage at each pressure) for argon at pressures of 1.6 Torr, 2 Torr, and 3 Torr. The experiment was also carried out at pressures of 1.5 Torr, 1.4 Torr, and 1 Torr, but no breakdowns occurred at these lower pressures.

The magnitude of the threshold charge is 10^{-11} C, or 10^8 electrons. The trend of decreasing threshold with increasing pressure is visible; the threshold is clearly lower at 2 and 3 Torr than at 1.6 Torr. An expected trend of decreasing threshold with increasing voltage is less clear, but the data are not totally inconsistent with such behavior.

The timescale of the breakdown, observable in Figure 4.8 (b), was always on the order of 10-100 μs for the UV experiments.

Analysis and further discussion of these results will be presented in Chapter 5.

4.4.2 Results of the IR Experiments

For the IR experiments, pressures of 1 Torr, 500 mTorr, and 300 mTorr were used — lower pressures than those in the UV experiments.

One important phenomenological distinction between the UV and IR experiments is that a characteristically different type of breakdown was observed in the IR experiments. In the example shown in Figure 4.13, the voltage was initially set to 550 V, below the breakdown voltage of 590 V measured at 300 mTorr of argon. These traces were triggered off the photodiode signal, which occurs at time $t = 0$ and would appear instantaneous on this scale. In the first trace, the voltage drops relatively slowly to a moderate voltage around 300 V before establishing a steady-state glow discharge. All breakdowns observed in the UV experiments displayed this behavior. The process takes about 50 μs and the maximum current attained is 2.5 mA. However, in the second trace, the breakdown occurs much faster and to a much greater degree. The voltage drops to 0 V in less than 1 μs. Breakdowns of this type were only observed in the IR experiments.

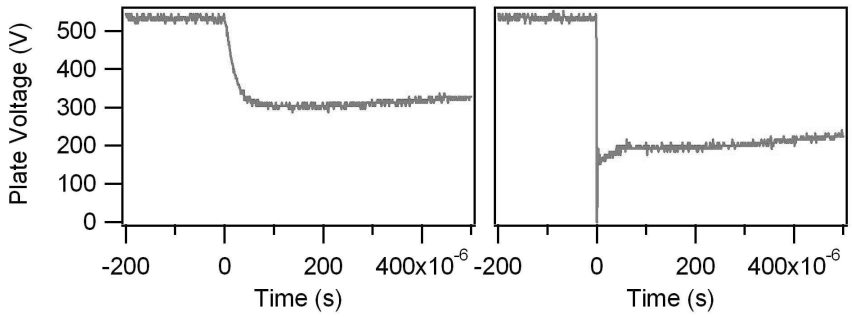

Figure 4.13: Voltage traces of two different types of breakdowns.

We will call discharges such as those in the first trace *slow* breakdowns and discharges like those in the second trace *fast* breakdowns. Based on the timescale of the breakdown phenomenon, and the minimum voltage reached, it is reasonable to conclude that they represent examples of Townsend breakdown to a glow discharge.

Plots of the critical charge used to achieve slow breakdown for these pressures are

presented in Figure 4.14.

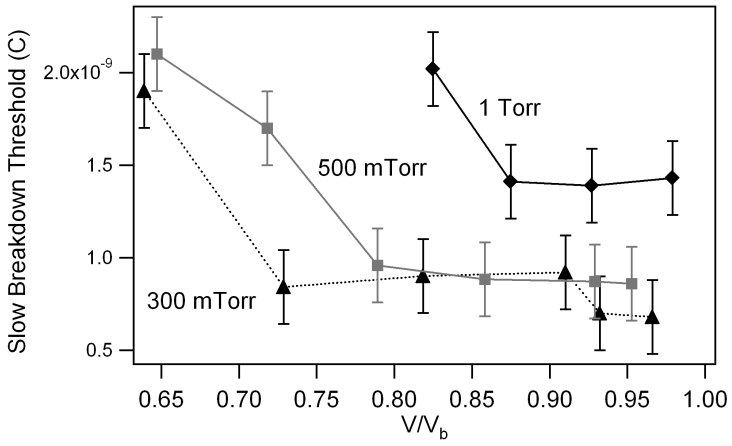

Figure 4.14: Slow undervoltage breakdown threshold versus fraction of breakdown voltage for argon.

As the voltage is brought closer to the breakdown voltage, the charge required for breakdown decreases – this is as expected. However, in this case, increasing the pressure seems to increase the required charge; a trend that stands in opposition to the theoretical predictions. In addition, the maximum value of $\bar{p}$ seen in these experiments (corresponding to 1 Torr at 500 V) is approximately 0.9, well below the critical value predicted by the theory.

The mechanism and discharge characteristic of the phenomenon represented by the second trace in Figure 4.13 is less clear. An arc discharge requires high current to provide ion flux to the cathode sufficient for thermionic emission. The circuit cannot sustain that, so it is not surprising that the voltage quickly begins to return to the more moderate glow voltage, which leaves the question of the exact nature of this discharge somewhat ambiguous. This could be an indication of streamer breakdown, although no discharge at an undervoltage or such a low pressure has been reported in the literature. Regardless, it is clear that in this case we have achieved a much faster breakdown to a temporarily higher conductivity than in the slow case.

In Figure 4.15, we see an example threshold plot for the fast breakdown. It demonstrates that the fast breakdowns are much less likely than the slow ones, only occurring with very large pulses. The plot shown here is of the data set that had the most instances

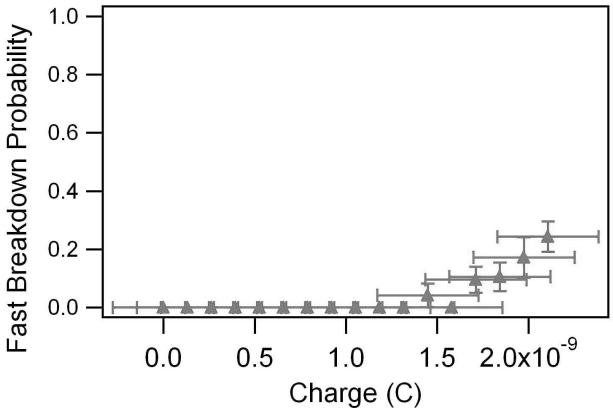

Figure 4.15: Probability of fast breakdown as a function of initial charge for 500 mTorr of argon at 356 V.

of fast breakdown of any taken. For most, fast breakdowns either did not occur or occurred in such small numbers as not to be statistically significant.

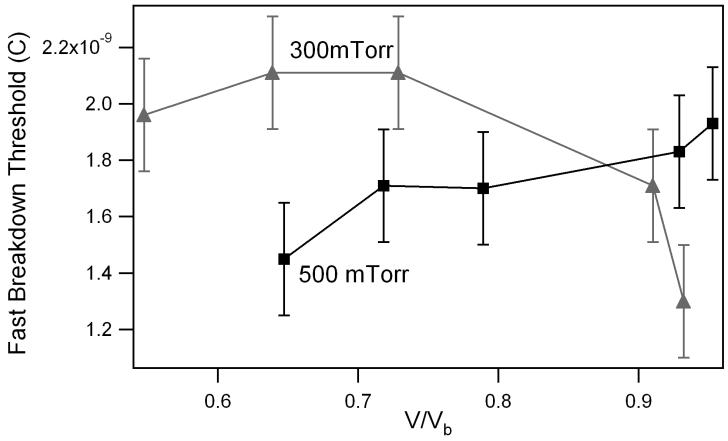

Figure 4.16: Fast undervoltage breakdown threshold versus fraction of breakdown voltage for argon. No fast breakdowns were observed at 1 Torr.

Making quantitative statements about the threshold conditions for fast breakdowns is more difficult because of the relative rarity of that phenomenon. However, if we seek only an order-of-magnitude estimate of the charge required to produce breakdown, examination of those data is worthwhile. Our previously defined threshold condition of 50% breakdown probability will not work because fast breakdowns never appeared with that probability. Instead, we plot in Figure 4.16 the lowest charge at which fast breakdown was observed

as a function of undervoltage.

These data are less well-behaved than the slow breakdown data, but it is clear that more charge is required to produce a fast breakdown than a slow one in all cases. Presumably, if our experimental setup could supply more charge, more fast breakdowns would occur, though as we will discuss later, the phenomenon is likely also linked to desorption of gas from the cathode surface during a laser pulse. However, we can see that at the lower pressures, roughly 2×10^{-9} C, or 1×10^{10} electrons seem to cause fast breakdown.

Chapter 5

Analysis and Discussion

The IR and UV experiments displayed characteristically different behavior in terms of the magnitude of the charge necessary, the pressure dependence of the breakdown threshold, the pressures at which breakdown was achievable, and the occurrence of the "fast" breakdown mechanism. This is likely the result of the discrepancy between the amount of energy in the laser pulses of the respective experiments, and especially the degree to which the cathode surfaces were heated.

We will therefore separate the analysis of these two series of experiments. We begin by comparing the UV results with theoretical predictions from the undervoltage breakdown model and discussing the useful insights such a comparison produces. We then continue with a discussion of the IR results and incorporate an explanation for the interesting phenomenological disparity between these data sets.

5.1 Discussion of the Results of the UV Experiments

UV laser pulses only produced breakdowns such as that represented in Figure 5.1: transitions occurring over a period of around 100 μs that reach a moderate voltage. These breakdowns are identical to the "slow" breakdowns observed in the IR experiments and, as stated, are consistent with the picture of a Townsend-like breakdown to glow discharge

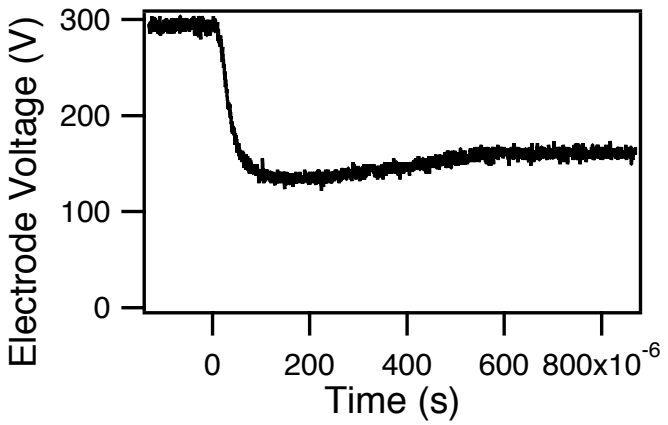

Figure 5.1: Voltage drop during a typical UV-induced breakdown. Note the 100 μs breakdown timescale.

that transpires over several ion avalanche generations. This is the phenomenon we are investigating, and we therefore expect comparison between these data and our theoretical predictions to be fruitful.

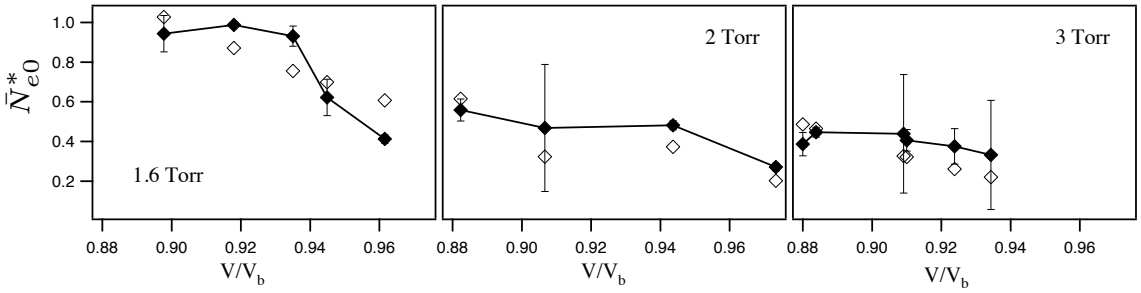

Figure 5.2: $\bar{N}^*_{e0}$ as measured (solid) and calculated for $\gamma = .1$ (open).

In Figure 5.2, we plot $\bar{N}^*_{e0}$ as calculated from the experimentally measured threshold charge values displayed in Figure 4.12. For each data point, we also plot the theoretically calculated value using published values for the Townsend ionization coefficients from [43] for argon[1] and assuming $\gamma = 0.1$. The true secondary emission coefficient, and its dependencies on electric field and pressure, are highly dependent on surface conditions [43] and are not well known. That value of γ was chosen because it generates good

[1]See Appendix C for a more detailed explanation of how we arrived at appropriate α values for this range of E/p.

agreement between predictions and data, but it happens to fall within an expected range for these experimental conditions.

The dimensionless parameter $\bar{N}_{e0}^{*}$ represents the ratio of the critical injected charge to the initial charge on an electrode resulting from the applied voltage, and ranges within values on the order of 10^{-1} for these experimental conditions. In order to enhance ionization through a distortion of the applied electric field, we must provide sufficient charge to compete with that field. Ionization will amplify the injected charge, but at low gain, the initial charge must still be a significant fraction of the applied charge. This is the fundamental difference between the phenomenon we are investigating, undervoltage breakdown through the Townsend mechanism at low gain, and breakdown in higher-gain devices, in which a single electron can start an avalanche that forms a streamer.

The trend of decreasing $\bar{N}_{e0}^{*}$ with increasing pressure ($\bar{p}$) is a demonstration of the importance of the α-process to undervoltage breakdown. At higher pressure, ionization is more field-limited than pressure-limited, and the system is more sensitive to increases in electric field such as those caused by the space charge distortion.

The relevance of the α process to undervoltage breakdown also explains the theoretically predicted dependence of critical pulse size on the secondary emission coefficient. Increasing γ increases $\bar{N}_{e0}^{*}$ because, at constant μ_0, higher γ implies lower σ. Since undervoltage Townsend breakdown is achieved through manipulation of gas amplification and not secondary emission, the phenomenon is more difficult to achieve when the amplification factor is reduced.

The weak dependence on ion mobility (Figure 3.7) suggests that breakdown is determined during the first electron avalanche.

From the Townsend coefficients for argon, we can deduce that $\bar{p} = 2$, for the voltage range used in these experiments, corresponds to pressures ranging from 1.3 Torr to 1.6 Torr at these voltages. The theoretical predictions of [59] suggest that these values represent approximate critical pressures below which undervoltage breakdown should not be possible, and indeed, no breakdowns were observed below 1.6 Torr.

5.2 Discussion of the Results of the IR Experiments

Unlike the results of the UV experiments, which were mostly consistent with theoretical predictions, the data from the IR experiments displayed three unexpected behaviors: a directly proportional relationship between gas pressure and critical charge, breakdowns below the critical $\bar{p}$, and "fast" breakdowns to temporarily high-conductivity discharges.

The fundamental difference between the two experiments is the manner in which the laser pulse interacts with the cathode surface. The UV photons photoelectrically interact with electrons bound to the copper surface, but the pulses are too weak to significantly heat the surface or affect it in any other way. The IR photons do not release photoelectrons from the tungsten cathode, but heat the surface significantly. The electron emission mechanism is not entirely clear; thermal modeling of surface heating during a laser pulse (Appendix A) suggests that it is possible for a tungsten surface to be heated such that significant thermionic emission occurs without melting or evaporation of the surface. However, it is also the case that gas desorbed from the surface plays a significant role.

The effects of gas desorption were evident while the experiment was taking place. During a calibration procedure, when the chamber was evacuated to pressures in the low 10^{-9} Torr range, we observed pressure spikes that brought the background to as high as 10^{-7} Torr temporarily before it quickly came back down. These pressure spikes corresponded to the more intense laser pulses. No such pressure spikes were observed during calibration with UV pulses. To measure the composition of the desorbed gas, we set up an experiment in which we evacuated the facility, closed the gate valve to seal the chamber, then set the (IR) laser firing at a repetition rate of 10 Hz at maximum pulse energy. The composition of the gas in the chamber was recorded with the residual gas analyzer. The results are presented in Figure 5.3.

The background gas pressure, which starts in this experiment around 2×10^{-9} Torr, increases when the laser is turned on up to approximately 2×10^{-8} Torr. Hydrogen dominates the gas background — this is not surprising since the turbopump is known to be

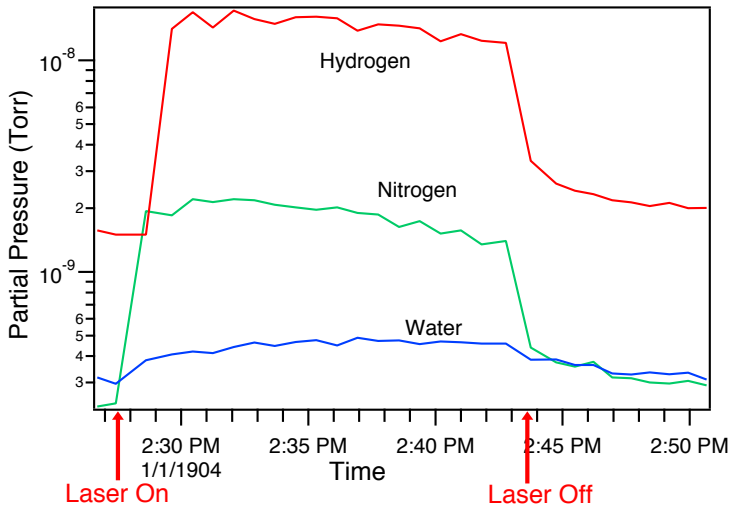

Figure 5.3: Partial pressures of gas released during the desorption experiment.

less efficient at pumping low-molecular-weight gases and we expect more hydrogen to be adsorbed on the surfaces of the vessel and electrodes. Water is also released, as is nitrogen, which increases its partial pressure relative to the other two gases. Regardless, when the laser is turned off, the pressure falls again, indicating that the released gas has been re-adsorbed onto various surfaces.

It is not our intention to completely explain the effects of the release of heated, possibly ionized gas of complex composition into our discharge gap and the effect this phenomenon might have on undervoltage breakdown. However, it is clear that significant gas is released when the cathode is heated by IR laser pulses. It is not unreasonable to speculate that this process is a major part of the explanation of each of the three major discrepancies between the theoretical predictions and the IR experimental results.

It seems clear that introducing additional gas could increase the local partial pressure above that which would corresponds to the critical parameter. In addition, the ejected material would change the local gas composition; both nitrogen and water have higher values of the Townsend B coefficient than argon, though hydrogen is lower. These could explain the observation that discharges occur below the critical $\bar{p}$.

Also, we would expect the amount of gas desorbed from the surface during a laser

pulse to be inversely proportional to the gaseous background pressure. This could explain the unexpected relationship between gas pressure and critical laser intensity that manifests itself as a direct proportionality between pressure and critical charge.

As for the fast breakdowns, the timing of the phenomenon suggests streamer-like behavior, a phenomenon generally known to occur in high-pd discharges (see Chapter 2. The region of high-density gas released during the laser pulse could be somehow involved in enhancing the ionization avalanche to the point where streamer formation occurs. In addition, it should be noted that the magnitude of charge released during an IR pulse is much higher than that released during a UV pulse. It may be this fact alone that explains the fast breakdowns.

5.3 Summary

Examination of the results of the undervoltage breakdown experiments, coupled with our theoretical predictions, allowed us to arrive at the following insights into undervoltage breakdown:

- At low gain and with injected pulses of comparable or lesser charge than that initially applied to the electrodes, undervoltage breakdown proceeds through a Townsend-like mechanism — through the successive growth of multiple avalanche generations. The breakdown timescale observed in the UV experiments and in the "slow" breakdowns of the IR experiments is consistent with this picture.

- Undervoltage breakdown becomes easier as the sensitivity of the α process to electric field distortion is increased, such as through increases in pressure. The theoretically predicted trend of an inverse relationship between critical charge and the dimensionless parameter $\bar{p}$, observed in the UV experiments, is a demonstration of this effect.

- Undervoltage breakdown should be impossible below $\bar{p} \approx 2$; below this value elec-

tric field suppression has a larger negative effect on electron-impact ionization than electric field enhancement has a positive one. The experimental data are partially consistent with this prediction, no discharges were observed in the UV experiments at a pressure corresponding to that less than $\bar{p} = 2.15$. Discharges occurred in the IR experiments at lower $\bar{p}$ values, but gas desorption would have locally increased the value of that parameter by increasing gas density and altering gas composition.

- To achieve breakdown at low gain, the space charge distortion must result from the magnitude of the injected pulse, so the injected charge must be significant when compared with the charge on the electrodes. The magnitude of the threshold charges required in the UV experiments bears this out.

- High-power, infrared laser pulses have somewhat unpredictable effects on undervoltage breakdown, due to the desorbed gas or other material they release through surface heating. These bursts of gas can impact the breakdown process, changing gas composition or density and inducing breakdown when it otherwise would not have occurred.

- A fast, streamer-like breakdown mechanism, transpiring on a timescale less than one electron avalanche transit, can occur in a low-gain, undervoltaged discharge gap. Some combination of a large magnitude of injected charge (in comparison to the charge on the plate) and pressure burst due to gas desorption is required to achieve this phenomenon.

Chapter 6

Discharge Initiation Requirements for GFPPTs

While the primary goals of this work were focused on investigating undervoltage breakdown from a fundamental point of view, the work was originally motivated by a desire to understand and improve discharge initiation in pulsed plasma thrusters. Now that we have arrived at a number of insights into the basic mechanisms that govern the phenomenon, it is worthwhile to try to apply some of those insights to problems with actual propulsion hardware. To that end, we present in this chapter a discussion of what is actually required of a GFPPT discharge initiation system, and how our knowledge of undervoltage breakdown can be used to meet those requirements.

6.1 The Pulsed Plasma Thruster

The Pulsed Plasma Thruster (PPT) [60] is one of a class of *electric spacecraft propulsion* devices [16, 61] that use electric power to accelerate propellant. Electric thrusters are characterized by high exhaust velocities (up to 100 km/s) at very low thrust (mN-N) compared with conventional chemical rockets. The low thrust renders electric thrusters unsuitable for launch or other use in the atmosphere, but the high exhaust velocity signifi-

cantly reduces the mass of propellant required for a given mission.

Electric thrusters are often classified into three categories according to the processes they use to accelerate their propellant [61]: *electrothermal* thrusters use electric power to heat gas which is then expanded through a nozzle; *electrostatic* thrusters accelerate charged particles with electric fields; and *electromagnetic* devices use combinations of electric and magnetic fields to impart momentum to ionized gas.

The PPT [60] is an unsteady electromagnetic device, accelerating pulses of ionized gas by means of a magnetic body force. It can be used for either primary propulsion or attitude control of spacecraft. Because of its pulsed nature, the average thrust can be easily throttled by varying the pulse frequency, energy per pulse, or quantity of gas accelerated per pulse. In addition, each pulse represents a very small impulse bit ($<$ 100μNs) so PPTs can be used for very fine positioning.

There are two well-known varieties of PPT: ablative and gas-fed. Ablative PPTs [62,63] use solid propellant (usually polytetrafluoroethene — PTFE, also known as Teflon) and require neither tankage nor valves. They are thus extremely simple to integrate into a spacecraft system and have been among the most common electric thrusters to fly in space.

Gas-fed PPTs [17,64–66] use a more conventional propellant delivery system to inject and accelerate pulses of gas. The devices offer much higher performance than ablative PPTs in terms of thrust efficiency ($\eta_{thrust} \approx 10\%$) and specific impulse (5000 s) [17]. While they don't offer the same system simplicity, they are extremely versatile, and can accelerate virtually any gaseous propellant. However, they have never seen space operation largely because of lifetime and performance issues which have only slowly been addressed. GFPPTs require propellant feed systems that must store gas at high pressure and reliable fast valves that can survive excesses of 10^9 firings without leaking. Such technology was not available when the thrusters were first researched in the early 1960's and the GFPPT was not considered a viable thruster candidate until improved fast valves and high-speed solid-state switches were implemented in the early 1990's [17]. Since then,

there has been renewed interest in GFPPTs, but the thrusters still present lifetime issues.

6.2 How a GFPPT works

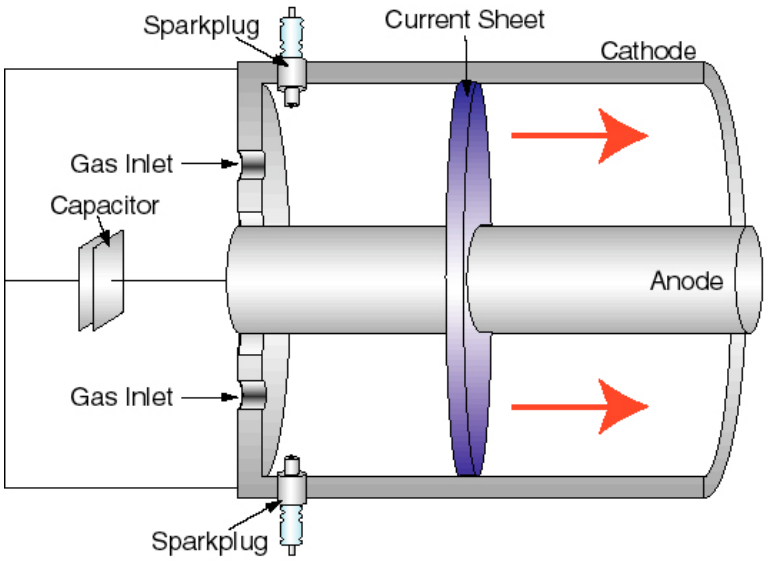

Figure 6.1: Diagram of a coaxial pulsed plasma thruster.

Figure 6.1 is a diagram of the major components of a GFPPT. These thrusters exist in many configurations, including parallel-plate [67,68] and cylindrical "z-pinch" [69–73], but the one shown is a coaxial device [74,75]. The thruster consists of two electrodes across which a large capacitor or bank of capacitors is placed. The breech of the thruster contains inlet holes through which fast valves can inject small puffs of gas, and a discharge initiation system (traditionally spark plugs or other high-voltage electrodes).

The first event that occurs in the lifetime of each pulse is the charging of the capacitor. Since gas acceleration will require much more power than is continuously available from any spacecraft power system, capacitors are used to deliver high instantaneous power. A voltage (usually a few hundred volts) is placed across the capacitor and thruster electrodes until the capacitor is fully charged. Following that, the valves inject a small amount of gas through the inlet holes, and the gas is then allowed to fill the inter-electrode gap.

The next step is the initiation phase. The sparkplugs (or other initiation system) fire at the precisely determined appropriate time, releasing charge carriers into the gap. This causes the gas to break down, forming a conductive path between the electrodes. Once current is allowed to flow, the capacitors release all of their stored energy into the gas in a very short time ($<$1 μs, more on this later). The result of this is that the discharge intensifies and narrows to form a well-defined sheet of current.

Once the current sheet is formed, the acceleration process begins. The current, which ideally is radial, induces an azimuthal magnetic field. This field in turn interacts with the current and exerts an axial $\mathbf{j} \times \mathbf{B}$ force. This is the acceleration force which causes the current sheet to move down the barrel of the thruster. As the sheet propagates, it envelops neutral gas and accelerates it down the channel.

Finally, as the sheet nears the end of the channel, it is ejected, pushing the entrained mass of neutral gas along with it. The system is reset and prepared for the next pulse. The sequence is repeated on a duty cycle that depends on the mission requirements.

6.3 Discharge Initiation in GFPPTs

This work focuses on one part of the GFPPT firing cycle: the discharge initiation.

Historically, GFPPTs and similar devices used as laboratory pulsed plasma accelerators employed discharge initiation systems based on one of three fundamental mechanisms.[1] The first, which we call *Paschen Initiation*, involved setting the electrodes to the desired operating voltage, then injecting a puff of gas. When the pressure between the electrodes became high enough that the electrode voltage was sufficient for breakdown, plasma formed. Used in the early days of pulsed plasma accelerator research in the 1960's, mostly at labs at General Dynamics [76–86] and General Electric [87, 88], this technique fell out of favor, especially for thruster applications, because of unreliability and inflexibility — changing the mass bit or operating voltage changes the timing of break-

[1] A review of the history of the development of GFPPTs and pulsed plasma accelerators, with details about discharge initiation and performance, can be found in [64].

down. This seriously hinders performance as breaking down too early results in current sheet acceleration before enough mass has accumulated, while breaking down too late allows gas to leak out the end of the thruster without being accelerated [89].

Accelerators using the second mechanism, *overvoltage breakdown* [67, 72, 75, 90–92], injected the gas first before putting any voltage across the electrodes, then quickly switched on a voltage that greatly exceeded that required to break the gas down. Such a technique solves the problems of timing and repeatability but adds the complexity of a fast, high-voltage switch. Including such a switch, usually an Ignitron or gas-discharge switch, means including additional mass, parasitic inductance, and (perhaps most importantly) a component proven to have limited lifetime. Furthermore, overvoltage breakdown requires high voltages, often tens of kV, which in turn requires heavy high-voltage capacitors. These issues are less relevant in a laboratory setting but become critical for thruster applications.

Undervoltage breakdown is the final mechanism that pulsed plasma accelerators, specifically GFPPTs, use to initiate their discharges. The electrodes are set to an undervoltage corresponding to the conditions that occur when gas is introduced. Propellant is injected, then a separate discharge initiation circuit fires at the appropriate time, supplying a pulse of electrons from secondary electrodes such as needles [93–95], or sparkplugs [96, 97]. The electron pulse then triggers breakdown. This mechanism has several advantages: breakdown timing can be accurately controlled, the isolation of the initiation circuit from the rest of the thruster's circuitry allows for minimal parasitic inductance as well as more manageable charging voltages, and the discharge initiation circuitry is simpler and perhaps more rugged than the high-voltage switching technology.

Undervoltage breakdown as a mechanism for PPT discharge initiation is not without its drawbacks, however. The electron injectors tend to create plasma in their local vicinity, which can result in nonuniform current sheets. Figure 6.2 is a high-speed image taken of a GFPPT current sheet. This particular GFPPT, SRL-PT4 operated at Princeton [97], uses four sparkplugs as discharge initiation mechanism. It is clear from the photograph that the current sheet forms preferentially near the sparkplugs. The result is a nonuniform current

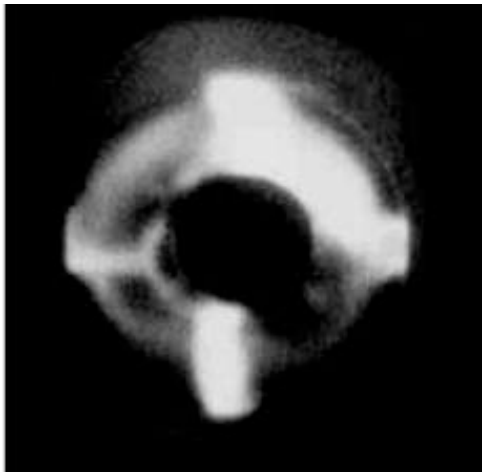

Figure 6.2: High speed photograph of a current sheet in a GFPPT ([97]).

sheet that is more permeable and less efficient than a well-formed one would be [97]. In this case, the problem is exacerbated by non-simultaneity of the spark discharges.

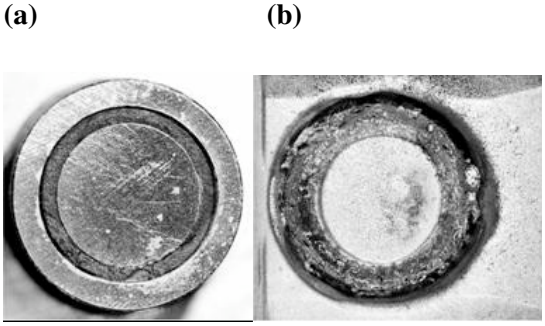

Figure 6.3: A sparkplug used for initiation of a GFPPT after (a) 100 shots and (b) 2 million shots. In (b), the thruster's cathode is also visible, showing noticeable erosion.

Another drawback to undervoltage breakdown is erosion of the trigger electrodes. The high voltage pulses delivered to these electrodes result in thermal ablation and ion bombardment, severely limiting their lifetime. Figure 6.3 shows sparkplugs used in the same thruster after only 100 shots had been fired and then again after 2 million shots (expected to be less than the lifetime of a thruster mission) had been fired. Significant erosion is visible. Measurements [17] determined that the sparkplugs lose on the order of 1 μg of material per shot. In this case, the sparkplugs are the thruster's life-limiting component.

We have proposed another discharge initiation technique [51, 52] that employs undervoltage breakdown by using laser pulses directed onto the thruster's cathode to release electrons into the discharge gap. This technique promises uniform current sheet formation with little or no erosion, but the idea is still in development.

Whether or not that technique ever comes to fruition, undervoltage breakdown has enjoyed the most success as a GFPPT discharge initiation mechanism and has the most promise for the reasons outlined above. Though advances in switching technology or additional initiation mechanisms may someday change this picture, for now we will assume that any initiation system will employ undervoltage breakdown as its fundamental mechanism.

That being said, the purpose of the work we present here is not to propose a new discharge initiation technique and tinker with it until we can make it work, nor to survey several possible initiation techniques. Rather, we aim to explore the basic physical phenomena behind PPT discharge initiation, specifically undervoltage breakdown through electron injection, and what specifically is required of an initiation system.

One of the fundamentally unique aspects of undervoltage breakdown in pulsed plasma thrusters is that they operate in a low-pressure parameter regime in which the gain due to ionization avalanches is relatively small. We will see that this leads to distinct breakdown behavior which has only been partially explored.

Because of the problems listed above, an improved discharge initiation system is required if GFPPTs are to become a viable propulsion candidate. Understanding the underlying physics behind how discharge initiation systems work is an important step toward improving them.

6.4 Glow vs Arc, Townsend vs Streamer: What Kind of Discharge Does a GFPPT Need?

The word "breakdown" is generally used to describe the transition of nonconductive neutral gas to conductive plasma, but we have seen that the actual phenomenon is more complex

than the use of one non-specific term implies. The plasma formed during a breakdown can have relatively low or relatively high conductivity and the process by which it breaks down can be relatively slow or relatively fast. Two characteristically different types of breakdown can be achieved through electron pulse injection at an undervoltage, so we will begin by characterizing the breakdown for which a GFPPT initiation system should aim.

Before we start, we should establish some order-of-magnitude guidelines about the parameter space a GFPPT is likely to inhabit. Based on the history of GFPPT development [17], we can say that a thruster consists of two electrodes with a separation distance on the order of 1 cm, a large capacitor bank with capacitance on the order of 100 μF, negligible circuit resistance (which is to say the plasma dominates the resistance), and very small initial inductance, on the order of 100 nH. A well-designed thruster behaves as an RLC circuit whose components are matched to supply a critically damped, or nearly critically damped, current wave form with

$$R = 2\sqrt{\frac{L_0}{C}}, \tag{6.1}$$

where R is the plasma resistance, L_0 the initial inductance, and C the capacitance. Such a relation maximizes energy transfer between the capacitors and the current sheet [17].

Typically a GFPPT is a relatively low-pressure discharge device employing mass bits ranging from 1 μg to a few hundred μg. Though the specifics of gas injection and timing imply complicated and often unknown mass distributions, we can estimate that thrusters and accelerators that have existed in the past were operated at pressures from around 1 mTorr up to several hundred mTorr.

Perhaps the most important guideline for a discharge initiation system to follow is the current rise requirement. In order for well-defined current sheets to form, the current has to increase very rapidly. Jahn [61] reports the experimentally determined rule of thumb that a current rise of 10^{10} A/s per cm of sheet width is required.

6.4.1 Plasma Conductivity

We can expect that a discharge formed in the gap of a GFPPT will take the form either of a low-conductivity glow discharge or a high-conductivity arc discharge – two types of discharge identified by the process by which electrons are emitted from the cathode [21].

A glow discharge relies on secondary emission, primarily through electron bombardment, to emit electrons from a cold cathode. This process is relatively inefficient, so glow discharges are much less conductive than arcs and can be expected to have total plasma resistances on the order of 1 kΩ - 1 MΩ.

An arc discharge employs a hot, thermionically emitting cathode to supply a very large flux of electrons. This very conductive discharge will have a resistance on the order of .1 mΩ - .1 Ω.

We can immediately use our critical damping relation, Equation 6.1, to calculate that a GFPPT, at least one similar to those that have been tested in the past, relies on a plasma resistance on the order of .1 Ω and therefore requires an arc discharge.

6.4.2 Breakdown Time

How quickly does the plasma need to form in a GFPPT discharge? The two distinct mechanisms for DC gas breakdown, Townsend and streamer (see Section 2.1), are characterized by very different timescales.

In a Townsend breakdown, it can be shown [21] that current growth during the breakdown is described by

$$j(t) = j_0 e^{\alpha d}\left[\frac{\mu}{\mu-1}\exp\left(\frac{\mu-1}{\mu}\frac{t}{T}\right) - \frac{1}{\mu-1}\right], \tag{6.2}$$

where j_0 is the initial electron current at the time the breakdown first started (in practice usually due to ambient electrons left over from cosmic ray ionization), α the number of ionizing collisions an electron undergoes per unit length, d the gap width, and T is a transit time. If the breakdown develops as described above, with electrons entering the discharge

gap through secondary emission from the cathode on ion impact, T represents the time it takes an ion to traverse the discharge gap. If, however, the forming plasma becomes bright enough to release electrons from the cathode through photoemission, current growth does not need to wait for ion drifts and the discharge develops faster; T roughly represents the electron transit time. Either way, we can see that plasma forms on the timescale of $\mu T/(\mu - 1)$. In our GFPPT as outlined above, we can expect electron transit times on the order of 100 ns and ion transit times on the order of 10μs. Thus, with a value of μ slightly exceeding 1, we expect formation times that could vary anywhere from the orders of 10 μs to 1 ms.

Streamer breakdown, the second mechanism, occurs much faster. Regardless of the basic physical details of streamer formation, it is clear that streamer breakdown is a mechanism by which plasma can be formed in less than one electron transit time, or for a GFPPT gap, in less than 100 ns.

It should be noted that streamers are usually thought of as a high-pressure (several hundred Torr up to and exceeding one atmosphere), high-overvoltage phenomenon and thus one might find reason to question their relevance in a low-pressure, undervoltage device like a PPT. However, once one accepts gross space charge distortion of the electric field as a necessarily characteristic feature of a streamer, it is not so difficult to imagine that large electron pulses in a low-pressure discharge gap, which will also greatly alter the space charge distribution, may result in streamers. In fact, careful examination of high speed photography of plasma formation in a sparkplug-triggered GFPPT (Figure 6.4) reveals well-defined columns of plasma emanating outward from the sparkplugs that suggest streamers or streamer-like behavior.

The most important concern about discharge formation time in a GFPPT is the current rise requirement stated above. To investigate the effect of breakdown timescale on maximum current rise, we can model the discharge as a RLC circuit with time-varying resistance:

$$\frac{d^2Q}{dt^2} + \frac{R(t)}{L}\frac{dQ}{dt} + \frac{1}{LC}Q = 0, \tag{6.3}$$

(a)

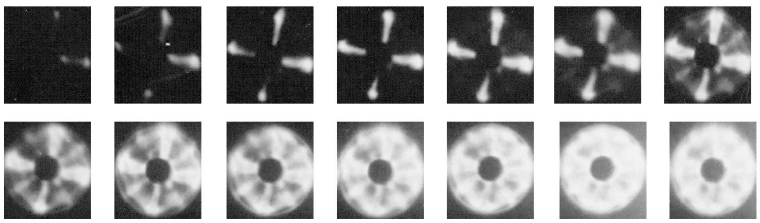

(b)

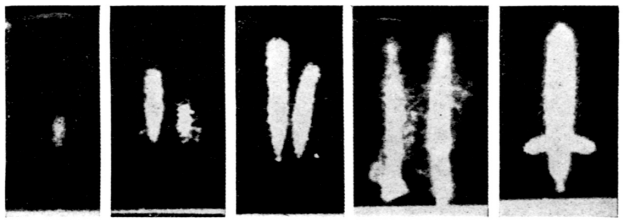

Figure 6.4: (a) High-speed photographs of a discharge in the SRL 5-GFPPT taken from Ziemer et al. [97]. Each exposure is 50 ns long with 500 ns between each. (b) High speed photographs of streamer breakdowns [15].

where Q is the charge on the capacitor bank given by $Q = VC$. Figure 6.5A is a plot of the results of a numerical solution of Equation 6.3 with C of 100 μF, L_0 of 60 nH, and 200V across the electrodes initially. The resistance is linearly ramped from 50 Ω down to .05 Ω over 50 μs, a timescale corresponding to a moderately slow Townsend breakdown. The behavior that we see is quite insightful into the importance of breakdown time on current behavior. The capacitor doesn't really begin to discharge until the resistance gets below some critical value, at which point it seems to proceed with vigor, producing current rise rates within the order of magnitude required to form current sheets for a thruster of our dimensions. Thus, even for this relatively slow breakdown, the maximum current rise attained, $\dot{J}_{max}$, is around 3×10^9 A/s, acceptably close to our rule of thumb stated above that current should rise on the order of 10^{10} A/s for a 1 cm device.

$\dot{J}_{max}$ is plotted versus several orders of magnitude of resistance ramp timescale in Figure 6.5B. What we see is that this quantity has very little sensitivity to breakdown time for most conceivable discharges; it stays within the acceptable range from very fast breakdowns on the order of 100 ns up through much slower ones that take 100 μs. Only the very slowest Townsend breakdown, with a timescale in the ms range, presents possible problems for our discharge initiation system.

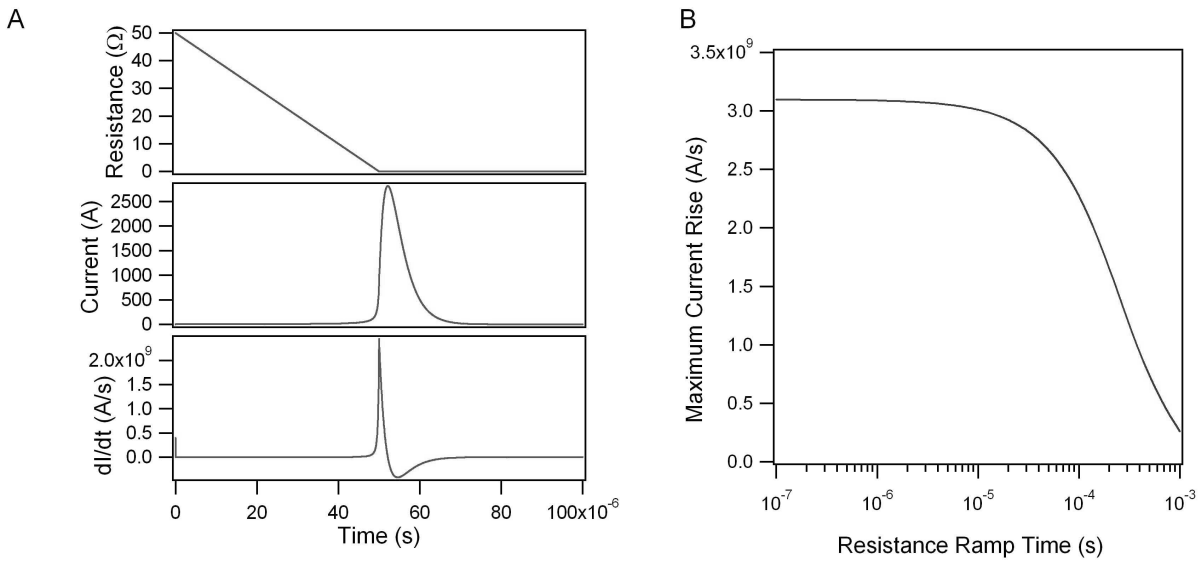

Figure 6.5: (A) Resistance, discharge current, and current rise during a RLC circuit discharge with a linearly ramped resistance. (B) Maximum current rise as a function of resistance ramp time.

Such a linear resistance ramp is unrealistic, and we actually expect exponential increases in conductivity (Equation 6.2), in which the majority of the transition occurs during a small fraction of the overall breakdown time. It thus seems safe to conclude that the timescale of the breakdown process does not affect the rate of current increase when a discharge begins. Thus, from a current sheet formation point of view, any reasonable breakdown mechanism is appropriate.

However, the nature of the breakdown process does affect the *delay* between when the discharge is triggered and when significant current is conducted. Thus, one could imagine several practical considerations that might make faster breakdowns more attractive: the discharge needs to be underway, for example, before the injected gas has a chance to leak out of the thruster, and long delays are undesirable if a high repetition rate is sought. Thus, we can conclude that while Townsend breakdown may be acceptable in GFPPT discharge initiation, streamer breakdown is preferred.

6.5 GFPPT Initiation and Undervoltage Breakdown

Having characterized the requirements a GFPPT discharge initiation system must satisfy, we can now apply some of the insights we gleaned from our analysis of undervoltage breakdown to make some fundamental statements about how those requirements might be met.

One important characteristic of GFPPTs is the relatively low pressure at which they operate. The devices that have been most developed as flight hardware (as opposed to laboratory experiments) are the SRL PT-series discussed in [17]. These were low-mass-bit devices (on the order of 1 μg or less) designed to provide fine positioning for spacecraft. The small mass bits correspond to low pressures in the discharge gap — on the order of 1 mTorr if we assume uniform gas distribution.

A discharge gap of 2 cm using argon at 1 mTorr and a voltage of 250 V (all values typical of an SRL PT device) corresponds to a $\bar{p}$ of about 10^{-3}. Even if we allow for a factor of 100 increase in local gas density due to judicious injection near the sparkplugs, this is still well below the critical value we predicted to be required for undervoltage breakdown through space charge distortion.

In addition, we can use these values to calculate an ionization gain of $e^{\alpha_0 d} \approx 1.02$ for 1 mTorr or $e^{\alpha_0 d} \approx 11$ for 100 mTorr. Since we have argued in this chapter that streamer breakdowns are preferred for GFPPT discharge initiation, and likely occur in these thrusters, it is clear that the devices operate in a surprisingly low-gain regime (recall from Section 2.1.2 that streamers usually occur in high-gain discharge gaps with $e^{\alpha_0 d}$ on the order of 10^8).

Yet, sparkplug discharge initiation at an undervoltage has proven itself to be a successful triggering technique in the SRL PT-series GFPPTs, save for the lifetime and current sheet uniformity issues we have discussed. How do we resolve these discrepancies?

To begin, we should examine more closely our assumptions about the distribution of gas density. Experimental measurements of sparkplug erosion during the operation of

these thrusters showed that the sparkplugs ablate approximately 1 μg of material each time they fire — this is comparable to, or greater than, the mass bit of injected gas. The ablated sparkplug material should temporarily form a high-density region near the cathode, greatly altering the discharge characteristics.

In fact, such a phenomenon, streamer-like breakdown at low gain that relies on material to be ablated or desorbed from the cathode surface, is consistent with our experimental observations and interpretation of the "fast" breakdown mechanism. We never endeavored to fully explore that phenomenon; we speculated that gas desorption plays a significant role, but didn't consider the role of other physical mechanisms such as UV photoionization or multi-dimensional effects. These could play a significant role in GFPPT discharge initiation.

Undervoltage breakdown in general is an attractive approach to initiating current sheet formation in typical GFPPTs. However, achieving the phenomenon through a Townsend-like process by way of a space charge distortion caused purely by an electron pulse should not be possible. Either a transient change in the distribution of gas density, through ablation or desorption, or a thruster design that occupies a different parameter space, such as one that uses higher mass bits, higher voltages, or smaller electrode spacing, is required for undervoltage breakdown to occur.

6.6 Summary and Conclusions

The purpose of this chapter was to understand what is required to initiate discharges in a gas-fed pulsed plasma thruster, specifically from a point of view of plasma conductivity, formation time, and the magnitude of the electron pulse. In doing so, we reached the following conclusions:

- GFPPTs require high-conductivity arc discharges to maximize energy coupling between the capacitors and the current sheet.

- Discharge initiation is insensitive to breakdown timescale, but faster breakdowns are preferable to slower ones because of the delay between triggering and breakdown.
- GFPPTs are inherently low-gain devices (with little electron-avalanche ionization) with $\bar{p}$ values well below the critical value for undervoltage breakdown through space-charge distortion, and below what is typical for streamer breakdown. Material ablated or desorbed near the cathode surface plays an important role in the discharge initiation process.
- A thruster operating at higher $\bar{p}$ — with higher mass bits, higher voltage, or smaller electrode spacings, would be a more favorable environment for discharge initiation through space-charge-triggered streamer breakdown.

This study has focused on the basic mechanism behind GFPPT discharge initiation, but for future investigations we must also consider other practical constraints: the electrons need to be produced in a relatively uniform manner to form relatively uniform current sheets and they need to be produced in such a way that erosion of surfaces is kept to an acceptable level. With that in mind, the next logical step in this line of investigation is a trade study exploring possible undervoltage breakdown techniques such as laser-surface interactions and improved sparkplugs, among others.

Chapter 7

Conclusions

In this thesis, we have described an investigation into undervoltage breakdown through electron pulse injection, specifically focusing on breakdown at low gain through a Townsend-like mechanism. This study has been fundamental in nature, exploring the basic processes at work with an eye toward universally applicable conclusions. At the same time, careful analysis of the circuit dynamics and discharge physics at work in a GFPPT allowed us to make some worthwhile determinations about what is required of the discharge initiation process in these devices.

Previous investigations into undervoltage breakdown have demonstrated the phenomenon in different parameter regimes and shed much light on the relevant physical mechanisms. What has been missing until now is a thorough investigation of threshold criteria, especially at low gain where breakdown is likely to proceed over multiple avalanche generations and where Raether's limit for streamer formation does not apply. Since knowledge of the amount of injected charge required for breakdown is necessary when formulating design criteria for any switching device making use of undervoltage breakdown, and since GFPPTs are inherently low-gain devices, this question is of particular interest.

Thus, this research was carried out with these specific goals in mind:

- Understand the fundamental physics behind undervoltage breakdown through electron pulse injection, specifically through Townsend-like breakdown at low gain.

- Identify experimental conditions under which undervoltage breakdown may occur (or conditions under which it may not occur.)
- For a given set of favorable undervoltage conditions, determine the required areal density of the electron pulse required to achieve breakdown and explore this quantity's dependencies on all relevant parameters.
- From the standpoints of conductivity and formation time, understand what is required for initiating GFPPT current sheet formation.

7.1 Fundamental Insights Into Undervoltage Breakdown

We have experimentally and theoretically explored threshold conditions for undervoltage breakdown, the conditions under which a pulse of electrons will induce breakdown in a low-gain discharge gap that is held below its breakdown voltage. Out of this investigation, we produced numerous fundamental insights.

We identified four similarity parameters which describe the effect of the first electron avalanche on subsequent avalanches. We learned that one of these, $\Pi_1 = Bpd/V$, exhibits a critical behavior, allowing undervoltage breakdown when the parameter exceeds a critical value and prohibiting it otherwise. This critical value varies between 1.6 and 2, depending weakly on two other similarity parameters $\Pi_2 = N_{e0}ed/(\epsilon_0)$ and $\sigma_0 = \alpha_0 d$. Careful examination of the dynamics of the initial electron avalanche is especially fruitful, as it is during this time that the question of whether or not breakdown will occur is decided.

We found through our theoretical investigation that Townsend's classic criteria for breakdown at steady-state, $\mu > 1$, is necessary for undervoltage breakdown, but not sufficient.

We learned that to achieve breakdown at low gain, the space charge distortion must result from the magnitude of the injected pulse, so the injected charge must be significant when compared with the charge on the electrodes. Furthermore, undervoltage breakdown is controlled by electron-impact ionization. It is thus easier as gain is increased, or as that

process' sensitivity to electric field distortion is increased, such as through a reduction of E/p.

In summary, undervoltage breakdown occurs through a manipulation of the process of electron impact ionization through space charge distortion of the electric field, specifically occurring during the initial avalanche caused by the injected electron pulse. Anything that can be done to enhance the role of electron-impact ionization, that phenomenon's sensitivity to changes in electric field, or the degree to which the applied electric field is distorted, will make undervoltage breakdown easier.

7.2 Insights Into GFPPT Discharge Initiation

The problem of discharge initiation in pulsed plasma thrusters inspired our fundamental investigation into undervoltage breakdown. While it was not our stated goal to directly further the development of this technology, we have been able to use the resulting insight, in combination with analysis of plasma and circuit dynamics as they apply to a typical GFPPT, to make some predictions about what specifically will be required of any successful initiation system.

We found that GFPPTs require high-conductivity arc discharges to maximize energy coupling between the capacitors and the current sheet. Therefore, an initiation system will have to produce an avalanche sufficient to heat the cathode above the threshold for thermionic emission.

Discharge initiation is insensitive to breakdown timescale, but faster breakdowns are preferable to slower ones because of the delay between triggering and breakdown. A streamer-type breakdown is therefore preferable for GFPPT discharge initiation. However, GFPPTs are inherently low-gain devices, with $\bar{p}$ values well below the critical value for undervoltage breakdown through space-charge distortion, and $\alpha_0 d$ values below what is typical for streamer breakdown. We observed such a breakdown mechanism in our IR undervoltage breakdown experiments, and learned that material released from surfaces

plays a large role in this process.

Such a mechanism is likely undesirable for a robust system. Alternatively, a thruster operating at higher $\bar{p}$ — with higher mass bits, higher voltage, or smaller electrode spacings, would be a more favorable environment for discharge initiation through space-charge-triggered streamer breakdown.

7.3 Future Work

There is still much to learn about the basic physics of undervoltage breakdown. Exploration of a broader parameter space is likely to reveal processes that play a more significant role than those described in this work. Specifically, we expect field-dependent secondary emission to be important for discharge gaps of high E/p and for contaminated cathodes. In addition, multi-dimensional effects should become significant at higher gain ($\alpha_0 d$) when streamer formation is more likely to occur or when the geometry imposes them, such as an experiment in which electron emission takes place over a smaller cathode area.

The "fast," or streamer-like breakdowns observed in the IR experiments represent an intriguing area of potential study. Occurrences were not numerous enough to allow us to reach quantitative conclusions about this phenomenon, but sparkplug discharge initiation systems in current GFPPT devices likely utilize some form of it. Since our experiment suggested that higher-power laser pulses were more likely to produce fast breakdown, a repeat of the experiment using a more intense laser could achieve the phenomenon with more regularity.

The role of desorbed gases in discharge initiation or undervoltage breakdown in general is still unclear. Numerous experiments could be carried out that would illuminate this phenomenon's contribution to the breakdown process. These include varying the background gas, the cathode temperature, or the laser beam spot size and repetition rate. More sophisticated modeling of the desorption and ionization processes, including such effects as electron attachment, metastable excitation, and dissociation could reveal much

about the interesting behavior observed in the IR experiments.

In order to better understand the breakdown process in actual thruster hardware, a more specified approach could be undertaken. A detailed 2D or 3D numerical model of sparkplug initiation in a GFPPT would likely illuminate the relative roles of the various processes involved, which probably include space charge effects, photo-emission, photo-ionization, gas desorption and chemistry, and multi-dimensional effects. In addition, experimental work could be undertaken in which discharge initiation current is measured during thruster firings while other parameters, such as electrode voltage, mass bit, and sparkplug trigger voltage are varied. Such a combined theoretical and experimental investigation could produce more direct design suggestions for an improved discharge initiation system.

Finally, gas-fed pulsed plasma thrusters are still lacking a robust, efficient discharge initiation system. Optically-triggered initiation systems have been proposed, but this technology is far from developed and numerous technical challenges, such as energy efficiency and surface robustness, have yet to be overcome. Indeed, some other approach, such as longer-lived or intentionally consumable sparkplugs, electron pulses from gated filaments, or something more exotic such as RF preionization [98], may prove to be the most effective technique. A detailed trade study of relevant possibilities, followed by a vigorous development effort, will be required before GFPPTs can be used for demanding missions.

Appendix A

Infrared Laser-Surface Interactions

The technique of using infrared laser pulses as a means for releasing bursts of electrons is an unusual one as the photons do not have enough energy to surpass the work function of suitable cathode materials. The idea that IR laser pulses could induce undervoltage breakdown was discovered accidentally [51] in experiments using a magnesium cathode.

As we have discussed, the phenomenon is likely the result of material desorbed from the surface as a result of the laser heating. However, in trying to understand the phenomenon, we learned of the possibility of a different emission mechanism. Here we present the results of thermal calculations which illuminate the role of thermionic emission. Our goal is to determine the transient temperature distribution near a metal surface and use that information to determine, for a given material, whether thermionic electron emission or vaporization are more likely.

We begin by calculating the temperature in the metal as a function of depth during the laser pulse. We assume that the heat flow is one dimensional, which will later be justified on the basis that the dimension of heat penetration is much smaller than the width of the beam. We also assume that the pulse energy is fully absorbed into the metal.

The differential equation for heat flow in a semi-infinite rod with a heat addition function $A(x,t)$ is [99]

$$\frac{\partial^2}{\partial x^2}T(x,t) - \frac{1}{\kappa}\frac{\partial}{\partial t}T(x,t) = -\frac{A(x,t)}{K}, \tag{A.1}$$

where T is the temperature, κ the thermal diffusivity, and K the thermal conductivity. If the surface is at $x = 0$, the initial and boundary conditions are

$$\begin{aligned} T(x,0) &= 0 \\ T(\infty,t) &= 0 \end{aligned} \tag{A.2}$$

We write our heating function as:

$$A(x,t) = F(t)(1/\delta)e^{-x/\delta}, \tag{A.3}$$

where F(t) is the absorbed laser irradiance in W/cm^2 and δ the skin depth of the metal.

Equation (A.1) is solved using Duhamel's principle, which involves finding the solution for which the temporal pulse shape is a flat step function at $t = 0$. For metals, which have high optical absorption, we get a solution [99]:

$$T(x,t) = \frac{\kappa^{1/2}}{K\pi^{1/2}} \int_0^t \frac{F(t-\tau)\exp(-x^2/4\kappa\tau)}{\tau^{1/2}} d\tau. \tag{A.4}$$

We assume that the laser pulse has the shape:

$$F(t) = I_{\text{peak}}(\frac{t}{T_{width}})^2 \exp{(\frac{-2t}{T_{width}})}. \tag{A.5}$$

Using this laser pulse shape, we numerically integrate Equation (A.4) to find the temperature distribution in the magnesium surface. Figure A.1 is a plot of temperature versus depth with time as a parameter for an 8 ns pulse of energy 170 mJ.

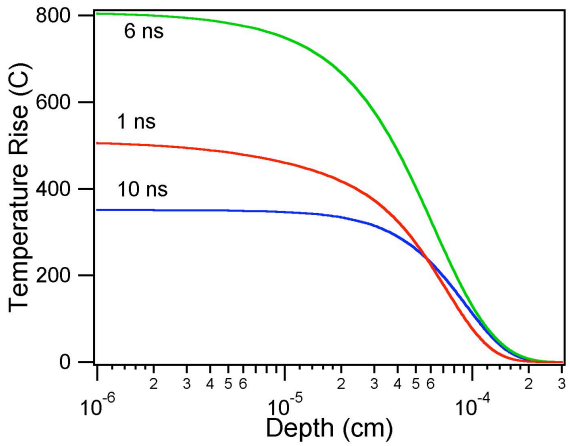

Figure A.1: Temperature distribution in the metal at various times for a laser pulse with $T_{width} = 8ns$ and a pulse energy of 170 mJ.

The temperature of the surface increases during the laser pulse, then drops due to conductive cooling. Note that no significant heating occurs beyond 10^{-3} cm. Since the laser spot size is 1 cm, our assumption of one-dimensionality is valid.

Thermionic electron current density is a function of surface temperature as given by Richardson's equation [20]:

$$j = AT^2 \exp(-\phi/kT), \tag{A.6}$$

where j is the current density in A/cm^2, ϕ is the work function of the metal, and A is a constant equal to $60.2A/(cm^2C^2)$. Magnesium has an electron work function of 3.7 eV.

From this calculation and equation (A.6) we calculate the maximum thermionic electron current from magnesium as a function of laser pulse energy; these results are presented in Figure A.2.

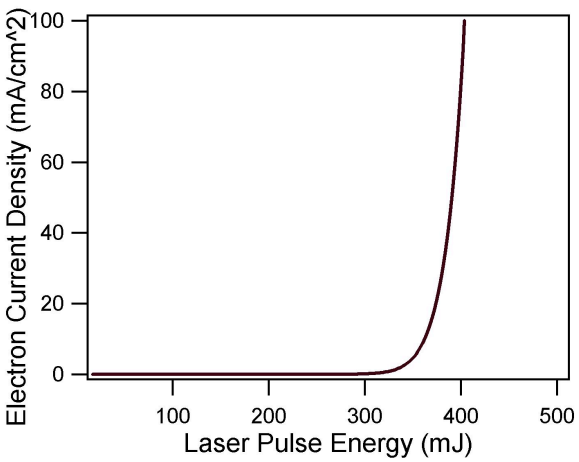

Figure A.2: Maximum electron current density as a function of laser pulse energy.

From Figure A.2 we see that there is essentially no thermionic electron emission until the pulse energy gets above 300 mJ.

However, thermionic emission is not really likely if the surface vaporizes before it reaches the emission threshold. Figure A.3 is a plot of maximum surface temperature rise versus pulse energy for magnesium. The boiling point of magnesium is 1100° C.

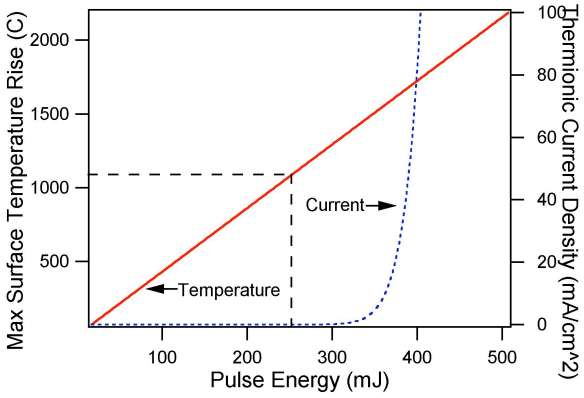

Figure A.3: Maximum surface temperature as a function of pulse energy for magnesium. The dotted line represents the boiling point of magnesium.

Magnesium's temperature threshold for thermionic emission is higher than its boiling point. It is therefore not possible to extract significant thermionic currents from a magne-

sium surface without damaging that surface. Thermionic emission from magnesium would thus not be a viable initiation mechanism for electron pulse extraction for such applications as PPT discharge initiation. However, the same is not true for all materials. For example if the surface were made out of tungsten, which has a much higher melting point than magnesium but comparable work function, it should be possible to extract significant amounts of thermionic current without damaging it. In addition, tungsten has a lower thermal conductivity than magnesium and thus requires lower laser energy to achieve the same temperature. In Figure A.4 we plot the maximum surface temperature and thermionic electron emission in a tungsten surface versus laser pulse energy. The dashed lines indicate the melting point of tungsten. Thus, a tungsten thermionic initiator is not out of the question.

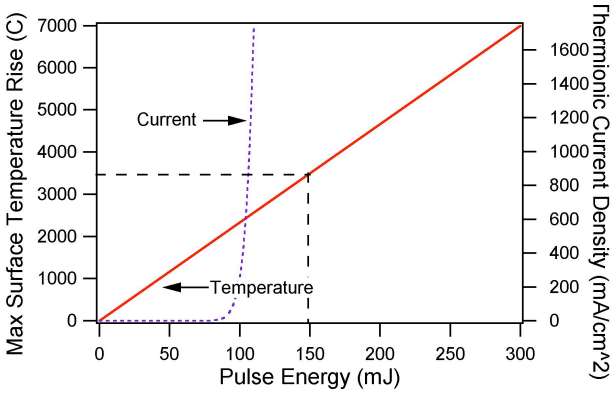

Figure A.4: Maximum surface temperature as a function of pulse energy for tungsten. The dotted line represents the boiling point of tungsten.

Appendix B

Space-Charge Limited Electron Pulses

Accurate use of the pulse calibration procedure described in Section 4.2.1 requires that we understand the difference between electron pulses ejected from the cathode surface into a vacuum, as in the calibration procedure, and those injected into a gas-filled gap, as in the actual experiment. In either case, the total amount of charge that can be released from the cathode is limited by space charge effects; emission stops when the electric field resulting from the injected charge cancels the applied field at the cathode surface, but can restart when a sufficient amount of charge convects out of the volume at the anode. We therefore expect the total amount of deliverable charge in a pulse to depend strongly on the ratio of temporal pulse width to electron transit time.

The fundamental difference between pulses injected into vacuum gaps and pulses injected into gas-filled gaps is thus clear: in the presence of gas, electron transport is dominated by momentum transfer collisions with neutral atoms and the transit time is much greater than that of a vacuum gap, in which electrons are allowed to freely accelerate across the gap.

In this Appendix, we will present an extension of our model that allows us to predict the behavior of electron pulses into vacuum gaps and use that model, along with a ver-

sion of the undervoltage breakdown model already discussed, to calculate a conversion between the amount of charge released by a given laser pulse when the system is under vacuum and the amount of charge we expect to be released by that same laser pulse in the presence of gas.

Here we are concerned only with the development of electron density and electrostatic potential in a 1D vacuum gap. Our governing equations are therefore:

$$\frac{dn_e}{dt} = -\frac{d}{dx}(n_e v_e) \tag{B.1}$$

$$\frac{d^2\phi}{dx^2} = \frac{e}{\epsilon_0} n_e \tag{B.2}$$

$$v_e(x) = \sqrt{\frac{2e\phi(x)}{m_e}}, \tag{B.3}$$

where m_e is the electron mass and the position-dependent electron velocity is calculated through electrostatic energy balance, $1/2 m_e v_e^2 = e\phi$.

The boundary condition for electron flux is:

$$\Gamma_{e0} = \begin{cases} \frac{N_{e0}}{\tau\sqrt{\pi}} e^{\left(\frac{t-3\tau}{\tau}\right)} & \text{if } E(0) > 0, \\ v_e n_e & \text{if } E(0) \leq 0. \end{cases} \tag{B.4}$$

Here we neglect the background current j_0 and secondary emission, which does not occur in the absence of gas. The boundary conditions on the potential are:

$$\phi(0) = 0 \tag{B.5}$$

$$\phi(d) = V. \tag{B.6}$$

Again we will nondimensionalize for universality, dividing as before each variable q by a reference quantity q' to form a dimensionless variable $\bar{q}$. For reference quantities we will use:

$$
\begin{array}{rclcrcl}
N' & = & \dfrac{V\epsilon_0}{ed} & & \phi' & = & V \\
x' = d & & n' = \dfrac{N_{e0}}{x'} & & v' & = & \sqrt{\frac{2eV}{m_e}} \\
t' & = & \frac{x'}{v'} & & \tau' & = & t'
\end{array}
$$

Our choices of reference quantities differ slightly from those employed in the undervoltage breakdown model. Most significantly, the characteristic velocity is chosen as the electron velocity at the anode of the vacuum-filled gap and the characteristic length is chosen as the gap width d. From these quantities, we can easily calculate that the transit time of an electron in an unperturbed field is $\bar{T}_e = 2\bar{t}$.

Our dimensionless governing equations become:

$$
\frac{d\bar{n}_e}{d\bar{t}} = \frac{d}{d\bar{x}}\left(\bar{n}_e\bar{v}_e\right) \tag{B.7}
$$

$$
\frac{d^2\bar{\phi}}{d\bar{x}^2} = \bar{N}_{e0}\bar{n}_e \tag{B.8}
$$

$$
\bar{v_e} = \sqrt{\bar{\phi}}. \tag{B.9}
$$

The dimensionless boundary conditions are:

$$
\bar{\Gamma}_{e0} = \begin{cases} \frac{1}{\bar{\tau}\sqrt{\pi}} e^{\left(\frac{\bar{t}-3\bar{\tau}}{\bar{\tau}}\right)} & \text{if } \bar{E}(0) > 0, \\ \bar{v}_e\bar{n}_e & \text{if } \bar{E}(0) \leq 0. \end{cases} \tag{B.10}
$$

$$
\bar{\phi}(0) = 0 \tag{B.11}
$$

$$
\bar{\phi}(\bar{x}=1) = 1. \tag{B.12}
$$

We will also introduce another convenient dimensionless parameter to describe the time-width of the injected pulse, $X \equiv \tau/T_e$, where T_e is again the vacuum transit time of an electron.

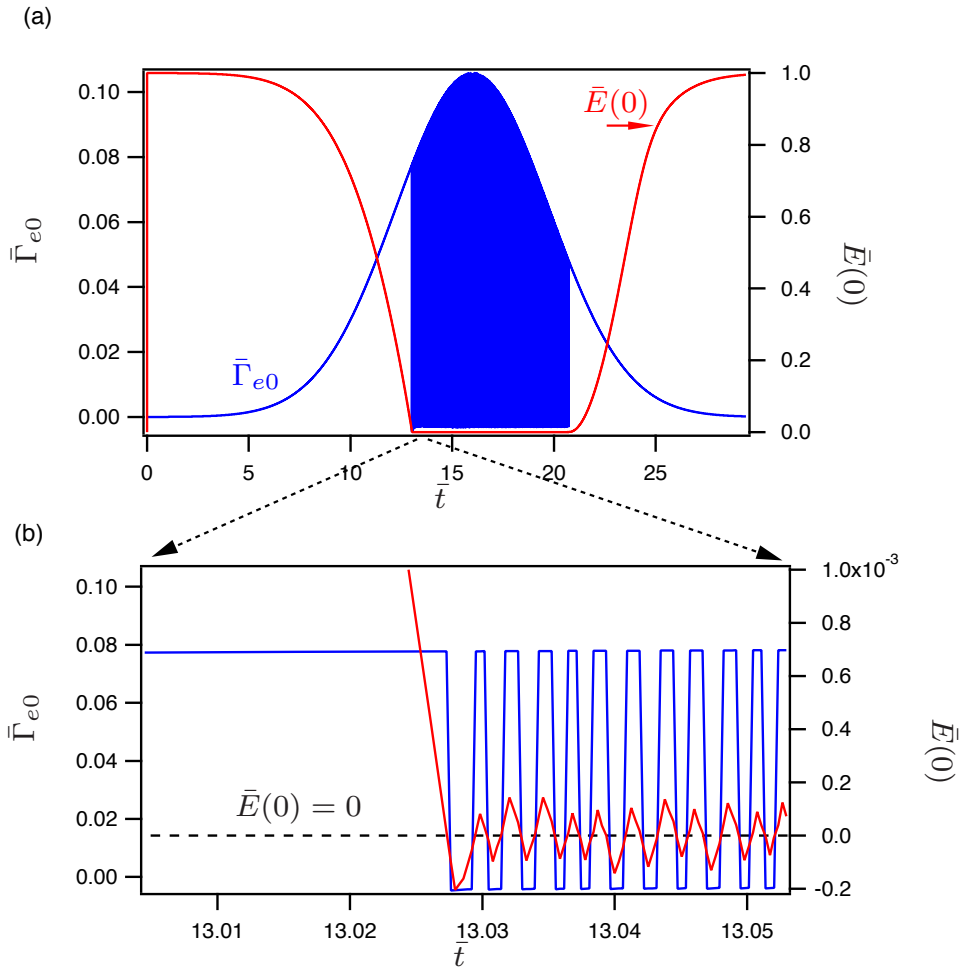

Figure B.1: (a) Cathode electron flux (blue) and cathode electric field (red) vs $\bar{t}$ during a vacuum pulse of $\bar{N}_{e0} = 10$ and X=2.7. Exploded view in (b). The dotted line in (b) refers to zero electric field.

We use the same numerical method as in the undervoltage breakdown model to calculate the development of electron density and current while an electron pulse is injected into vacuum. In Figure B.1 we plot electron flux from the cathode during an injected pulse as well as $\bar{E}$ at the cathode as a function of dimensionless time for a pulse that exceeds the space charge limit. The Gaussian envelope of the injected pulse is clearly discernable, but as the electric field becomes negative, cathode emission ceases. After a short time, some electrons have left the volume at the anode, the field becomes positive again, and emission temporarily resumes, only to be cut off again when the space charge limit is exceeded. These oscillations continue until the pulse intensity drops below a certain limit. Clearly, the total amount of charge injected into this gap is less than it would have been in the absence of space charge limitations.

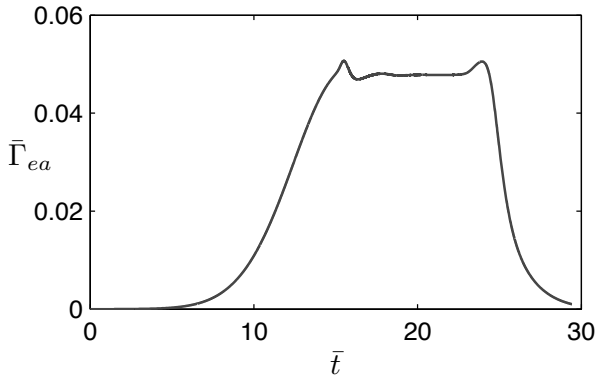

Figure B.2: Dimensionless electron flux at the anode during a vacuum pulse.

Examining the dimensionless electron flux at the anode (Figure B.2) gives us an idea of what the measured circuit current would look like in an actual experiment. By the time the electrons traverse the gap, electrostatic repulsion causes the individual bursts of electrons released by the oscillations at the cathode to bleed together, achieving a quasi-steady current. This is the current limit predicted by the Child-Langmuir law:

$$J_{cl} = \frac{4\epsilon_0}{9d^2}\sqrt{\frac{2e}{m_e}}V^{3/2}. \tag{B.13}$$

It follows that if $X \gg 1$, the critical charge that can be introduced into a gap can be approximated by $Q_{\text{crit}} = \tau J_{cl}$.

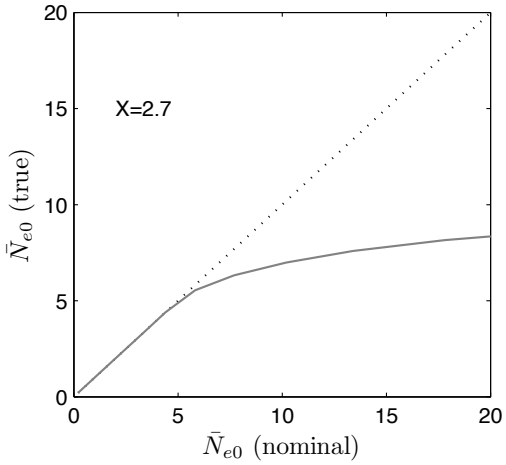

Figure B.3: True $\bar{N}_{e0}$ actually emitted from the cathode versus nominal $\bar{N}_{e0}$ applied. The dashed line is the nominal $\bar{N}_{e0}$ plotted against itself. Here the pulse width $\bar{\tau}$ is 2.7 times the vacuum transit time.

In Figure B.3, we plot N_{e0} as actually emitted from the cathode versus the nominal N_{e0} supplied for $X = 2.7$. As the applied pulse becomes large, the true injected pulse density nearly reaches a critical value.

When an electron pulse is injected into a gas-filled gap, ionization avalanching occurs as we have discussed, which results in complex, time-varying distributions of electron density, ion density, and electric field. However, because each ionization event results in the introduction of both an ion and an electron, no additional charge is created, and the injected pulse itself accounts for the total charge in the gap until the first avalanche reaches the anode. We thus expect that the behavior of the injected charge limit should resemble that of the vacuum case, except that the electron transit time is longer for a given voltage, and thus X is smaller. Therefore, we can predict that the amount of charge released at a given voltage in the presence of gas should be smaller than that released at the same voltage from the same pulse into vacuum, and that increasing the pressure should in turn decrease the emitted charge.

It is straightforward to verify such a supposition using “Phase I” of our undervoltage breakdown model, (Section 3.3) which describes the evolution of the relevant variables during the first electron avalanche.

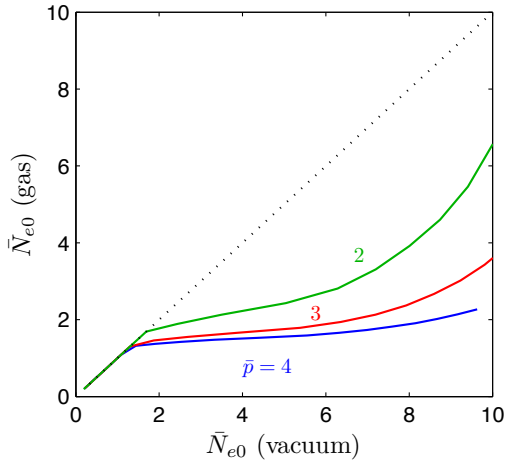

Figure B.4: True $\bar{N}_{e0}$ released from the cathode in the presence of gas as a function of the $\bar{N}_{e0}$ that would be released from the same pulse at the same voltage in vacuum. Curves for three different normalized pressures are plotted.

By applying the same pulse first to a vacuum gap and then to a gas-filled gap at a specified dimensionless pressure, we can calculate how much charge we expect to be released into the gas filled gap (as during an undervoltage breakdown experiment) as a function of charge released into a vacuum gap (as during a pulse calibration). Figure B.4 contains plots of the emitted $\bar{N}_{e0}$ into gas-filled gaps versus $\bar{N}_{e0}$ emitted into vacuum-filled gaps for $\bar{p}$'s of 2, 3, and 4 (roughly the values achieved in the experiments.) We see that, as we speculated, less charge is released in the presence of gas than into vacuum, and increasing dimensionless pressure (equivalent to decreasing transit time) decreases the emitted charge.

Using this technique, along with our experimental calibration procedure, we can accurately calculate the amount of charge released during a shot of an undervoltage breakdown experiment as a function of photodiode signal.

Appendix C

Parameter Space Occupied by the Undervoltage Breakdown Experiment

Before comparing the theoretical predictions of the non-dimensional undervoltage breakdown model to the experimental results, we should first specify the values of the relevant parameters that correspond to the range of experimental conditions.

All the experiments were carried out using research-grade argon of 99.9997% purity at pressures ranging from 1.4 Torr to 3 Torr. The electrode separation was held fixed at 1 inch and voltages ranging from 330 to 400 V were delivered to the plates. The photoelectric cathode was oxygen-free, high-conductivity copper polished to 10 μm smoothness. The cathode used in the infrared experiments was tungsten.

E/n and α_0

Because many important discharge parameters are found to scale with the ratio of applied electric field to neutral density or pressure (reduced electric field) and are reported as functions of these parameters, it will be convenient for us to identify the range of E/n and

E/p values we explored. Using units of Townsends (1 Td=10^{21} V m^2), we calculate that values of E/n ranged from 142 Td to 323 Td. Assuming a temperature of 300°K, we find that the E/p ranged from 45 to 104 V/cm Torr.

The Townsend A and B coefficients used to calculate α (Equation 3.11) are known to vary with E/n. Using published data, Phelps and Petrovic [43] calculated an empirical fit that reasonably predicts α for a wide range of E/n:

$$\begin{aligned} \alpha/n &= 1.1 \times 10^{-22} \exp[-72/(E/n)] \\ &\quad +5.5 \times 10^{-21} \exp[-187/(E/n)] \\ &\quad +3.2 \times 10^{-20} \exp[-700/(E/n)] \\ &\quad -1.5 \times 10^{-20} \exp[-10000/(E/n)], \end{aligned} \tag{C.1}$$

where α/n is in m^2 and E/n is in Td. This empirically determined formulation incorporates many ionization processes (electron impact, photoionization, metastable collisions, "fast ions") and is meant to be universally applicable over a wide range of E/n. However, for a narrower E/n regime, not all terms contribute, and a simpler, Townsend-like approximation will suffice.

For our case, we fit the published data to:

$$\alpha/n = C \exp\left(\frac{-D}{E/n}\right) \tag{C.2}$$

over the range of 142-323 Td (Figure C.1.) This returns values of $C = 2.77 \times 10^{-20}$ m^{-2} and $D = 443.42$ Td, which at 300 K is equivalent to $A = 892$ m^{-1} Torr^{-1} and $B = 14280$ V m^{-1} Torr^{-1}. This gives α_0's ranging from 20-107 m^{-1} and $e^{\alpha_0 d}$ values ranging from 12.8 to 38.2. These values are used to calculate the various dimensionless parameters needed in Chapter 5 when comparing the experimental data with theoretical predictions.

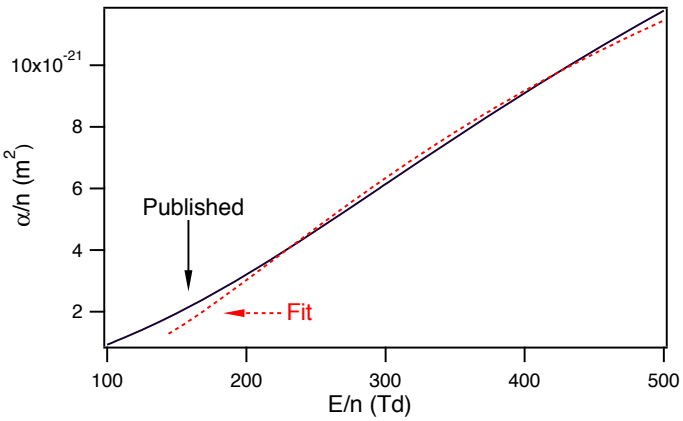

Figure C.1: Empirically determined α/n for argon from [43] with a fit of the form $\alpha/n = C\exp\left(\frac{-D}{E/n}\right)$. The fit returns $C = 2.77 \times 10^{-20}$ m^{-2} and $D = 443.42$ Td.

Secondary Emission

Secondary electron emission from a cathode is a phenomenon that encompasses several different processes and depends strongly on such factors as gas purity, surface contamination, and surface smoothness and geometry, all of which are notoriously difficult to control in a laboratory environment. As a result, the secondary emission coefficient and its dependencies are perhaps the least well-known of all experimental discharge parameters. Still, enough theoretical and experimental data exist in the literature to make reasonable predictions about γ for our setup.

Two important assumptions we made about secondary emission in our theoretical analysis were that the processes is dominated by ion impact at the cathode and that the secondary emission coefficient is independent of electric field and pressure. These assumptions do not hold universally, but were made for clarity and are applicable in certain circumstances.

In Figures C.2 and C.3 we show theoretical predictions and experimental data for secondary emission in argon discharges on both clean and dirty metallic cathodes from [43]. Here “clean” refers to atomically pure surfaces free of oxidation or other impurities while “dirty” cathodes are exposed to such contamination. Figure C.2 (a) presents theoretical

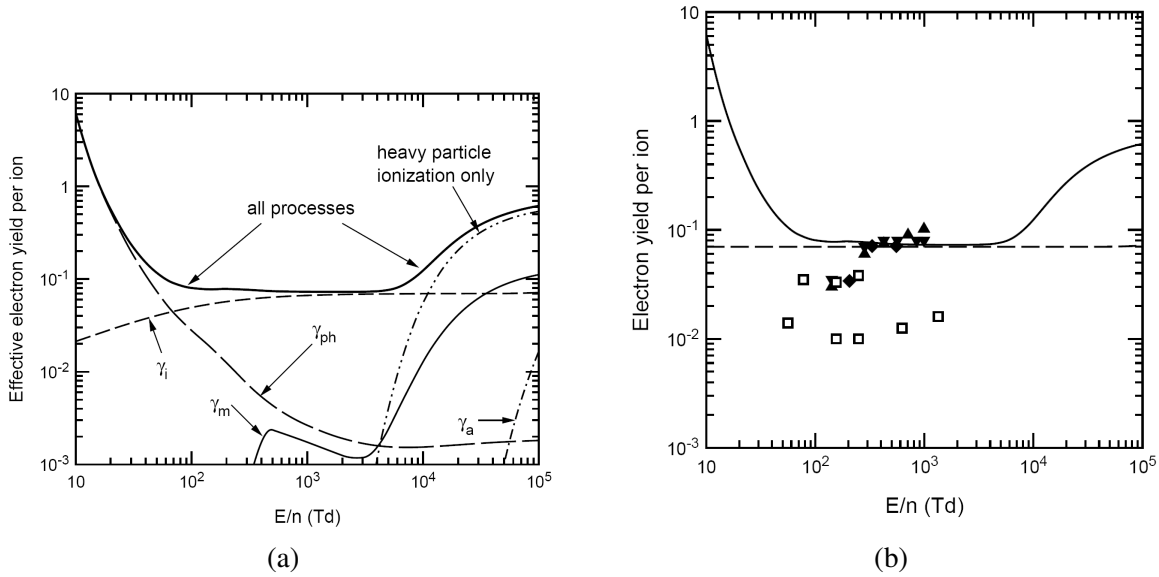

(a) (b)

Figure C.2: Secondary emission coefficient as a function of E/n for argon on clean surfaces from [43]. (a) presents theoretically calculated curves of the various contributions of secondary emission processes: γ_i corresponds to secondary emission through ion impact, γ_{ph} through photoelectric emission, γ_a through fast ion impact, and γ_m through impact of atoms excited to metastable states. In (b), we see the theoretical curve for all processes overlayed with experimental data for various cathode materials. □'s are copper.

predictions not only of the total secondary emission coefficient, but also of the contributions from all significant secondary emission processes: ion impact at the cathode, photon impact at the cathode, impact of fast neutrals created through charge-exchange collisions, and impact of neutrals excited to metastable states.

In the range explored by our experiment, E/n ranging from 143 to 323 Td, we can see that γ is reasonably independent of that parameter for clean cathodes. Furthermore, secondary emission is dominated by ion impact and no other process is relevant. The theory predicts a value of $\gamma \approx .07$ while the experimental data in Figure C.2 (b) shows slightly lower values, ranging from about .01 to .03.

Figure C.3 shows the same information but for "dirty" (oxidized or contaminated) cathodes. In this case, the behavior is quite different. Instead of γ being constant, it varies significantly with E/n and the dependence is non-monotonic, though it should be noted that our E/n range of interest coincides with region of the curve where the dependence is

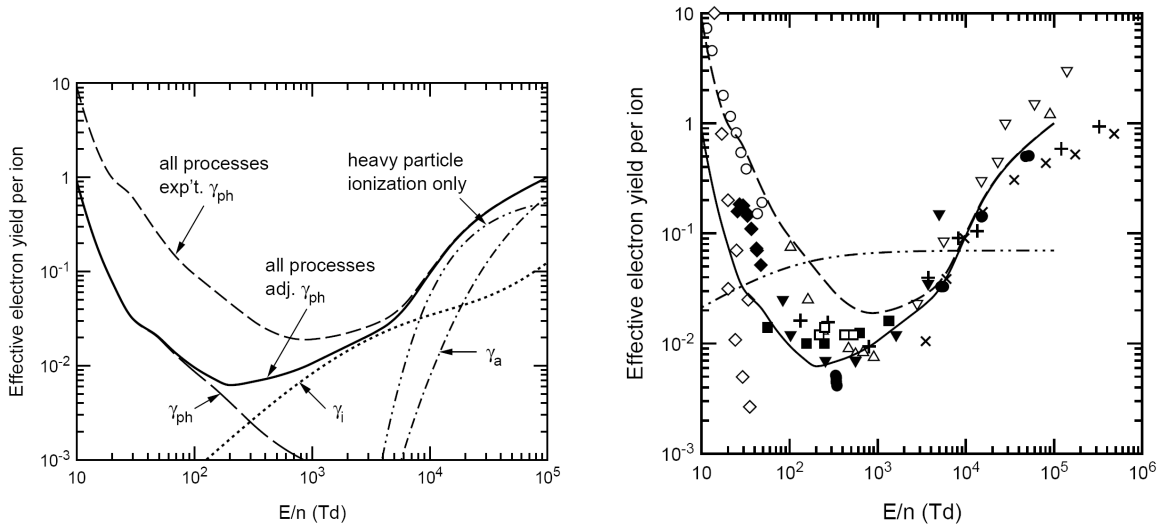

Figure C.3: Secondary emission coefficient for argon on dirty surfaces from [43]. (a) Theoretical contributions of various secondary emission processes. (b) Experimental data, ■'s are copper.

weakest. The magnitude of γ_i is lower and emission through photon impact is significant at low E/n. From these curves, we can estimate a secondary emission coefficient of $\gamma \approx .01$.

Particle Loss

We can define a "lifetime" of a loss mechanism as:

$$\tau = \frac{1}{\beta n_e^0}, \tag{C.3}$$

where the electron density decay proceeds as

$$\frac{dn_e}{dt} = -\beta n_e n_+. \tag{C.4}$$

In our case, breakdown occurs on the order of several μs, and our theory predicts that much is decided during the first electron avalanche transit, which occurs in about 100 ns. If the lifetime is much larger than these timescales, we can safely neglect that process.

In a weakly ionized plasma, the fastest loss mechanism is usually dissociative recom-

bination [21], which occurs according to the reaction:

$$A_2^+ + e \rightarrow A + A^*.$$

The rate at which this mechanism progresses is often dominated by the rate of formation of molecular ions, and is hence pressure-dependent. Radiative recombination through a two-body collision ($A^+ + e \rightarrow A + h\nu$) tends not to be a channel for electron removal because the cross section is quite small (on the order of 10^{-21} cm^2), though it can be an important mechanism for light emission. Radiative recombination through three-body collision ($A^+ + e + e \rightarrow A + e$) can be important for higher density plasmas or for cases in which the rate of production of molecular ions is small.

Electrons can also be lost when they diffuse to walls or otherwise out of the discharge volume. For the process, the mean electron lifetime will be

$$\tau_{\text{dif}} = \frac{\Lambda^2}{D}, \tag{C.5}$$

where Λ is relevant length scale of the electrodes (1 cm in our case) and D the appropriate diffusion coefficient. Early in the breakdown process, the electrons will experience free diffusion, but as space charge builds over several avalanches, ambipolar diffusion will become more significant and the rate of electron loss will slow.

In Table C.1, we list the lifetimes of these loss processes for the pressures used in our experiment assuming an electron density on the order of 10^{16} m^{-3}, a reasonable estimate for the majority of the discharge process. Rate constants and diffusion coefficients are from published data found in [21] and [22].

Free diffusion, which likely occurs only during the first avalanche, has a lifetime on the order of a μs — longer than the transit time of that avalanche. For the other processes, we can see that the shortest particle lifetime is on the order of 10^{-4} s, much longer than our breakdown timescale. Thus, it is reasonable to neglect particle loss in our analysis.

Loss Process	Lifetime (s) at 1 Torr	Lifetime at 2 Torr	Lifetime at 3 Torr
Dissociative Recombination	4.82×10^{-3}	1.21×10^{-3}	5.36×10^{-4}
Radiative Recombination	1×10^{2}	1×10^{2}	1×10^{2}
3-body Recombination	3.63×10^{3}	3.63×10^{3}	3.63×10^{3}
Free Diffusion	2.02×10^{-6}	4.03×10^{-6}	6.05×10^{-6}
Ambipolar Diffusion	5.84×10^{-4}	1.17×10^{-3}	1.75×10^{-3}

Table C.1: Loss processes and associated lifetimes

Mobility

Our use of the parameter μ_+/μ_e in the theoretical formulation carries with it the implied assumption that this parameter is constant and varies neither with electric field nor neutral pressure. This assumption is not universally applicable, but does hold within certain parameter regimes. Both the electron and ion mobilities scale with E/p, so it is valid to express the ratio of these quantities as constant as long as the dependence is linear in both cases.

Figure C.4 contains a plot of electron mobility and drift velocity in argon as presented in [22]. We see that in the E/p range of interest (from about 40 V/cm Torr to 100 V/cm Torr), the mobility is not a linear function of E/p, but varies weakly with that parameter, ranging from about 2.4 $\times 10^5$ to 2.6 $\times 10^5$ cm^2 Torr/V s, with a significant deviation from linearity only at the lowest E/p. In Figure C.5, we show drift velocity data of Ar^+ in Ar as presented in [21]. Again, the drift velocity ($v_d = \mu_+ E$) does not have a universally linear relationship to E/p, (the dashed curve on the left represents a linear fit) but the approximation is reasonable within the range of interest. Using these data, we can calculate that a mobility ratio of $\mu_+/\mu_e = 290$ is a reasonable estimate of that parameter for all of our experimental conditions.

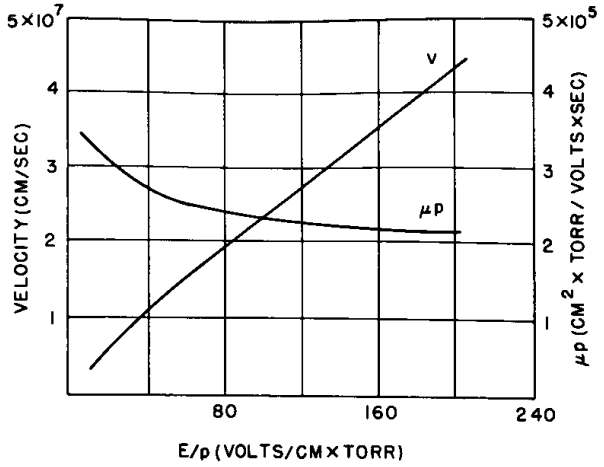

Fig. 4.29 Drift velocity and mobility of electrons in argon.
V. E. Golant (1959)
SPTPHY J790 V4 P680

Figure C.4: Electron mobility and drift velocity as a function of E/p from [22]

Electron Kinetics

Several aspects of our theoretical framework, including our use of a Townsend approach to describe localized ionization, and a drift velocity-based description of electron motion, rely on the implicit assumption that the mean electron energy is reasonably small. Specifically, our approach requires that electron energy is well below the energies that correspond to the maxima of the cross sections of relevant inelastic scattering processes.

There are two situations in which we might expect this assumption to be violated. The first is the existence of a region of high enough E/n that the electrons gain more than about 20-50 eV between collisions. The average energy gained between collisions is [21]:

$$\Delta\varepsilon = \frac{e^2 E^2}{m\nu_m^2} \tag{C.6}$$

Using a momentum transfer collision frequency of $\nu_m/p = 5.3 \times 10^9 \text{s}^{-1}\text{Torr}^{-1}$ (from [21]), we get at $E/p = 104$ V cm^{-1} Torr^{-1} an average energy gain between collisions of about 0.7 eV. This is well below the energy at which we expect runaway electrons or nonlocal

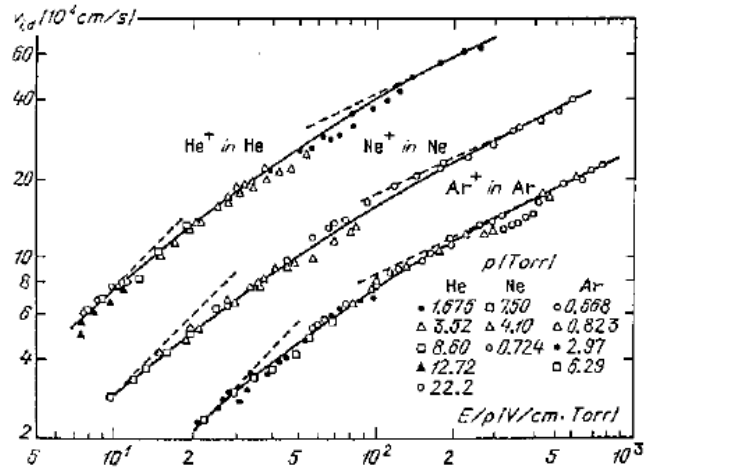

Fig. 2.9. Drift velocities of ions in inert gases. Change in mobility laws: from $v_{id} \sim E$ (*dashed line* on the left) to $v_{id} \sim \sqrt{E}$ (*dashed line* on the right); $T = 300$ K. From [2.17]

Figure C.5: Ion drift velocity as a function of E/p from [21]

ionization effects.

Our "cold electron" assumption might also be violated if the electrons are injected from the cathode with significant initial energy. However, the surface of a conductor behaves as a potential well with a depth equal to the work function. Photoelectrically released electrons will leave the surface with whatever kinetic energy is left over after climbing through that potential. The mean electron energy after photoelectric emission will therefore be equal to whatever the mean energy of the electrons in the conduction band of the metal have plus the *difference* between the photon energy and the work function. The work function of copper is 4.65 eV, which is very close to the photon energy at 266 nm: 4.66 eV. The photons free the electrons from the surface, but give them only about .01 eV of excess kinetic energy.

We therefore expect the injected electrons to be relatively cold, and our approach of Townsend ionization and drift velocity dynamics should be valid.

One-Dimensionality

It is clear that the experiment is not strictly one-dimensional; while the parallel-plate electrodes provide a uniform electric field, and insulating coating isolates the discharge in the center of the electrode area far from the fringing fields at the edges, the laser does not uniformly illuminate the entire cathode area. Instead, the angle of incidence of the laser is such that the irradiated area is elliptical and roughly 2.3 cm long by .8 cm wide in the UV case, and 2.9 cm long by 1 cm wide in the IR case. Such distributions are smaller than the total area of the electrodes, which have 5 cm $\times$ 5 cm of exposed surface. However, each dimension of the discharge is longer than the free diffusion length of an electron during a single avalanche transit (about 1 mm). Thus, multi-dimensional, diffusion-based analyses, such as that employed by Raether in calculating streamer formation as started from a single electron, are not required. A 1D analysis, while not completely accurate, should capture the essence of the most important physical processes.

Bibliography

[1] R. Kluckow. Über den zeitlichen verlauf des stromes einer gasentladung in wasserstoff. *Z. Phys. A*, 161(4), Aug 1961.

[2] N. Sato and S. Sakamoto. Undervoltage breakdown between parallel plates in air. *J. Phys. D: Appl:Phys*, **12**:875–886, 1979.

[3] M.F. Frechette, N. Bouchelouh, and R.Y. Larocque. Laser-induced undervoltage breakdown in atmospheric N_2 correlated with time-resolved avalanches. In *IEEE International Sumposium on Electrical Insulation*, Pittsburgh, PA, June 5-8 1994.

[4] R.N. Varney. Liberation of electrons by positive-ion impact on the cathode of a pulsed townsend discharge tube. *Phys Rev*, 93:1156, 1954.

[5] H. Schlumbohm. The temporal development of a Townsend discharge. *Z. Phys.*, 159:212, 1960.

[6] P. Fonte. A model of breakdown in parallel-plate detectors. *IEEE Transactions on Nuclear Science*, **43**(3):2135, June 1996.

[7] J.E. Cooley and E.Y. Choueiri. Fundamentals of discharge initiation in gas-fed pulsed plasma thrusters. In 29^{th} *International Electric Propulsion Conference*, Princeton, New Jersey, September 2005. IEPC 2005-153.

[8] T.E. Broadbent. The breakdown mechanism of certain triggered spark gaps. *British Journal of Applied Physics*, 8:37, January 1957.

[9] T.E. Broadbent, C.T. Elliott, and A.H.A Shlash. Spark initiation in small trigatrons. *British Journal of Applied Physics*, 15:1118, March 1964.

[10] J.T. Kennedy, J.M. Wetzer, and P.C.T. van der Laan. Space charge induced breakdown in under-volted gaps in nitrogen and air. In *8th International Symposium on High Voltage Engineering*, Yokohama, Japan, August 23-27 1993.

[11] P. Fonte, V. Peskov, and F. Sauli. Feedback and breakdown in parallel-plate chambers. *Nuclear Instruments and Methods in Physics Research A*, **305**:91, 1991.

[12] J.E. Cooley and E.Y. Choueiri. Fundamentals of PPT discharge initiation: Undervoltage breakdown through electron pulse injection. In 39^{th} *Joint Propulsion Conference*, Huntsville, AL, 2003. AIAA-2003-5027.

[13] J.D. Craggs, M.E. Haine, and J.M. Meek. The development of triggered spark gaps for high power modulators. *Journal I.E.E.*, 93:963, 1946.

[14] K. Frank and J. Christiansen. The fundamentals of the pseudospark and its applications. *IEEE Transactions of Plasma Science*, 17(5):748, October 1989.

[15] H. Raether. *Electron Avalanches and Breakdown in Gases*. Washington, D.C., Butterworth Co, 1964.

[16] R.G. Jahn and E.Y. Choueiri. Electric propulsion. In *Encyclopedia of Physical Science and Technology, 3rd edition,* vol. 5, pages 125–141, Academic Press, San Diego, CA, 2002.

[17] J.K. Ziemer. *Scaling Laws in Gas-fed Pulsed Plasma Thrusters*. PhD thesis, Dept. of Mechanical and Aerospace Engineering, Thesis No. 3016-T, Princeton University, Princeton, NJ, 2001.

[18] J.E. Cooley and E.Y. Choueiri. Threshold criteria for undervoltage breakdown. *Journal of Applied Physics*, 103(1), Accepted for publication February 2008.

[19] J.S. Townsend. *Electricity in Gases*. Oxford, Clarendon Press, 1915.

[20] J.D. Cobine. *Gaseous Conductors: Theory and Engineering Applications*. Dover Publications, 1958.

[21] Y.P. Raizer. *Gas Discharge Physics*. Springer-Verlag, 1997.

[22] S.C. Brown. *Basic Data of Plasma Physics*. M.I.T. Press, 1966.

[23] J.M. Meek and J.D. Craggs. *Electrical Breakdown of Gases*. Clarendon, 1953.

[24] R.V. Hodges, R.N. Varney, and J.F. Riley. Probability of electrical breakdown: evidence for a transition between the Townsend and streamer breakdown mechanisms. *Phys Rev A*, **31**(4):2610, April 1985.

[25] H. Raether. Die entwicklung der elektronenlawine in den funkenkanal. *Zeitschrift Für Physik*, 112:464, 1939.

[26] L.M. Chanin and R.D. Steen. Mobilities of cesium ions in cesium. *Phys. Rev.*, 132(6):2554–2557, Dec 1963.

[27] S. Bachmanna, A. Bressana, S. Kapplerb, B. Ketzera, M. Deutela, L. Ropelewskia, F. Sauli, and E. Schultec. Development and applications of the gas electron multiplier. *Nuclear Ints. Meth. A*, 471(1-2):115–119, Sep 2001.

[28] A. Bressan, M. Hoch, P. Pagano, L. Ropelewski, F. Sauli, S. Biagi, A. Buzulutskov, M. Gruwe, G. De Lentdecker, D. Moermann, and A. Sharma. High rate behavior and discharge limits in micro-pattern detectors. *Nuclear Ints. Meth. A*, 424(2):321–342, Mar 1999.

[29] F. Sauli. Micro-pattern gas detectors. *Nuclear Ints. Meth. A*, 477(1-3):1–7, Jan 2002.

[30] A. Kozlova, I Ravinovicha, L. Shekhtman, Z. Fraenkela, M. Inuzukab, and I Tserruya. Development of a triple GEM UV-photon detector operated in pure CF_4 for the PHENIX experiment. *Nuclear Inst. Meth. A*, 523(3):345–354, May 2004.

[31] V. Peskov, P. Fonte, M. Danielsson, C. Iacobaeus, J. Ostling, and M. Wallmark. The study and optimization of new micropattern gaseous detectors for high-rate applications. *IEEE Transactions on Nuclear Science*, 48(4):1070–1074, Aug 2001.

[32] C. Montijn and U. Ebert. Diffusion correction to the raether-meek criterion for the avalanche-to-streamer transition. *J. Phys D: Appl. Phys*, 39:2979, June 2006.

[33] R.K. Bock. *The Particle Detector Briefbook*. Springer, 1998.

[34] G. Brubaker and E. Pollard. Properties of the proportional (geiger-klemperer) counter. *Review of Scientific Instruments*, 8:254–258, 1937.

[35] H. Geiger and O. Klemperer. Beitrag zur wirkungsweise des spitzenzählers. *Zeitschrift Für Physik*, 49(753), 1928.

[36] H. Fränz. Zertrümmerungsversuche an bor mit a-strahlen von Ra C'. *Zeitschrift Für Physik*, 63:370, 1930.

[37] H. Klarmann. Die künstliche umwandlung des magnesiums durch polonium-a-teilchen. *Zeitschrift Für Physik*, 87:411, 1934.

[38] W.E. Duncanson and H. Miller. Artificial disintegration by radium c' α-particles-aluminium and magnesium. *Proceedings of the Royal Society*, A146:396, 1934.

[39] J. Christiansen. Selbstlöschende parallelplatten-dampfzähler bei spannungen unterhalb der statischen durchschlagsfeldstärke. *Z. angew Phys*, **4**(4):326, 1956.

[40] W. Pendleton and A. Guenther. Investigation of a laser triggered spark gap. *Review of Scientific Instruments*, 36(11):1546, November 1965.

[41] M.J. Kushner, R.D. Milroy, and W.D. Kimura. A laser-triggered spark gap model. *Journal of Applied Physics*, 58(8):2988, October 1985.

[42] Y. Kowada and T. Hosakawa. Breakdown mechanism of a laser-triggered spark gap in a uniform field gap. *Journal of Applied Physics*, 62(6):2237, September 1987.

[43] A.V. Phelps and Z.L. Petrovic. Cold-cathode discharges and breakdown in argon: surface and gas phase production of secondary electrons. *Plasma Sources Sci. Technol*, **8**(R21), 1999.

[44] V. I. Kolobov and A. Fiala. Transition from a townsend discharge to a normal discharge via two-dimensional modeling. *Phys. Rev. E*, 50(4):3018–3032, Oct 1994.

[45] J.D. Pace and A.B. Parker. The breakdown of argon at low pressure. *J Phys D Appl Phys*, 6:1525, 1973.

[46] A. Von Engel and M. Steenbeck. *Elektrische Gasentladungen*. Verlag Von Julius Springer, 1932.

[47] D. Šijačić and U. Ebert. Transition from townsend to glow discharge: Subcritical, mixed, or supercritical characteristics. *Physical Review E*, **66**:066410, 2002.

[48] G.I. Barenblatt. *Similarity, Self-Similarity, and Intermediate Asymptotics*. Cambridge University Press, 1996.

[49] R. Leveque. *Finite Volume Methods for Hyperbolic Problems*. Cambridge University Press, 2002.

[50] W. Press, S. Teukolsk, W. Vetterling, and B. Flannery. *Numerical Methods in C*. Cambridge University Press, 2002.

[51] J.W. Berkery and E.Y. Choueiri. Laser discharge initiation for gas-fed pulsed plasma thrusters. In 37^{th} *Joint Propulsion Conference*, Salt Lake City, UT, 2001. AIAA-2001-3897.

[52] J.E. Cooley and E.Y. Choueiri. IR-assisted discharge initiation in pulsed plasma thrusters. In 38^{th} *Joint Propulsion Conference*, Indianapolis, IN, 2002. AIAA-2002-4274.

[53] J.D. Jackson. *Classical Electrodynamics*. Wiley, 1975.

[54] C.D. Child. Discharge from hot CaO. *Phys Rev*, 32(5):492, May 1911.

[55] I. Langmuir. The effect of space charge and initial velocities on the potential distribution and thermionic current between parallel plane electrodes. *Phys Rev*, 21(4):419, 1923.

[56] A. Valfells *et al.* Effects of pulse-length and emitter area on virtual cathode formation in electron guns. *Physics of Plasmas*, 9(5):2377, May 2002.

[57] Davis *et. al*. Quantum efficiency measurements of a copper photocathode inan RF electron gun. In *Proceedings of the 1993 IEEE Particle Accelerator Conference.*, Washington, DC., May 17-20 1993.

[58] P.R. Bevington. *Data Reduction and Error Analysis for the Physical Sciences*. McGraw-Hill, 1969.

[59] J.E. Cooley and E.Y. Choueiri. A universal scaling parameter for undervoltage breakdown. *submitted for publication*.

[60] R.L. Burton and P. J. Turchi. Pulsed plasma thruster. *Journal of Propulsion and Power*, **14**(5):716–735, September-October 1998.

[61] R.G. Jahn. *Physics of Electric Propulsion*. McGraw-Hill Book Company, 1968.

[62] P.J. Hart. Modified snowplow model for coaxial plasma acclerators. *Journal of Applied Physics*, 35(12):3425–3431, December 1964.

[63] W.J. Guman. Solid propellant pulsed plasma micro-thruster studies. In 6^{th} *Aerospace Sciences Meeting*, New York, New York, January 22-24 1968. AIAA 68-85.

[64] J.K. Ziemer. A review of gas-fed pulsed plasma thruster research over the last half-century. Available at http://alfven.princeton.edu/publications.htm.

[65] S. Domitz, H.G. Kosmahl, P. Ramins, and N.J. Stevens. Survey of electromagnetic accelerators. Technical Report TN D-3332, NASA, 1965.

[66] O.K. Mawardi, editor. *Proceedings of an International Symposium on Plasma Guns, Pysics of Fluids Supplement (Part II, Vol. 7(11))*, November 1964.

[67] T.E. Markusic and E.Y. Choueiri. Visualization of current sheet canting in a pulsed plasma accelerator. In 26^{th} *International Electric Propulsion Conference*, Kitakyushu, JAPAN, October 17-21 1999. IEPC 99-206.

[68] J.K. Ziemer, E.Y. Choueiri, and D. Birx. Comparing the performance of co-axial and parallel-plate gas-fed PPTs. In 26^{th} *International Electric Propulsion Conference*, Kitakyushu, JAPAN, October 17-21 1999. IEPC 99-209.

[69] L. Aronowitz and D.P. Duclos. Characteristics of the pinch discharge in a pulsed plasma accelerator. In E. Stuhlinger, editor, *Electric Propulsion Development*, volume 9 of *Progress in Astronautics and Rocketry*. Academic Press, 1963.

[70] D.P. Duclos, L. Aronowitz, F.P. Fessenden, and P.B. Carstensen. Diagnostic studies of a pinch plasma accelerator. *AIAA Journal*, 1(11):2505–2513, November 1963.

[71] R.G. Jahn and W. von Jaskowsky. Structure of a large-radius pinch discharge. *AIAA Journal*, 1(8):1809–1814, August 1963.

[72] R.G. Jahn and W. von Jaskowsky. Current distributions in large-radius pinch discharges. *AIAA Journal*, 2(10):1749–1753, October 1964.

[73] M. Rosenbluth. Infinite conductivity theory of the pinch. Technical Report LA-1850, Los Alamos, 1954.

[74] J.K. Ziemer, E.Y. Choueiri, and D. Birx. Is the gas-fed PPT an electromagnetic accelerator? An investigation using measured performance. In 35^{th} *Joint Propulsion Conference*, Los Angeles, CA, June 20-24, 1999. AIAA 99-2289.

[75] C.J. Michels and P. Ramins. Performance of coaxial plasma gun with various propellants. In *Proceedings of an International Symposium on Plasma Guns, Pysics of Fluids Supplement (Part II, Vol. 7(11))*, pages S71–S74, November 1964.

[76] J. Marshal. Performance of a hydromagnetic plasma gun. *The Physics of Fluids*, 3(1):134–135, January-February 1960.

[77] L.C. Burkhardt and R.H. Lovberg. Current sheet in a coaxial plasma gun. *The Physics of Fluids*, 5(3):341–347, March 1962.

[78] T.J. Gooding, B.R. Hayworth, and R.H. Lovberg. Instabilities in a coaxial plasma gun. *AIAA Journal*, 1(6):1289–1292, June 1963.

[79] R.H. Lovberg. Inference of plasma parameters from measurement of E and B fields in a coaxial accelerator. In *Proceedings of an International Symposium on Plasma Guns, Pysics of Fluids Supplement (Part II, Vol. 7(11))*, pages S57–S61, November 1964.

[80] A.V. Larson, T.J. Gooding, B.R. Hayworth, and D.E.T.F. Ashby. An energy inventory in a coaxial plasma accelerator driven by a pulse line energy source. *AIAA Journal*, 3(5):977–979, May 1965.

[81] D.E.T.F. Ashby, T.J. Gooding, B.R. Hayworth, and A.V. Larson. Exhaust measurements on the plasma from a pulsed coaxial gun. *AIAA Journal*, 3(6):1140–1142, June 1965.

[82] D.E.T.F. Ashby. Energy loss in pulsed coaxial plasma guns. *AIAA Journal*, 3(6):1045–1047, June 1965.

[83] R.H. Lovberg. The measurement of plasma density in a rail accelerator by means of schlieren photography. *IEEE Transactions on Nuclear Science*, pages 187–198, January 1964.

[84] R.H. Lovberg. Schlieren photography of a coaxial acclerator discharge. *The Physics of Fluids*, 8(1):177–185, January 1965.

[85] A.V. Larson, L. Liebing, and R. Dethlefsen. Experimental and evaluation studies of a coaxial plasma gun accelerator. Technical Report CR-54710, NASA, 1966.

[86] D.E.T.F. Ashby, L. Liebing, A.V. Larson, and T.J. Gooding. Quasi-steady-state pulsed plasma thrusters. *AIAA Journal*, 4(5):831–835, May 1966.

[87] P. Gloersen, B. Gorowitz, and J.H. Rowe. Some characteristics of a two-stage repetitively fired coaxial gun. *IEEE Transactions on Nuclear Science*, pages 249–265, January 1964.

[88] P. Gloersen, B. Gorowitz, and J.T. Kenney. Energy efficiency trends in a coaxial gun plasma engine system. *AIAA Journal*, 4(3):436–441, March 1966.

[89] L. Aronowitz. Delays in initiation of discharges in pulsed plasma accelerators. *AIAA Journal*, 2(11):2019–2020, November 1964.

[90] W.J. Guman. Switch-triggered pulsed plasma accelerator thrust measurements. *AIAA Journal*, 3(6):1158–1159, June 1965.

[91] J.W. Berkery. *Current Sheet Mass Leakage in a Pulsed Plasma Accelerator*. PhD thesis, Dept. of Mechanical and Aerospace Engineering, Princeton University, Princeton, NJ, 2005.

[92] T.E. Markusic. *Current Sheet Canting in Pulsed Electromagnetic Accelerators*. PhD thesis, Dept. of Mechanical and Aerospace Engineering, Princeton University, Princeton, NJ, 2002.

[93] B. Gorowitz, T.W. Karras, and P. Gloersen. Performance of an electrically triggered repetitively pulsed coaxial plasma engine. *AIAA Journal*, 4(6):1027–1031, June 1966.

[94] T.W. Karras, B. Gorowitz, and P. Gloersen. Neutral mass density measurements in a repetitively pulsed coaxial plasma accelerator. *AIAA Journal*, 4(8):1366–1370, August 1966.

[95] B. Gorowitz, P. Gloersen, and T.W. Karras. Steady state operation of a two-stage pulsed coaxial plasma engine. In 5^{th} *Electric Propulsion Conference*, San Diego, California, March 7-9 1966. AIAA 66-240.

[96] J.K. Ziemer and E.Y. Choueiri. Performance and erosion measurements of gas-fed pulsed plasma thrusters at NASA jet propulsion laboratory. Technical Report EPPDyL-JPL99a, Princeton University, March 1999.

[97] J.K. Ziemer, T.E. Markusic, and E.Y. Choueiri. Effects of ignition on discharge symmetry in gas-fed pulsed plasma thrusters. In 35^{th} *Joint Propulsion Conference*, Cleveland, OH, July 13-15, 1998. AIAA 98-3803.

[98] J. Li. Design of a microwave-initiated pulsed plasma thruster. Undergraduate senior thesis, Mechanical and Aerospace Engineering Department, Princeton University, 2006. Available online at: http://alfven.princeton.edu/publications.htm.

[99] J.F. Ready. *Effects of High-Power Laser Radiation*. Academic Press, 1971.